Title

High-Aperture Optical Microscopy Methods for Super-Resolution Deep Imaging and Quantitative Phase Imaging

Author

Kim, Jeongmin

Publication Date

2016

High-Aperture Optical Microscopy Methods for Super-Resolution Deep Imaging and Quantitative Phase Imaging

by

Jeongmin Kim

A dissertation submitted in partial satisfaction of the

requirements for the degree of

Doctor of Philosophy

in

Engineering – Mechanical Engineering

and the Designated Emphasis

in

Nanoscale Science and Engineering

in the

Graduate Division

of the

University of California, Berkeley

Committee in charge:

Professor Xiang Zhang, Chair
Professor Liwei Lin
Professor Laura Waller

Summer 2016

High-Aperture Optical Microscopy Methods for Super-Resolution Deep Imaging and Quantitative Phase Imaging

Abstract

High-Aperture Optical Microscopy Methods
for Super-Resolution Deep Imaging and Quantitative Phase Imaging

by

Jeongmin Kim

Doctor of Philosophy in Engineering – Mechanical Engineering
and the Designated Emphasis in
Nanoscale Science and Engineering

University of California, Berkeley

Professor Xiang Zhang, Chair

Optical microscopy, thanks to the noninvasive nature of its measurement, takes a crucial role across science and engineering, and is particularly important in biological and medical fields. To meet ever increasing needs on its capability for advanced scientific research, even more diverse microscopic imaging techniques and their upgraded versions have been intensively developed over the past two decades. However, advanced microscopy development faces major challenges including super-resolution (beating the diffraction limit), imaging penetration depth, imaging speed, and label-free imaging. This dissertation aims to study high numerical aperture (NA) imaging methods proposed to tackle these imaging challenges.

The dissertation first details advanced optical imaging theory needed to analyze the proposed high NA imaging methods. Starting from the classical scalar theory of optical diffraction and (partially coherent) image formation, the rigorous vectorial theory that handles the vector nature of light, *i.e.*, polarization, is introduced. New sign conventions for polarization ray tracing based on a generalized Jones matrix formalism are established to facilitate the vectorial light propagation with physically consistent outcomes.

The first high NA microscopic imaging of interest is wide-field oblique plane microscopy (OPM) for high-speed deep imaging. It is a simple, real-time imaging technique recently developed to access any inclined cross-section of a thick sample. Despite its experimental demonstration implemented by tilted remote focusing, the optical resolution of the method has not been fully understood. The anisotropic resolving power in high NA OPM is rigorously investigated and interpreted by deriving the vectorial point spread function (PSF) and vectorial optical transfer function (OTF). Next, OPM is combined with stochastic optical reconstruction microscopy (STORM) to achieve super-resolution deep imaging. The proposed method, termed *oblique*STORM, together with oblique lightsheet illumination paves the way for deeper penetration readily available in localization-based super-resolution microscopy. The key performance metrics of *oblique*STORM, quantitative super-resolution and axial depth of field, are studied. *oblique*STORM could achieve sub-50-nm resolution with a penetration depth of tens of microns for biological samples.

The last part of the thesis covers the development of nonparaxial imaging theory of high NA differential phase contrast (DPC) microscopy for high resolution quantitative phase imaging. The phase retrieval in conventional optical DPC microscopy relies on the paraxial transmission cross-coefficient (TCC) model. However, this paraxial model becomes invalid in high NA DPC imaging. Formulated here is a more advanced nonparaxial TCC model that considers the nonparaxial nature of light propagation, apodization in high NA imaging systems, and illumination source properties. The derived nonparaxial TCC is numerically compared with the paraxial TCC to demonstrate its added features. The practical forms of the TCC for high resolution phase reconstruction are discussed for two special types of objects, weak objects and slowly varying phase objects.

The theoretical studies conducted here can help to bring such high NA microscopy techniques into the real world to solve imaging challenges.

To My Family

Contents

List of Figures

Acknowledgments

I would like to thank my mentor, Professor Xiang Zhang, for his extreme support on my research and graduate life. First of all, I was influenced a lot by his enthusiasm, encouragement, and big passion on research. Especially his attitude on research trying to understand fundamental science and solve big problems changed me the most. Rather than staying in my former engineering-oriented mindset on research, I have begun to try to see the big picture of my research field and to solve the biggest challenges. I believe that this is the most valuable lesson I learned during the PhD years. He also supported lots of conferences and Summer/Winter school programs that helped to broaden my horizons. His guidance in scientific writing also helped me to learn how to convey an idea in concise and clear ways. All of these would not happen without him. I would also like to thank Prof. Liwei Lin, Prof. Zi. Q. Qiu, Prof. Chris Dames, and Prof. Laura Waller for serving on my qualification committee as well as my dissertation committee. Professor Liwei Lin encouraged me a lot in his ME119 class I took first at Berkeley. As a department major field advisor, he also advised me for years. Prof. Qiu is my best instructor at Berkeley, from whom I learned about electromagnetism and solid state physics. I also enjoyed fabulous lectures on microscale heat transfer by Prof. Dames. Professor Laura Waller gave me many pieces of good advice on my research as well as a great opportunity of collaboration with her group on quantitative phase imaging. She also offered me a great chance to discuss with Prof. Collin Sheppard during his visit at Berkeley on February-March, 2016.

Also, I want to especially thank all my former and current collaborators: Yuan Wang, Shaomin Xiong, Prof. Tongcang Li, Prof. Sadao Ota, Zi Jing Wong, Ye-Long Xu, Prof. Liang Pan, Pankaj K. Jha, Kevin O'Brien, Michael Mrejen, Chihhui Wu, Nir Shitrit, and Michael Chen. I also thank all former and current 'Xlab' members for their friendship and support, especially David Barth, Lin Li, Prof. Jun Suk Rho, Xiaoze Liu, Wei Bao, Cheng Gong, Sui Yang, Jun Xiao, Chad Ropp, Taiki Hatakeyama, and Nga Thien Bui.

Finally, and most importantly, I would like to thank my family for their endless love, trust, and support. This dissertation is especially dedicated to my parents.

Chapter 1

Introduction

1.1 Optical Imaging: Microscopy

Optical imaging vitally assists studies across many fields in science and engineering. Today diverse microscopy tools are available, such as x-ray, atomic force, electron, and optical microscopes, to study nano-/micro-scale science in biology, physics, material science, etc. Among these varied imaging instruments, optical microscopy is a preferred choice in biological and medical fields thanks to its non-invasive, or minimally invasive, nature. As shown in Fig. 1.1, optical microscopy covers biological imaging over broad scales from sub-cellular

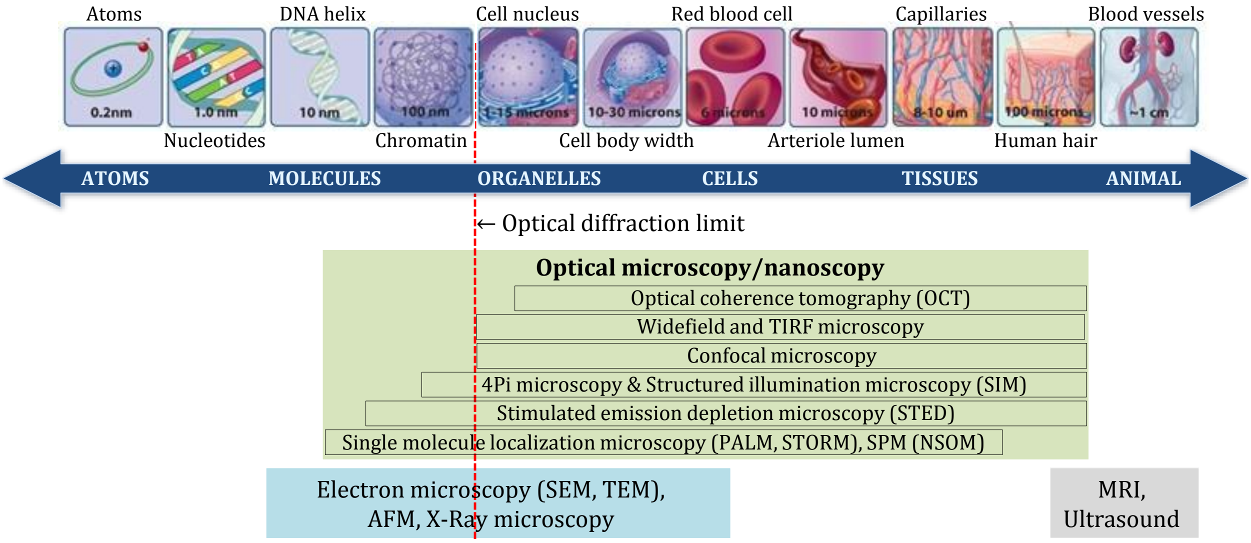

Figure 1.1: Coverage of various microscopy techniques for biological entities[1] at different scales. Super-resolution optical microscopy methods can access sub-cellular features.

---

[1] Source: `http://www.nature.com/scitable`

to animal levels. Comparatively, electron microscopy (EM) certainly provides excellent resolution but is incompatible with living samples. EM requires an electrically conductive, thin sample as well as a vacuum operating environment to lower ambient electron scattering. Recently graphene-assisted electron microscopy allows live cell imaging [1], but it may have limited access to near-surface areas of samples. On the other hand, optical microscopy has less stringent sample preparation and sample environment restrictions, and thus is live-cell compatible in general. In fact, labeling a living sample with fluorescent dyes, or other exogenous contrast agents, is a common microscopy procedure with favorable or at least minimally harmful sample buffers in fluorescence microscopy. This routine staining process can be even eliminated in applications where no target specificity is required. Then imaging contrast is rather endogenously achieved by label-free optical microscopy techniques such as phase contrast imaging, interferometric imaging, or nonlinear imaging.

1.2 Challenges in optical microscopy

Since the invention of a light compound microscope by Hans Janssen in 16th century, optical microscopy has been continually advanced. The advent of lasers in 1960 further accelerated developments in scanning optical microscopes. These days various types of optical microscopes are commercially available from bright/dark field/phase contrast microscopes, scanning microscopes to super-resolution microscopes. Yet even more diverse microscopy techniques are emerging from many research groups. This implies, despite its advantage of non-invasiveness over non-optical means, optical microscopy still faces many other challenges. The following section describes current major challenges in optical microscopy and how researchers try to overcome such obstacles.

The optical resolution in microscopes is limited by light diffraction to roughly a half the wavelength, $\lambda/2$, of the light used. This so-called Abbe diffraction limit, $\frac{\lambda}{2NA}$, discovered by Ernst Abbe in 1873, where NA is a numerical aperture of the imaging system, indicates that in conventional optical microscopes a resolving power below 150 nm is physically impossible. Nonetheless, biologists have dreamed of having super-resolution microscopes that can resolve sub-100 nm details or even better resolution down to sub-10 nm to observe molecular features such as protein-protein interactions. Scientists have been proposing many interesting ideas on how to break the diffraction limit. Superlens [2, 3], hyperlens [4, 5], and metalenses [6] were devised to properly handle evanescent waves originating from fine structures of the samples. Their limited field of view and biocompatibility remain unresolved. Superoscillations [7] implemented by a special phase modulation were also demonstrated as a super-resolution imaging technique [8]. This nascent method needs to overcome many hurdles to be practically available. Scanning probe microscopy (SPM) is more practical for achieving sub-100 nm resolution, but with topographic-limited imaging and no affinity to biological samples in liquid buffers. Structured illumination microscopy (SIM) [9] was initially proposed to double optical resolution, but further advancement was made to attain around 50 nm resolution or even better for techniques named lattice light-sheet microscopy [10], nonlinear SIM

[11], plasmonic SIM [12, 13], and hyperstructured illumination [14]. Stimulated emission depletion microscopy (STED) [15] is also a well-established method to achieve sub-100 nm resolution in scanning microscopy, for which imaging speed was much improved by multi-STED beams [16]. Another remarkable far-field super-resolution method was achieved by a single molecule localization technique: PALM (photoactivated localization microscopy) [17], FPALM (fluorescence photoactivation localization microscopy) [18], and STORM (stochastic optical reconstruction microscopy) [19]. These three methods published in 2006 are the same in principle, but the first two used photoswitchable fluorescent proteins while the last used synthetic dyes. This localization approach generally enables 20 nm lateral and 50 nm axial resolutions at relaxed temporal resolution, having a potential to realize sub-10 nm resolution with brighter fluorescent dyes [20–22].

While many target objects of interest are located inside samples, penetration depth in conventional microscopes is typically limited to a few tens of microns, which is a ballistic limit of photon scattering. The major barriers in deep tissue imaging are optical aberrations by inhomogeneous refractive index for transparent samples (plus their dynamic motions if alive), and light scattering for opaque samples. Adaptive optics (AO) [23] that corrects sample-induced and/or system-induced aberrations has improved penetration depth, when combined with two-photon fluorescence microscopy, up to 400 μm for transparent biological samples such as zebrafish [24, 25] and *C. elegans* [10]. For non-transparent samples, imaging depth is deemed possible up to around 10 times the ballistic mean free path of photon scattering in samples [26]. This depth is called transport mean free path (TMFP), which is the onset of random scattering of photons, and is around 1-2 mm for typical animal tissues. Within this range, two-photon and three-photon microscopy demonstrated an imaging depth of up to around 2 mm for mouse brains with near-infrared (NIR) femtosecond lasers [27, 28]. Imaging research for turbid, or highly scattering, media above one TMFP, relying on diffusive photons, is still in its nascent stage. The main concentration in this modern AO approach still stays at light focusing both spatially and temporally by mapping the media's transmission matrix in a high-speed, non-invasive way [29–35]. Recently speckle correlation imaging [36, 37] has gained attention as a potential approach in this field. Alternatively, though it is a non-optical method, photoacoustic microscopy (PAM) [38] and tomography (PAT) [39] are also widely being studied, promising an imaging depth on the order of a few centimeters at the expense of imaging resolution of around a few microns or worse [40–42]. Another consideration in optical deep tissue imaging is a limited optical window (or spectrum) available to use, depending on the light absorption property in animal tissues by endogenous chromophores and according autofluorescence induced [43, 44].

Imaging speed matters in studies on dynamics of living samples. For example, action potentials in neurons change in *ms* time scale [45], and brain rhythms in the cortex oscillate as fast as 100 Hz [46]. Certain cells like single-cell protozoan *Tetrahymena thermophila* [47] are in rapid motion. Nevertheless, there exist no optical imaging tools that faithfully capture these signals over broader areas or in three dimensions. Given that the signals are strong enough with brighter illumination, the imaging rate is typically clamped by detector speeds. The readout rate of state-of-the-art scientific CMOS (complementary metal oxide semiconductor) cameras for microscopy applications is around 500M pixels/s, allowing 100 frames/s (fps) at full-array readout or higher at sub-array readout. This way at the expense of downsizing field of view (FOV), a volumetric imaging rate at around 20 volumes/s has been demonstrated [48, 49]. There are ultra-high speed CMOS-based cameras, Phantom series by Vision Research Inc., at 25G pixels/s, or 25,000 fps or even as high as 1Mfps at reduced array readout. These high-priced cameras are being used mainly for cinema applications and for some scientific research, but have not been fully proven yet for their feasibility in high-speed microscopy applications. Digital holographic imaging, recording 3D information of samples as modulated interferograms into 2D sensors, is inherently fast (1500 volumes/s [50]) but has its own challenges such as coherence-related noise. Light-field microscopy [51] allows synthetic reconstruction of 3D images at lower NA, at a rate of 20 volumes/s [52]. Optical microscopy with a single pixel camera [53], adapting a new undersampling paradigm of compressed sensing [54, 55], would potentially improve imaging speeds up to 1 Mfps [56, 57]. Rather than using aerial sensors, a fast and sensitive photomultiplier tube (PMT) combined with a frequency domain signal multiplexing was also proposed in microscopy to achieve a 4.4 kfps rate [58].

Photodamage on samples is an important aspect not to be neglected. Although comparatively much safer than non-optical illumination sources such as x-ray and electron beams, modern advanced optical microscopes operating at multi-sun regimes [59] negatively influence both living samples (phototoxicity) and fluorescent dyes (photobleaching). These undesirable effects limit long-term observations of the physiological state of live-cells. A design optimization on the efficiency of signal transmission and source/detector synchronization certainly minimizes photodamage [60]. Alternatively, quantum imaging [61, 62] that allows lower photon flux illumination thanks to its sub-shot-noise imaging capability has begun to draw attention recently.

Last but not least, an ultimate goal of biological imaging, especially at the cellular level, would be label-free imaging that is truly non-invasive. A variety of phase imaging methods have been proposed for this purpose: phase contrast microscopy [63], knife-edge microscopy [64], digital holographic microscopy [65], differential interference contrast microscopy [66], optical coherent tomography (OCT) [67], etc. Other approaches utilizing the intrinsic contrast of samples include photoacoustic microscopy/tomography [40] and nonlinear optical (NLO) microscopy [68, 69]. NLO microscopy is in general tightly-focused 3D scanning microscopy that detects various types of nonlinear signals from samples in different modality [70]: second harmonic generation (SHG), third harmonic generation (THG), four-wave mixing (FWM), coherent anti-Stokes Raman scattering (CARS), and nonlinear absorption [71]. Modern label-free imaging also employs computational approaches, such as Fourier ptychographic microscopy [72] and LED array microscopy [73], that either enable new capabilities or improve imaging performance.

A few challenges addressed above are mutually opposing. An improvement in one challenge can result in aggravating the other challenges. For example, localization-based microscopy attains super-resolution at the expense of temporal resolution. Super-resolution STED microscopy performs a finer raster scanning, which generally reduces imaging rates or field of view (FOV) or both. Deep imaging often requires stronger illumination or longer dwell time of the detector at deeper penetration depth due to a reduced photon efficiency, and this causes more severe photodamage or slows down imaging speed. In high-speed imaging, maintaining a reasonable signal-to-noise ratio at shorter dwell time also demands brighter illumination.

1.3 Motivation and objective

In order to tackle the aforementioned challenges of optical imaging, theoretical and experimental studies on three high NA imaging methods were conducted and are described throughout this dissertation.

As a way to achieve high speed, deep imaging along any arbitrary plane of interest in 3D samples, oblique plane microscopy is studied. Whereas the concept of oblique plane microscopes [74–78] was already proposed, their performance has not been clearly explained. In this dissertation, vectorial diffraction theory is employed to accurately predict and interpret imaging performance in high NA oblique plane microscopy.

Next, a super-resolution deep imaging approach, termed *oblique*STORM is investigated. This is single molecule localization microscopy combined with oblique plane microscopy, targeting more than one-order deeper penetration depth than is possible with current far-field super-resolution microscopy. The proposed method can help to answer biological questions at sub-cellular and tissue levels associated with inner parts of living samples.

For more accurate quantitative, high-resolution phase imaging, nonparaxial differential phase contrast (DPC) microscopy is studied. The classical DPC theory used for phase reconstruction is based on the paraxial diffraction theory, which is invalid in higher NA system. Here, non-paraxial diffraction theory, together with properties of light sources considered, is harnessed to derive transfer functions necessary for more precise phase retrieval.

The following chapters are outlined below:

- Chapter 2 covers advanced imaging theory as a theoretical tool for rigorous treatment of the novel high NA imaging systems under consideration. After the fundamental wave nature of light and its propagation are introduced, classical two-dimensional (and three-dimensional) image formation theory, including partially coherent imaging theory, are first reviewed. Then a transition to vectorial imaging theory is made. As a necessary step of a vectorial analysis of imaging systems, polarization ray tracing with new sign conventions in generalized Jones matrices is proposed to obtain physically consistent results, including some case examples. Numerical simulations are also performed to show the effectiveness of the vectorial theory over the classical scalar theory.

- Chapter 3 concentrates on a theoretical study of oblique plane microscopy (OPM). OPM attempts to capture a wide-field image along an inclined plane with respect to the microscope's focal plane for a three-dimensional object. Experimental demonstrations have been reported but the optical resolution of the method is still unclear. From the rigorous vectorial theory introduced in Chapter 2, optical resolution of OPM is predicted in terms of the vectorial point spread function (PSF) and the optical transfer function (OTF), including interpretations of the results. An experimental study is briefly introduced.

- Chapter 4 deals with oblique plane super-resolution microscopy (*oblique*STORM), for super-resolution deep imaging. The proposed method is theoretically studied to predict key performance metrics: the anisotropic PSF in fluorescence imaging, quantitative super-resolution, and achievable penetration depth. Preliminary experimental results are also presented.

- Chapter 5 describes nonparaxial DPC microscopy. Imaging equations are formulated using the nonparaxial diffraction theory for varied system configurations. The nonparaxial transmission cross-coefficient (TCC) of the high NA DPC imaging system is derived and numerically compared with the paraxial TCC. The practical forms of the derived TCC are discussed for two special types of objects, weak objects and slowly varying phase objects. A few considerations for experimental corroboration of the derived theory are also discussed.

- Chapter 6 includes a summary and conclusion of the dissertation research and introduces future work and possible research directions.

Chapter 2

Advanced Imaging Theory

Classical imaging theory has been a solid foundation to accurately predict imaging resolution of early stage's low-aperture optical microscopes. Its small-angle (or paraxial) approximation [79] simplified an image formation as a linear process in the realm of the Fourier optics. The development of high NA microscope objectives ($NA > 0.7$), however, made such a linear theory no longer valid [80, 81]. The major disagreement results from the three factors: a vectorial nature of light, *i.e.*, polarization, non-paraxial light propagation, and apodization in high aperture system. These are not conceptually difficult but considered mathematically too complicated. In fact, there exist no precise analytical equations for high NA image formations. This chapter revisits optical diffraction theory and image formation theory. The key physical concepts and mathematical formulation behind the optical diffraction and the image formation are briefly summarized for low NA imaging systems. Then high NA image formation is conceptually introduced with an emphasis on the role of the vectorial approach. New sign conventions for the Jones matrix formalism are proposed to trace polarization changes over light propagation through optical systems. The sign conventions suggested here produce physically consistent results, as opposed to previous studies [82–85]. In the end, numerical simulations are provided to help better understanding of the vectorial theory and to show its effectiveness. This complicated but rigorous approach will correctly answer imaging performance of many emerging high NA microscopy methods.

2.1 Optical diffraction theory

Vectorial diffraction theory

Light is an electromagnetic wave, consisting of transverse electric $\vec{\mathcal{E}}$ and magnetic $\vec{\mathcal{B}}$ fields, obeying the *macroscopic* Maxwell's equations in a sourceless (no charges), non-magnetic medium, in differential form in SI units [86] as

$$\begin{aligned}\nabla \cdot \vec{\mathcal{D}}(\vec{x},t) &= 0\\ \nabla \cdot \vec{\mathcal{B}}(\vec{x},t) &= 0\\ \nabla \times \vec{\mathcal{E}}(\vec{x},t) &= -\frac{\partial \vec{\mathcal{B}}(\vec{x},t)}{\partial t}\\ \nabla \times \vec{\mathcal{H}}(\vec{x},t) &= \frac{\partial \vec{\mathcal{D}}(\vec{x},t)}{\partial t},\end{aligned} \tag{2.1}$$

where ∇ denotes the Laplace operator, $\vec{\mathcal{D}}$ the electric displacement, $\vec{\mathcal{H}}$ the magnetic displacement, $\vec{x}$ the position in space, and t the time. A mathematical manipulation with vector identities and constitutive relations $\vec{\mathcal{D}} = \epsilon\vec{\mathcal{E}}$ and $\vec{\mathcal{H}} = \mu^{-1}\vec{\mathcal{B}}$ for linear, isotropic, homogeneous and nondispersive medium leads to the wave equation that electric fields must follow as

$$\nabla^2\vec{\mathcal{E}} - \mu\epsilon\frac{\partial^2\vec{\mathcal{E}}(\vec{x},t)}{\partial^2 t^2} = 0, \tag{2.2}$$

where μ is magnetic permeability and ϵ is electric permittivity. For a monochromatic light oscillating at an angular frequency of ω, *i.e.*, $\vec{\mathcal{E}}(\vec{x},t) = \mathrm{Re}(\vec{E}(\vec{x})e^{-i\omega t})$, the wave equation can be reduced to the time-independent Helmholtz wave equation for the complex amplitude $\vec{E}(\vec{x})$ as

$$(\nabla^2 + k^2)\vec{E}(\vec{x}) = 0, \tag{2.3}$$

where $k = \omega\sqrt{\mu\epsilon}$ is wave number in medium.

A general integral solution for the Helmholtz equation using the Green's method is derived [86–88] as

$$\vec{E}(\vec{x}) = \frac{1}{4\pi}\iint_S \left[i\omega(\vec{N}\times\vec{B}_S)G + (\vec{N}\times\vec{E}_S)\times\nabla' G + (\vec{N}\cdot\vec{E}_S)\nabla' G\right] d^2\vec{x}', \tag{2.4}$$

where S denotes a wavefront surface typically over the reference sphere of the exit pupil in an imaging system, $\vec{N}$ the inwardly facing surface normal unit vector to the wavefront, $\vec{E}_S, \vec{B}_S$ electric and magnetic fields at the exit pupil, and $G = e^{ik|\vec{R}|}/|\vec{R}|$ the Green function representing a diverging spherical wave. See Fig. 2.1 for details. Using the Gauss's law and vector identities, Eq. (2.4) can be converted to vectorial Kirchhoff diffraction integral at far-field ($R \gg k^{-1}$):

$$\vec{E}(\vec{x}) = -\frac{ik}{4\pi}\iint_S G\left[\vec{E}_S - (\vec{E}_S\cdot\hat{R})\vec{N} + (\vec{N}\cdot\hat{R})\vec{E}_S\right] d^2\vec{x}', \tag{2.5}$$

where the hat on R indicates a unit vector. Thus an electric field at a position $\vec{x}$ can be calculated if the fields across the aperture are given. There is no contribution from the outside of the aperture by the Sommerfeld radiation condition [86]. The same derivation steps apply to magnetic fields. The calculation of $\vec{E}\cdot\vec{E}^*$ gives the time-averaged electric

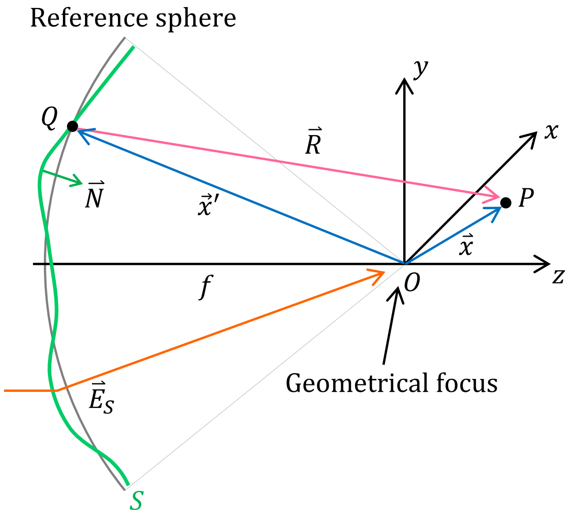

Figure 2.1: Diffraction geometry. O: geometrical focus, P: an observation point ($\vec{x}$), Q: a point ($\vec{x}'$) on the wavefront where the diffraction integral is evaluated, $\vec{R}=\vec{x}-\vec{x}'$.

energy density (or intensity), to which most optical detectors used in optical microscopes respond.

The Debye approximation [89, 90] is usually employed for further simplicity, valid at a high Fresnel number ($N_F = fNA^2/\lambda \gg 1$) [91–93] which is practically true in microscopic imaging. This assumes an observation point ($\vec{x}'$) very close to the geometrical focus such that $\vec{R} = \vec{x} - \vec{x}' \approx (\vec{x} \cdot \vec{N})\vec{N} - \vec{x}'$, reducing Eq. (2.5) into the vectorial Debye integral as

$$\vec{E}(\vec{x}) = -\frac{ik}{2\pi}\frac{e^{ikf}}{f}\iint_S \vec{E}_S(\vec{x}')e^{ik\vec{N}\cdot\vec{x}}\, d^2\vec{x}'. \tag{2.6}$$

This implies that the electric field near focal regions is seen as 1) a Fourier transformation of the field strength $\vec{E}_S(\vec{x}')$ and/or 2) a superposition of plane waves all pointing to the Gaussian focus, thereby generating axially symmetric intensity distribution. This approximation also modifies the physical picture of the Huygens-Fresnel principle for light propagation, as a superposition of planar secondary wavelets, not spherical secondary wavelets. Either Eq. (2.5) or (2.6) requires a prior knowledge on $\vec{E}_S$ which can be estimated from polarization ray tracing through the optical system from the source to the exit pupil, together with any apodization factor if exists. The $\vec{E}_S$ may include an additional factor of $\frac{e^{-ikf}}{f}$ due to its its spherically converging nature at the exit pupil typically supported by a lens. This changes $\frac{e^{ikf}}{f}\iint_S d^2\vec{x}'$ into $\iint_S d\Omega$, where $d\Omega$ denotes an solid angle for $d^2\vec{x}'$.

Scalar diffraction theory

For a *scalar* Helmholtz wave equation, the same Green's method with Kirchhoff boundary conditions (valid for aperture sizes much larger than the wavelength), leads to the Kirchhoff diffraction integral at far-field [86] as

$$E(\vec{x}) = -\frac{1}{4\pi} \iint_S G\vec{N} \cdot \left[\nabla' E_S(\vec{x}') + ik\hat{R}E_S(\vec{x}')\right] d^2\vec{x}'. \tag{2.7}$$

The integral geometry can be any curved surface where both $E(\vec{x}')$ and its gradient $\nabla' E_S(\vec{x}')$ are known. These two Kirchhoff boundary conditions (or *Cauchy* boundary conditions) are known to be mathematically inconsistent [79]. An alternative choice of the Green function as $G_D(\vec{x}, \vec{x}') = e^{ikR}/R - e^{ikR'}/R'$ eliminates the inconsistency, yielding the first Rayleigh-Sommerfeld diffraction formula [79]:

$$E(\vec{x}) = -\frac{ik}{2\pi} \iint_S E_S(\vec{x}') \frac{e^{ikR}}{R} \vec{N}\cdot\hat{R}\, d^2\vec{x}'. \tag{2.8}$$

This formula needs boundary information on only $E(\vec{x}')$ (*Dirichlet* boundary condition) over a planar geometry [86], yet is also widely employed for a non-planar diffraction geometry. This is perhaps thanks to its direct mathematical description of the Huygens-Fresnel principle compared to other diffraction integrals, yet no superior results in optical frequencies [79, 90]. An alternative diffraction integral [94] was also proposed not only to avoid the inconsistency but also to satisfy the reciprocity theorem.

The Fresnel (or paraxial) approximation, $R \approx (z-z') + \frac{(x-x')^2+(y-y')^2}{2(z-z')}$, together with a uniform inclination factor $\vec{N}\cdot\hat{R} \approx 1$ is commonly employed in the scalar diffraction theory. If $(z-z')^2 \gg (x-x')^2 + (y-y')^2$ [79], it provides the Fresnel diffraction formula as

$$E(\vec{x}) = \frac{e^{ik(z-z')}}{i\lambda(z-z')} e^{\frac{ik}{2(z-z')}(x^2+y^2)} \iint_S E_S(x', y') e^{-\frac{ik}{(z-z')}(xx'+yy')} e^{\frac{ik}{2(z-z')}(x'^2+y'^2)}\, dx'dy'. \tag{2.9}$$

For a smaller Fresnel number ($N_F \ll 1$), the Fraunhofer approximation neglects the quadratic phase factor in the integrand, leading to the field at the observation space simply as a Fourier transformation of the field at the diffraction aperture.

The Debye approximation can be also made in the scalar theory for high aperture systems, which may be called the scalar Debye integral as

$$E(\vec{x}) = -\frac{ik}{2\pi} \frac{e^{ikf}}{f} \iint_S E_S(\vec{x}') e^{ik\vec{N}\cdot\vec{x}}\, d^2\vec{x}'. \tag{2.10}$$

Extension to nonmonochromatic waves

The diffraction formulas introduced so far base on a monochromatic wave at a particular ω. For nonmonochromatic waves, the same theory using the time-independent complex amplitude still holds for each ω, and the total field could be numerically obtained by integrating over an overall spectral response from a source to a detector. This strategy was analytically demonstrated for imaging systems with a ultrashort pulsed beam [90]. Otherwise, more rigorous treatment on time-varying phasor amplitude has to be made. Based on the paraxial diffraction theory, Eq. (2.8), the scalar field for nonmonochromatic and narrowband waves in air was derived at a far distance ($R \gg \lambda$) in [95]. Similarly, if the vectorial Kirchhoff diffraction integral, Eq. (2.5), is used, the vectorial field for nonmonochromatic waves at far-field may be given by

$$\vec{\mathcal{E}}(\vec{x},t) = \iint_S \frac{1}{4\pi cR}\frac{d}{dt}\Big[\vec{\mathcal{E}}(\vec{x}',t-t_r) - \big(\vec{\mathcal{E}}(\vec{x}',t-t_r)\cdot\vec{R}\big)\vec{N} + (\vec{N}\cdot\vec{R})\vec{\mathcal{E}}(\vec{x}',t-t_r)\Big]\, d^2\vec{x}', \qquad (2.11)$$

where $t_r = R/c$ is a retardation time taken for a light propagation. For a narrowband light whose bandwidth is much smaller than the central frequency, $\Delta\omega/\bar{\omega} \ll 1$, the field at $R \gg \bar{\lambda}$ could be approximated as

$$\vec{\mathcal{E}}(\vec{x},t) = \iint_S \frac{1}{2i\bar{\lambda}R}\Big(\vec{\mathcal{E}}(\vec{x}',t-t_r) - \big(\vec{\mathcal{E}}(\vec{x}',t-t_r)\cdot\vec{R}\big)\vec{N} + (\vec{N}\cdot\vec{R})\vec{\mathcal{E}}(\vec{x}',t-t_r)\Big)\, d^2\vec{x}'. \qquad (2.12)$$

2.2 Two-dimensional scalar image formation theory

This section covers image formation theory derived from the scalar diffraction integral, Eq. (2.8). As a basic step, two-dimensional (2D) coherent and incoherent imaging for a thin object is first reviewed, then partially coherent imaging comes after as a general case.

Coherent image formation

As illustrated in Fig. 2.2, let us consider the simplest case of 2D coherent image formation for a thin, monochromatic object, $E_o(x_o, y_o)$, with a paraxial lens whose transmittance is $P(\xi,\eta)e^{-\frac{ik}{2f}(\xi^2+\eta^2)}$ [79], where $P(\xi,\eta)$ denotes the pupil function defined over the aperture Σ and f the focal length. Applying the Fresnel diffraction formula twice gives the fields at the paraxial lens and then at the image space sequentially. At an image distance of d_i by

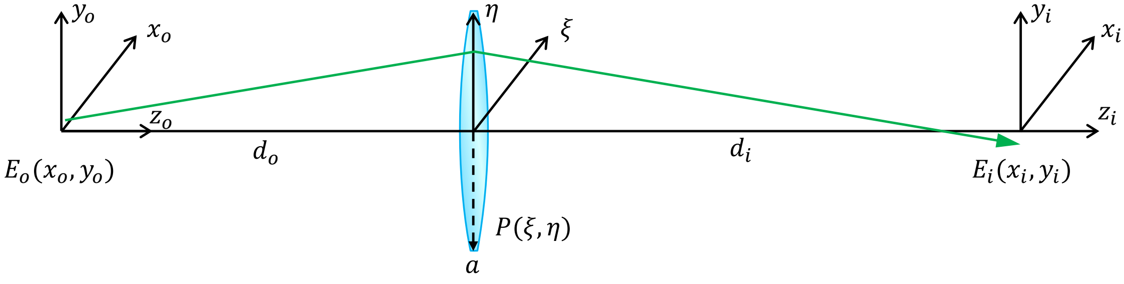

Figure 2.2: Image formation by a thin lens (focal length: f, aperture radius: a). A monochromatic object field E_o forms an image field E_i in the image space with a lens law of $1/d_o + 1/d_i = 1/f$.

the thin lens law $1/d_o + 1/d_i = 1/f$ with a lateral magnification of $M = -d_i/d_o$, the field is derived as

$$\begin{aligned} E_i(x_i, y_i) = \frac{ie^{ik(d_o+d_i)}}{\lambda^2 d_o d_i} e^{\frac{ik}{2d_i}(x_i^2+y_i^2)} \iint_{S_o} \iint_{\Sigma} & E_o(x_o, y_o) P(\xi, \eta) e^{\frac{ik}{2d_o}(x_o^2+y_o^2)} \\ & \times e^{-\frac{ik}{d_o}\left[\xi(x_o - x_i/M) + \eta(y_o - y_i/M)\right]} \, d\xi d\eta \, dx_o dy_o. \end{aligned} \tag{2.13}$$

In general, the pupil function of imaging systems can be defined at the exit pupil and becomes complex if aberrations exist: $\mathcal{P}(\xi, \eta) = P(\xi, \eta) e^{ikW(\xi, \eta)}$ where $W(\xi, \eta)$ is a wavefront error. For an ideal on-axis point object, $E_o(x_o, y_o) = \delta(x_o)\delta(y_o)$, the resulting image field is known as 2D amplitude point spread function (PSF), if scaled down to the object coordinate $(x, y) \equiv (x_i/M, y_i/M)$ and in the flipped pupil coordinate $(\xi_r, \eta_r) \equiv (-\xi, -\eta)$, as

$$h(x, y) = \frac{ie^{ik(d_o+d_i)}}{\lambda^2 d_o d_i} e^{-\frac{ikM}{2d_o}(x^2+y^2)} \iint_{\Sigma} \mathcal{P}(-\xi_r, -\eta_r) e^{-\frac{ik}{d_o}(x\xi_r + y\eta_r)} \, d\xi_r d\eta_r, \tag{2.14}$$

which is, if the quadratic phase factor is neglected, a 2D Fourier transform of the (reflected) pupil function of the imaging system. For a circularly uniform aperture with a radius of a, the shape of PSF is a *jinc* function: $2J_1(r)/r$ where $J_1(r)$ is a Bessel function of the first kind of order one and $r = ka\sqrt{x^2+y^2}/d_o$; the first zero-crossing occurs at $0.61\lambda/(a/d_o) \approx 0.61\lambda/NA$. This implies that an imaging system with a larger aperture (or a higher NA) and a shorter wavelength results in a narrower PSF, thereby better resolution. Hence an optical resolution of an aberration-free system is pupil diffraction-limited.

For objects smaller than one-fourth the aperture dimension of the lens [79] or a PSF falling off quickly [90], the field is approximated as

$$E_i(x, y) = e^{\frac{ik}{2d_o}(x^2+y^2)} \iint_{\Sigma} E_o(x_o, y_o) h(x - x_o, y - y_o) \, dx_o dy_o. \tag{2.15}$$

The image field of a thin object is thus calculated by the 2D convolution of the object field with the amplitude PSF of the imaging system, meaning linear in the complex amplitude. This physically suggests an object model as a set of coherent point sources, and then the image field results from a superposition of all amplitude PSFs displaced on each geometrical image points. This linear systems approach, however, is credible only when the PSF is space-invariant. Strictly speaking, for off-axis point objects, either the two quadratic phase factors inside Eq. (2.13) or an aberrated pupil function could cause space-varying PSFs, which then needs a careful consideration in using it. In such the case, the calculated image field would only be accurate near the on-axis area of the object.

Once the field is calculated, the image intensity is given by its modulus squared as

$$I_i(x, y) = \left| \iint_{\Sigma} E_o(x_o, y_o) h(x - x_o, y - y_o) \, dx_o dy_o \right|^2. \tag{2.16}$$

Linear imaging systems are often analyzed in spatial frequency domain. By taking a Fourier transform in Eq. (2.15) with spatial frequencies $f_x = x/(\lambda d_o)$ and $f_y = y/(\lambda d_o)$ for x

and y directions respectively, if the prephase factor is neglected, the frequency spectrum of the image field, $\tilde{E}_i(f_x, f_y) \equiv \mathcal{F}\{E_i(x_i, y_i)\}$, is given by the convolution theorem of Fourier transform [79] as

$$\tilde{E}_i(f_x, f_y) = \tilde{E}_o(f_x, f_y)\, H(f_x, f_y), \tag{2.17}$$

where $H(f_x, f_y) = \mathcal{F}\{h(x, y)\} = \mathcal{P}(\lambda d_o f_x, \lambda d_o f_y)$ is known as the coherent transfer function (CTF). The CTF can be shown to be exactly a scaled pupil function if the prefactor in Eq. (2.14) and a multiplicative constant on the results of $\mathcal{F}\{h(x, y)\}$ are neglected. The object spectrum is circularly filtered by the CTF at a frequency cutoff of $f_c = a/(\lambda d_o) \approx NA/\lambda$ for a circular aperture, and the remaining frequency content only contributes to image formation. A frequency spectrum of image intensity in coherent imaging system, the Fourier transform of Eq. (2.16), is expressed from the autocorrelation theorem of Fourier transform [79] as

$$\tilde{I}_i(f_x, f_y) = \iint \tilde{E}_o(f'_x, f'_y) H(f'_x, f'_y) \tilde{E}^*_o(f'_x - f_x, f'_y - f_y) H^*(f'_x - f_x, f'_y - f_y)\, df'_x df'_y. \tag{2.18}$$

Incoherent image formation

If an object field is perfectly incoherent (no phase correlations between any two points on it), amplitude PSFs are not coherently summed; rather intensity PSFs, $|h(x, y)|^2$ *a.k.a.* the Airy disk, are linearly superposed as

$$I_i(x, y) = \iint_\Sigma I_o(x_o, y_o) |h(x_o - x, y_o - y)|^2\, dx_o dy_o. \tag{2.19}$$

The Fourier transform of this intensity convolution integral gives an intuition on image formation in spatial frequency point of view, which leads to

$$\tilde{I}_{i,n}(f_x, f_y) = \tilde{I}_{o,n}(f_x, f_y)\, \mathcal{H}(f_x, f_y), \tag{2.20}$$

where the subscript n denotes a normalized Fourier spectrum by its own maximum at $\tilde{I}(0, 0)$, as a maximum spectral power for real and non-negative signals like intensity occurs at the zero frequency. The $\mathcal{H}(f_x, f_y)$ is well known as the optical transfer function (OTF) which is also conventionally normalized as

$$\mathcal{H}(f_x, f_y) = \frac{\iint |h(x, y)|^2 e^{-i2\pi(f_x x + f_y y)}\, dx dy}{\iint |h(x, y)|^2\, dx dy}. \tag{2.21}$$

Again from the autocorrelation theorem and Parseval's theorem [79], one can find out that the OTF is a normalized autocorrelation function of the CTF [96] as

$$\mathcal{H}(f_x, f_y) = \frac{\iint H(f'_x, f'_y) H^*(f'_x - f_x, f'_y - f_y)\, df'_x df'_y}{\iint |H(f'_x, f'_y)|^2\, df'_x df'_y}, \tag{2.22}$$

or in terms of the generalized complex pupil function as

$$\mathcal{H}(f_x, f_y) = \frac{\iint \mathcal{P}(\xi, \eta)\mathcal{P}^*(\xi - \lambda d_o f_x, \eta - \lambda d_o f_y)\, d\xi d\eta}{\iint |\mathcal{P}(\xi, \eta)|^2\, d\xi d\eta}. \tag{2.23}$$

Geometrically, the OTF is interpreted as an area overlap of the complex pupil and its displaced, conjugated pupil, normalized by the pupil area (or a 2D convolution of the pupil with its inversed conjugate pupil). Thus, the quantity is real and non-negative in aberration-free systems with a doubled absolute cutoff frequency compared with the coherent imaging cutoff. A presence of aberrations always negatively influences on the OTF by lowering its modulation $MTF = |OTF|$ than the diffraction-limit, but engineering the pupil apodization could improve the upper limit of the conventional diffraction-limited MTF curve set by a uniform pupil [79].

2.3 Partially coherent image formation theory

Most imaging systems are neither perfectly coherent nor perfectly incoherent mainly due to a statistical nature of source radiations. Optical sources emit light by spontaneous and/or stimulated emissions that randomly fluctuate in time. Also their emission area is finite, any two radiating points of which may be statistically correlated. It is a mutual coherence function, $\Gamma(\vec{x}_1, \vec{x}_2; \tau) \equiv \langle \mathcal{E}(\vec{x}_1, t+\tau)\mathcal{E}^*(\vec{x}_2, t)\rangle$ [95], that properly treats such a random process with a concept of temporal and spatial coherence. Many imaging systems practically satisfy the quasimonochromatic conditions [95]: 1) narrowband light source ($\Delta\lambda \ll \bar{\lambda}$) and 2) optical path-length difference much shorter than the source's coherence length in all possible light propagation of interest. In such a case, the spatial coherence is only a primary concern, which is then described by mutual intensity $J(\vec{x}_1, \vec{x}_2) = \Gamma(\vec{x}_1, \vec{x}_2; 0)$.

A general imaging system may be illustrated as shown in Fig. 2.3. If a source is perfectly incoherent, the coherent imaging theory may still be applied for each source point to obtain

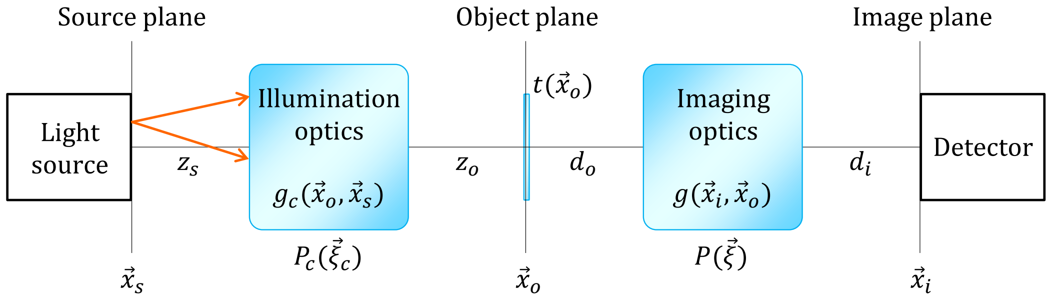

Figure 2.3: Schematic of a general partially coherent imaging system. $g_c(\vec{x}_o, \vec{x}_s)$: amplitude spread function for a point source at $\vec{x}_s$ into the object plane $\vec{x}_o$, $g(\vec{x}_i, \vec{x}_o)$: amplitude spread function between the object and the final image plane. $P_c(\vec{\xi}_c)$ and $P(\vec{\xi})$ are effective pupil functions of illumination and imaging optics respectively.

individual image intensity, followed by an incoherent sum of all to get overall image intensity. This is feasible in such a special case only. Many light sources, however, are partially coherent to a certain degree, characterized by the mutual intensity. As light propagates through space, the mutual intensity does change. The key concept in partially coherent imaging theory is to trace the mutual intensity from the source to the final image plane.

In general, the propagation of the mutual intensity is governed by a pair of the scalar Helmholtz wave equations in scalar theory [95]. More intuitive way is to plug the scalar diffraction integral from the Huygens-Fresnel principle, the scalar version of Eq. (2.12), into the definition of mutual intensity to discover

$$J(\vec{x}_1, \vec{x}_2) = \iint_\Sigma \iint_\Sigma J(\vec{x}'_1, \vec{x}'_2) e^{-i\bar{k}(R_2 - R_1)} \frac{\vec{N}_1 \cdot \vec{R}_1}{\bar{\lambda} R_1} \frac{\vec{N}_2 \cdot \vec{R}_2}{\bar{\lambda} R_2} \, dS_1 dS_2, \tag{2.24}$$

which describes how a mutual intensity between $\vec{x}'_1$ and $\vec{x}'_2$ on a surface Σ evolves after a propagation to $\vec{x}_1$ and $\vec{x}_2$ respectively on another surface of interest. This four-dimensional (4D) process could be repeatedly applied up to the image plane. During the propagation, if intervened by a thin object whose amplitude transmittance is $t(\vec{x})$, the mutual intensity is altered as $J_{out}(\vec{x}_1, \vec{x}_2) = t(\vec{x}_1) t^*(\vec{x}_2) J_{in}(\vec{x}_1, \vec{x}_2)$ at the quasimonochromatic conditions [95]. Once the final mutual intensity function is obtained, image intensity is obtained by merging $\vec{x}_1 = \vec{x}_2$, so that $I(\vec{x}) = J(\vec{x}, \vec{x})$.

Utilizing this procedure, as a check, to the image formation by a thin lens in Fig. 2.2 with the paraxial approximation (or this may also be viewed as the right half of the whole imaging system in Fig. 2.3), image intensity is derived to be

$$I_i(\vec{x}_i) = J_i(\vec{x}_i, \vec{x}_i) = \iiiint J_o(\vec{x}_{o1}, \vec{x}_{o2}) g(\vec{x}_i, \vec{x}_{o1}) g^*(\vec{x}_i, \vec{x}_{o2}) \, d^2\vec{x}_{o1} d^2\vec{x}_{o2}, \tag{2.25}$$

where $J_o(\vec{x}_{o1}, \vec{x}_{o2})$ is mutual intensity at the object plane and $g(\vec{x}_i, \vec{x}_o)$ is the amplitude spread function (an amplitude response at the $\vec{x}_i$ coordinate to a point object located to $\vec{x}_o$) defined as

$$g(\vec{x}_i, \vec{x}_o) = \frac{e^{\frac{i\bar{k}}{2d_i}|\vec{x}_i|^2} e^{\frac{i\bar{k}}{2d_o}|\vec{x}_o|^2}}{\bar{\lambda}^2 d_i d_o} \iint_\Sigma \mathcal{P}(-\vec{\xi}_r) e^{-\frac{i\bar{k}}{d_o}(-\vec{x}_o + \frac{\vec{x}_i}{M}) \cdot \vec{\xi}_r} \, d^2\vec{\xi}_r, \tag{2.26}$$

where $\vec{\xi}_r = (-\xi, -\eta)$ is the flipped pupil coordinate. The four integrals imply that partially coherent imaging is a 4D process. This result can be exactly reduced to the two extremes of the 2D imaging processes: coherent imaging, Eq. (2.16), and incoherent imaging, Eq. (2.19), by putting $J_o(\vec{x}_{o1}, \vec{x}_{o2}) = |E_o(\vec{x}_{o1})|^2$ and $J_o(\vec{x}_{o1}, \vec{x}_{o2}) = I_o(\vec{x}_{o1}) \delta_{2D}(\vec{x}_{o1} - \vec{x}_{o2})$, respectively.

Next, object illumination, the left half of the system in Fig. 2.3, needs to be examined. In principle, the same strategy as before can be implemented to obtain illumination mutual intensity $J_{ill}(\vec{x}_{o1}, \vec{x}_{o2})$ from the known source coherence $J_s(\vec{x}_{s1}, \vec{x}_{s2})$ and the amplitude spread function $g_c(\vec{x}_o, \vec{x}_s)$ of the illumination optics. Then, considering an object of $t(\vec{x}_o)$, the mutual intensity right after the object is given as $J_o(\vec{x}_{o1}, \vec{x}_{o2}) = t(\vec{x}_{o1}) t^*(\vec{x}_{o2}) J_{ill}(\vec{x}_{o1}, \vec{x}_{o2})$. Plugging this into Eq. (2.25), the image intensity for the object in partial coherent imaging can be calculated from the eight-dimensional process as

$$I_i(\vec{x}_i) = \iiiint_{\Sigma_o} \iiiint_{\Sigma_s} J_s(\vec{x}_{s1},\vec{x}_{s2})\, g_c(\vec{x}_{o1},\vec{x}_{s1}) g_c^*(\vec{x}_{o2},\vec{x}_{s2})\, t(\vec{x}_{o1}) t^*(\vec{x}_{o2}) \times g(\vec{x}_i,\vec{x}_{o1}) g^*(\vec{x}_i,\vec{x}_{o2})\, d^2\vec{x}_{s1} d^2\vec{x}_{s2}\, d^2\vec{x}_{o1} d^2\vec{x}_{o2}. \tag{2.27}$$

The mutual intensity of light sources could be approximated several ways. For a partially coherent source as the most general case, $J_s(\vec{x}_{s1},\vec{x}_{s2}) = \sqrt{I_s(\vec{x}_{s1}) I_s(\vec{x}_{s2})}\,\mu_s(\vec{x}_{s2}-\vec{x}_{s1})$, where μ_s is normalized mutual intensity known as the complex coherence factor [95]. If the source area is much smaller than the coherent area ($A_S \gg A_{coh}$) and the source structure is slowly varying compared to A_{coh}, $J_s(\vec{x}_{s1},\vec{x}_{s2}) \approx I_s(\bar{x}_s)\mu_s(\vec{x}_{s2}-\vec{x}_{s1})$, where $\bar{x}_s = (\vec{x}_{s1}+\vec{x}_{s2})/2$ [95]. For an incoherent source used practically in many wide-field optical microscope systems, the source mutual intensity could be modeled as $J_s(\vec{x}_{s1},\vec{x}_{s2}) = I_s(\vec{x}_{s1})\delta_{2D}(\vec{x}_{s1}-\vec{x}_{s2})$. The δ-function introduced here reduces partially coherent imaging to a six-dimensional process.

Also, many microscopes implement uniform intensity illumination, so-called the Köhler illumination, with typically non-uniform, incoherent sources. This illumination conceptually adopts the $1f_c$-$1f_c$ configuration on which the source is imaged at infinity by the condenser optics (with an effective focal length of f_c). Then the amplitude spread function for the illumination optics is derived as

$$g_c(\vec{x}_o,\vec{x}_s) = \frac{e^{\frac{i\bar{k}}{2f_c}|\vec{x}_o|^2} e^{\frac{i\bar{k}}{2f_c}|\vec{x}_s|^2}}{\bar{\lambda}^2 f_c^2} \iint_{\Sigma_c} \mathcal{P}_c(\vec{\xi}_c) e^{-\frac{i\bar{k}}{f_c}(\vec{x}_o+\vec{x}_s)\cdot\vec{\xi}_c}\, d^2\vec{\xi}_c. \tag{2.28}$$

Alternatively, as introduced in [95] the illumination mutual intensity $J_{ill}(\vec{x}_o 1, \vec{x}_{o2})$ may be further simplified in practice. The propagation of mutual intensity from an incoherent source to the entrance pupil of the condenser optics, known as the Van Cittert-Zernike theorem [97], leads to

$$J_s(\vec{\xi}_1,\vec{\xi}_2) \propto \frac{1}{(\bar{\lambda} z_s)^2} \iint_{\Sigma_s} I(\vec{x}_s) e^{\frac{i\bar{k}}{z_s}(\vec{\xi}_2-\vec{\xi}_1)\cdot\vec{x}_s} d^2\vec{x}_s, \tag{2.29}$$

which is a 2D Fourier transform of the source intensity distribution into the difference coordinate $\vec{\xi}_2-\vec{\xi}_1$ at the entrance pupil. Hence the coherence area at the pupil is inversely proportional to the source area, or more accurately $A_{coh} = (\bar{\lambda} z_s)^2/A_S$ [95]. Assuming a larger source whose resulting coherence area at the pupil is extremely smaller than the pupil area (A_p), *i.e.*, $A_p A_s \gg (\bar{\lambda} z_s)^2$, the pupil itself may be approximated as an effective incoherent source. Then the mutual intensity incident on the sample can be specified as

$$J_{ill}(\vec{x}_{o1},\vec{x}_{o2}) = \frac{e^{\frac{i\bar{k}}{2z_o}\left(|\vec{x}_{o2}|^2-|\vec{x}_{o1}|^2\right)}}{\bar{\lambda}^2 z_o^2} \iint_{\Sigma_c} \left|\mathcal{P}_c(\vec{\xi}_c)\right|^2 e^{\frac{i\bar{k}}{z_o}(\vec{x}_{o2}-\vec{x}_{o1})\cdot\vec{\xi}_c}\, d^2\vec{\xi}_c, \tag{2.30}$$

which is now simply a 2D Fourier transform of the squared modulus of the condenser pupil function. Even if the partial coherence at the pupil is considered, from the generalized Van

Cittert-Zernike theorem [98], the same conclusion results given that $A_S(z_o/z_s)^2 \gg A_o$, where A_o is an object area [95].

On the other hand, a linear systems approach can be employed in partially coherent imaging as well, provided that amplitude spread functions are space-invariant. This would be roughly the case for smaller areas in the object and image planes where pre-phase factors at the amplitude spread functions could be neglected. Then, rescaling the image plane coordinate to the object plane coordinate as $\vec{x}_i/M = \vec{x}$ entitles a spatial invariance on the impulse response: $g(\vec{x}, \vec{x}_{o1})g^*(\vec{x}, \vec{x}_{o2}) = g(\vec{x} - \vec{x}_{o1})g^*(\vec{x} - \vec{x}_{o2})$. This converts the 4D integral relation of mutual intensity between two planes, Eq. (2.25), to a 4D convolution integral as

$$J_i(\vec{x}_1, \vec{x}_2) = \iiiint J_o(\vec{x}_{o1}, \vec{x}_{o2}) g(\vec{x}_1 - \vec{x}_{o1}) g^*(\vec{x}_2 - \vec{x}_{o2})\, d^2\vec{x}_{o1} d^2\vec{x}_{o2}. \tag{2.31}$$

As was done at Eq. (2.16), taking the Fourier transform on Eq. (2.31) yields the 4D Fourier spectra of the object and image mutual intensities related as

$$\tilde{J}_i(\vec{f}_1, \vec{f}_2) = G(\vec{f}_1)\, G^*(-\vec{f}_2)\, \tilde{J}_o(\vec{f}_1, \vec{f}_2), \tag{2.32}$$

where $G(\vec{f}) \equiv \mathcal{F}\{g(\vec{x} - \vec{x}_o)\}$ with spatial frequencies from the coordinate difference as $\vec{f} = (\vec{x} - \vec{x}_o)/(\bar{\lambda} d_o)$, and $G(\vec{f}_1)G^*(-\vec{f}_2)$ is a 4D transfer function, or in terms of the pupil function as $\mathcal{P}(\bar{\lambda} d_o \vec{f}_1)\mathcal{P}^*(-\bar{\lambda} d_o \vec{f}_2)$. The mutual intensity spectrum in the image plane is drawn [95] as

$$\tilde{J}_i(\vec{f}_1, \vec{f}_2) = G(\vec{f}_1)G^*(-\vec{f}_2) \iint T(\vec{f}' + \vec{f}_1) T^*(\vec{f}' - \vec{f}_2) \tilde{J}_{ill}(\vec{f}')\, d^2\vec{f}', \tag{2.33}$$

where $T(\vec{f}) \equiv \mathcal{F}\{t(\vec{x}_o)\}$. Further mathematical elaboration leads to the frequency content of the image intensity [95] as

$$\tilde{I}_i(\vec{f}_i) = \iint T(\vec{f}'') T^*(\vec{f}'' - \vec{f}_i)\, C(\vec{f}_i, \vec{f}'')\, d^2\vec{f}'', \tag{2.34}$$

where $\vec{f}_i \equiv \vec{x}/(\bar{\lambda} d_o)$, $C(\vec{f}'', \vec{f}_i)$ is the transmission cross-coefficient (TCC) [99–101] defined as

$$C(\vec{f}_i, \vec{f}'') = \iint G(\vec{f}'' - \vec{f}')\, G^*(\vec{f}'' - \vec{f}_i - \vec{f}')\, \tilde{J}_{ill}(\vec{f}')\, d^2\vec{f}', \tag{2.35}$$

which describes the unique property of the imaging system alone, excluding the object. Once the TCC is identified, the image intensity for an object can be predicted by the inverse Fourier transform of $\tilde{I}_i(\vec{f}_i)$ calculated from Eq. (2.34). If the simplified mutual intensity for illumination, Eq. (2.30) is borrowed, the TCC can be expressed in terms of imaging and condenser pupil functions:

$$C(\vec{f}'', \vec{f}_i) = \iint \mathcal{P}\big(-\bar{\lambda} d_o (\vec{f}' - \vec{f}'')\big)\, \mathcal{P}^*\big(\bar{\lambda} d_o (\vec{f}' - \vec{f}'' + \vec{f}_i)\big)\, \big|\mathcal{P}_c(\bar{\lambda} z_o \vec{f}')\big|^2\, d^2\vec{f}'. \tag{2.36}$$

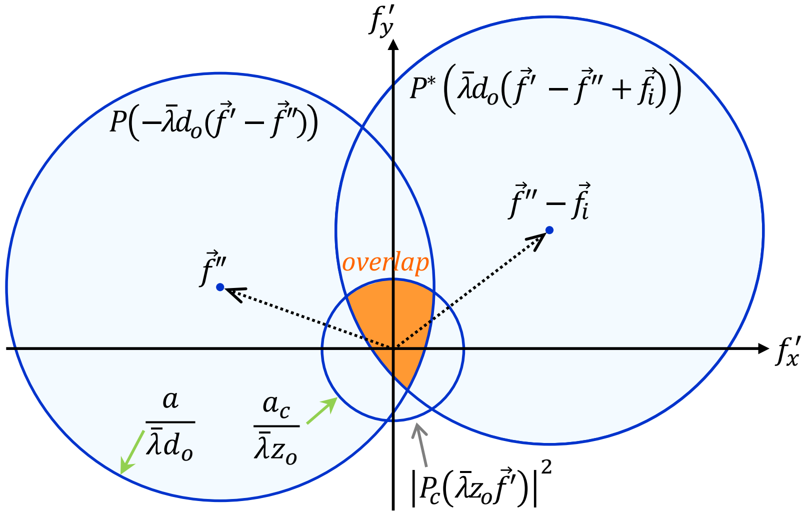

Figure 2.4: Geometrical interpretation of TCC (transmission cross-coefficient) in partial coherent imaging as an overlap of three scaled pupils in spatial frequency domain. The scaled pupil radii of imaging and condenser optics are $a/(\bar{\lambda}d_o)$ and $a_c/(\bar{\lambda}z_o)$, respectively.

This is geometrically an overlap of the three pupils, as illustrated in Fig. 2.4. The TCC may be normalized by $C(\vec{0},\vec{0})$. Also, it is worth noting that Eq. (2.34) can be reduced to either the perfect coherent imaging, Eq. (2.18) by setting $\tilde{J}_{ill}(\vec{f}')=1$, or the perfect incoherent imaging, Eq. (2.20) by setting $\tilde{J}_{ill}(\vec{f}')=\delta_{2D}(\vec{f}')$ with a proper normalization.

As a degree of partial coherence on image formation, often used is the partial coherence factor ($\sigma=NA_c/NA$) [102], which is a ratio of illumination NA to imaging NA. If $\sigma\approx 0$ (or $NA_c\ll NA$), the imaging system follows the coherent imaging theory. Incoherent imaging requires a larger condenser pupil so that the resulting coherence area at the object plane calculated from the Van Cittert-Zernike theorem is much smaller than the optical resolution (Airy disk area). From the TCC point of view in Fig. 2.4, if $a_c\geq a+\bar{\lambda}d_o|\vec{f}''|$ [95], where $|\vec{f}''|$ may be the maximum spatial frequency of interest in the object, the condenser pupil no longer impacts on the net pupil overlap, thereby entering the incoherent imaging regime. This argument leads to $\sigma\geq 1+|\vec{f}''|\bar{\lambda}/NA$.

Partial coherence imaging theory is mathematically quite complicated. As stated in the beginning of this section, if the source is incoherent, the image intensity could be alternatively obtained by an intensity superposition for each source point, that is

$$\begin{aligned} I_i(\vec{x}_i) = \iint I_s(\vec{x}_s) \iiiint & g(\vec{x}_i,\vec{x}_{o1})g^*(\vec{x}_i,\vec{x}_{o2})\, t(\vec{x}_{o1})t^*(\vec{x}_{o2}) \\ & \times g_c(\vec{x}_{o1},\vec{x}_s)g_c^*(\vec{x}_{o2},\vec{x}_s)\, d^2\vec{x}_{o1}d^2\vec{x}_{o2}\, d^2\vec{x}_s. \end{aligned} \tag{2.37}$$

Here the concept of mutual intensity propagation is omitted, yet the quasimonochomatic assumption still has to be satisfied.

Before closing, it is worth noting that the partial coherent imaging theory introduced here may not totally cover the imaging theory of wide-field fluorescence microscopy. In fluorescence imaging, dye molecules incoherently emit spherically uniform light, if free to rotate, on a time-averaged basis. As long as the excitation power density is below a saturation threshold of the dyes, the incoherent imaging theory can be applied, together with the excitation intensity distribution multiplied to the object intensity transmittance (or fluorescence strength).

2.4 Three-dimensional scalar image formation theory

Three-dimensional imaging theory takes care of a thick object whose transmittance is $t(\vec{x_o}) = t(x_o, y_o, z_o)$ under the first Born approximation [100]. This weakly scattering assumption is valid if the object is semi-transparent and has negligible secondary diffraction [90]. Then each xy-section on the object is independently considered as a thin object $t(x_o, y_o, z_o = z_{o1})$, and the image field would be a superposition of all image fields from each sections. To do this, one needs to consider small defocus perturbations on object and image distances in the thin lens imaging situation in Fig. 2.2: $d_o = d_O - z_o$ and $d_i = d_I + z_i$ where $1/d_O + 1/d_I = 1/f$ and $M = -d_I/d_O$. With these in mind, a similar approach to the 2D image formation in Section 2.2 is carried out using the Fresnel diffraction integral.

In *coherent imaging* case, the 3D image field could be derived as

$$\begin{aligned} E_i(x_i, y_i, z_i) =& \frac{ie^{ik(d_O+d_I)}}{\lambda^2 d_o d_i} e^{\frac{ik}{2d_i}(x_i^2+y_i^2)} e^{ikz_i} \iiint_{S_o} \iint_{\Sigma} E_o(x_o, y_o, z_o) e^{-ikz_o} \mathcal{P}(\xi, \eta) e^{\frac{ik}{2d_o}(x_o^2+y_o^2)} \\ & \times e^{\frac{ik}{2d_O^2}\left(z_o - \frac{z_i}{M^2}\right)(\xi^2+\eta^2)} e^{-\frac{ik}{d_O}\left[\xi(x_o - x_i/M) + \eta(y_o - y_i/M)\right]} \, d\xi d\eta \, dx_o dy_o dz_o. \end{aligned} \tag{2.38}$$

By defining a 3D amplitude PSF as

$$h(x, y, z) = \frac{ie^{ik(d_O+d_I)}}{\lambda^2 d_o d_i} e^{-\frac{ikM}{2d_O}(x^2+y^2)} \iint_{\Sigma} \mathcal{P}(-\xi_r, -\eta_r) e^{-\frac{ik}{2d_O^2} z(\xi_r^2+\eta_r^2)} e^{-\frac{ik}{d_O}(x\xi_r + y\eta_r)} \, d\xi_r d\eta_r, \tag{2.39}$$

which is a 2D Fourier transform of the defocused pupil function $\mathcal{P}(-\xi_r, -\eta_r) e^{-\frac{ik}{2d_O^2} z(\xi^2+\eta^2)}$, the field for a 3D object in a new image coordinate scaled down to the object coordinate of interest in microscopy, $(x, y, z) \equiv (x_i/M, y_i/M, z_i/M^2)$, is given approximately as

$$E_i(x, y, z) = e^{ikM^2 z} e^{\frac{ik}{2d_o}(x^2+y^2)} \iint_{\Sigma} E_o(x_o, y_o, z_o) e^{-ikz_o} h(x - x_o, y - y_o, z - z_o) \, dx_o dy_o dz_o, \tag{2.40}$$

which is a 3D convolution integral of an effective object function [90], $E_o(x_o, y_o, z_o) e^{-ikz_o}$, with the 3D amplitude PSF. The added factor e^{-ikz_o} reflects the reduced optical path length for a defocused object location by z_o. Assuming the space-invariant PSF, the linear systems approach can be equally applied in three-dimensional image formation as well. The image intensity for a coherent object $E_o(\vec{x}_o)$ is expressed as

$$I_i(\vec{x}) = \Big| \iint_\Sigma E_o(\vec{x_o}) e^{-ikz_o} h(\vec{x} - \vec{x}_o)\, d^3\vec{x}_o \Big|^2, \tag{2.41}$$

which exactly returns $|h(\vec{x})|^2$ for a point object $\delta_{3D}(\vec{x}_o)$. The axial response $h(0,0,z)$ of the PSF for a uniform circular aperture system is proportional to $sinc\big(\frac{kz}{4}\frac{a^2}{d_I^2}\big)$. The radius of its mainlobe is $2\lambda(d_I/a)^2$ or roughly $2\lambda/NA^2$. The 3D PSF is thus an axially elongated ellipsoid whose ellipticity (=$\mathrm{PSF}_z/\mathrm{PSF}_{xy}$) scales with NA^{-1}.

In spatial frequency domain, the Fourier transform of Eq. (2.40), if the pre-phase factor is neglected, yields $\tilde{E}_i(f_x, f_y, f_z) = \tilde{E}_o(f_x, f_y, f_z{+}1/\lambda)\, H(f_x, f_y, f_z)$. Setting the origin of the frequency coordinate based on the object spectrum, it can be modified to

$$\tilde{E}_i(f_x, f_y, f_z{-}1/\lambda) = \tilde{E}_o(f_x, f_y, f_z)\, H(f_x, f_y, f_z{-}1/\lambda), \tag{2.42}$$

where $H(\vec{f})$ is a 3D coherent transfer function (CTF) defined as the 3D Fourier transform of the 3D amplitude PSF:

$$H(\vec{f}) = \mathcal{F}\{h(\vec{x})\} = \mathcal{P}(\lambda d_O f_x, \lambda d_O f_y)\delta\Big(f_z + \frac{\lambda(f_x^2 + f_y^2)}{2}\Big). \tag{2.43}$$

There is an axial frequency shift by $1/\lambda$ originated from the phase factor e^{-ikz_o}. Thus in frequency domain, the image field is calculated by an inverse Fourier transform of the object spectrum multiplied by the axially shifted 3D CTF. The shape of the 3D CTF, inferred from Eq. (2.43), is a cap of a paraboloid due to the quadratic phase term of the defocus in the paraxial approximation. For a circular aperture system, the paraboloid extends laterally to $a/(\lambda d_O) \approx NA/\lambda$ and axially to $a^2/(2\lambda d_O^2) \approx NA^2/(2\lambda)$.

For convenience, the physical spatial frequency may be normalized with a medium wavelength such that $\vec{m} \equiv \lambda\vec{f}$ where $\vec{m} = (m, n, s)$ and $|\vec{m}| = 1$. The dimensionless spatial frequency $\vec{m}$ is physically related to the directional cosine of the propagating wave originated from an object containing a structural frequency of $\vec{f}$. In the normalized frequency, the 3D CTF for the circular aperture is given by

$$H(\vec{m}) = H(l, s) = \mathcal{P}(d_O l)\delta(s + l^2/2), \tag{2.44}$$

where $l{=}\sqrt{m^2 + n^2}$ is a normalized radial frequency. Thus, $0{\le}l{\le}NA$ and $0{\le}|s|{\le}NA^2/2$.

In *incoherent imaging* case, the image intensity is expressed as

$$I_i(\vec{x}) = \iint_\Sigma I_o(\vec{x}_o)|h(\vec{x} - \vec{x}_o)|^2\, d^3\vec{x}_o, \tag{2.45}$$

which is an 3D convolution integral of the object intensity with the 3D intensity PSF $|h(\vec{x})|^2$. There is no phase relation among any points in the incoherent object, and thus the phase factor e^{-ikz_o} that appeared in coherent imaging vanishes here. Thus in the frequency domain, the frequency content of the image intensity is $\tilde{I}_i(\vec{m}) = \tilde{I}_o(\vec{m})\mathcal{H}(\vec{m})$, where the 3D optical transfer function (OTF) is defined as the 3D Fourier transform of the 3D intensity PSF, or an autocorrelation of the 3D CTF, as

$$\mathcal{H}(\vec{m}) = \mathcal{F}\{|h(\vec{x})|^2\} = H(\vec{m}) \star_{3D} H(\vec{m}). \tag{2.46}$$

This can be also thought as a 3D convolution of the 3D CTF, $H(\vec{m})$, with its inverse conjugate function, $H^*(-\vec{m})$. For a circular aperture and aberration-free system, the 3D OTF is geometrically an overlap of the system's pupil (a paraboloidal cap) with its axially flipped pupil. The overlap occurs mostly as an arc within the frequency support whereas as an area at the zero pupil shift, implying much higher magnitude at the origin. In fact, the 3D OTF has a singularity at the zero frequency (see Fig. 2.5). This physically means that there is no imaging for a thick planner object ($l = 0$).

A thick object, if not varying along the z direction, has only lateral frequency contents, and thus interacts with a slice of the 3D OTF, *i.e.*, $\mathcal{H}(m, n, 0)$. Contrarily, an in-focus thin object assumed in the 2D imaging theory contains all the axial frequency components uniformly, thereby being affected over the whole axial depth of the 3D OTF. For such a conventional thin object, the 3D CTF and OTF are reduced to the 2D CTF and OTF if projected along the axial frequency direction upon the projection-slice theorem of the Fourier transform [90], *e.g.*, $H(l) = \int H(l, s)\, ds$.

The PSF plays a key role on image formation, and thus it is critical to have a better PSF model of an imaging system. Compared to the paraxial approximation, the scalar Debye approximation yields a more accurate PSF at high NA as it considers the apodization properly. High NA microscope objective lenses, designed to meet the Abbe's sine condition [100], induces an energy projection factor of $\sqrt{n_{\text{inc}}/n_f \cos\theta}$ [104, 105] upon focusing of the

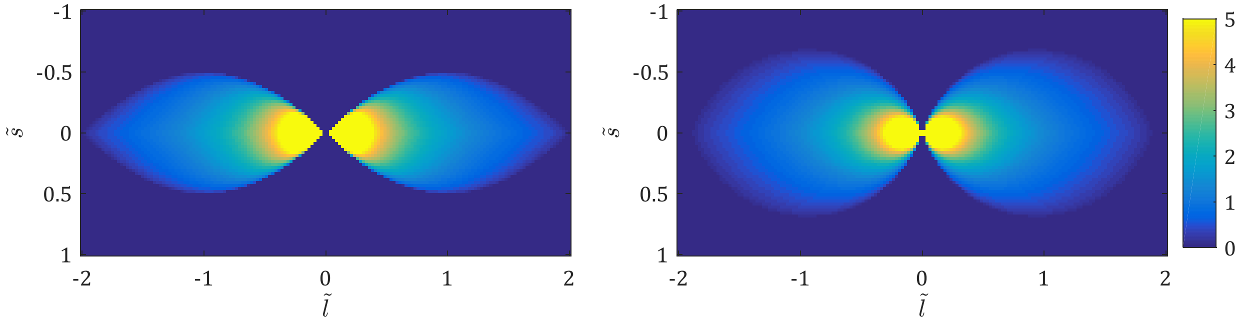

Figure 2.5: Scalar 3D OTF for a circular aperture imaging system: (left) paraxial approximation and (right) Debye approximation ($\alpha = 71.8°$ for 0.95 NA, aplanatic). Here, spatial frequencies are normalized as $(\tilde{l}, \tilde{s}) = \left(\sqrt{f_x^2 + f_y^2}/(NA/\lambda), f_z/(NA^2/\lambda)\right)$. Analytical expressions of $\mathcal{H}(\tilde{l}, \tilde{s})$ are available at [103], with doughnut-shaped passbands: (left) $|\tilde{s}| \leq |\tilde{l}|(1 - |\tilde{l}|/2)$, (right) $\tilde{l}^2 + \tilde{s}^2 \leq 2(|\tilde{l}| \sin\alpha - |\tilde{s}| \cos\alpha)$.

field, where θ is an angle of light rays w.r.t. the optical axis, and n_{inc}/n_f is a refractive index ratio of media before and after the lens. Addressing the definition of coherent transfer function (CTF) as the Fourier transform of the amplitude PSF, the non-paraxial 3D CTF can be formulated [90] as

$$H(\vec{m}) = H(l, s) = \frac{\mathcal{P}(f_o l)}{\sqrt{1-l^2}} \delta(s + \sqrt{1-l^2}), \tag{2.47}$$

where f_o may be a focal length of the aplanatic objective lens. The apodization factor is reflected here in the denominator as $\sqrt{1-l^2}$. The shape of 3D CTF is no longer a cap of a paraboloid; rather it is a cap of the Ewald sphere [106], with the axial bandwidth changed. The 3D OTF can be predicted from the autocorrelation of the 3D CTF. No analytical expressions for the nonparaxial 2D CTF and OTF were found, but they can be numerically calculated from the axial projection of these 3D transfer functions.

2.5 Vectorial image formation theory

The beauty of the paraxial approximation in scalar diffraction theory may be that for a given object field it enables relatively easier tracing of the field throughout the optical system up to the image plane. And as a result, it tells you that (coherent or incoherent) image formation is linear; the image equation is derived simply as a convolution of the object with the system's PSF (which is space-invariant practically in microscopy). However, with the scalar Debye theory or the vectorial diffraction theory, it is possible to numerically trace the diffracted field, but may be hard (or probably impossible) to analytically draw a conclusion on whether the image formation is linear, primarily because of mathematical complexity associated with these rigorous theories. When it comes to partially coherent imaging, for the same reason these advanced theories would be much more challenging to apply, although their physics are not conceptually difficult. Fortunately, if fluorescent nano-beads are imaged by a microscope with a decent high NA objective lens, they typically look identical within the field of view. Therefore, empirically one may assume the space invariance of the PSF, and consider the image formation still roughly as a linear process. Then the only important information to know is narrowed down to a knowledge of the PSF of the imaging system.

A prediction of an accurate PSF is essential not only in the design phase of microscopy development but also in post-image processing stage. For example, the optical resolution of STED microscopy is very sensitive to PSF (especially for the depletion beam) which certainly requires a design optimization. Also, image deconvolution (or any other inverse image problems) for resolution improvement relies hugely on the accuracy of the PSF model used. The PSF of a microscopy method provides useful information on a resolving power in terms of one-point or two-point resolution, as well as in spatial frequency perspective the MTF and cutoff frequency from the transfer function (the Fourier transform of the PSF).

The vectorial diffraction theory plays a key role in accurately predicting the PSF. In applying it to imaging systems, it is not necessary to trace the diffracted field plane by plane since the optical diffraction is exclusively dominated at the physical stop, or equivalently the exit pupil, of the image system. Thus one needs to figure out the field distribution at the exit pupil for an on-axis point source, and apply the vectorial diffraction integral only once there. Many studies demonstrate how to calculate the light field near focal regions [81, 105, 107, 108] at high-aperture systems based on the vector diffraction theory, including effects of aberrations [109–112] and index-mismatches in stratified media [113]. As it handles the polarization state of the field correctly, the prediction agrees with experimental results much better than when predicted with the scalar (Debye) theory. While a light propagates through the system, its polarization state changes upon optical components such as polarizers, retarders, phase modulators, and lenses. A mathematical procedure, called polarization ray tracing [114, 115] using the generalized Jones matrix formalism (see the following section), tracks down these changes in geometrical optics point of view, to obtain three orthogonal components (x, y, z) of electric fields at the exit pupil. Then they are plugged into to the vector diffraction integral to yield three independent PSFs (called vectorial PSF). Thus, effectively there exist three effective pupil functions for electric fields (another three for magnetic fields). These are termed as vectorial pupil functions [116], and their Fourier transform results in the vectorial PSF as implied by the vectorial Debye integral. Analytical expressions for vectorial PSFs for a circular aperture with a few simple polarization states were already well studied. Borrowing the concept of OTF in the scalar theory as a Fourier transform of the space-invariant PSF, the vectorial OTF could be also introduced from the Fourier transform of the vectorial PSFs in a broader sense [117]. Or it can be also obtained by summing three autocorrelations of the vectorial pupils [116, 117]. No known analytical expressions for the vectorial OTF were found. However, there is a subtle issue using these concepts as a generalized analysis tool in high NA imaging, because depolarizations at the object need to be incorporated in the image formation [116] which is nontrivial. Yet, these concepts offer better insight on what is happening on the imaging system under development and thus are still useful.

2.6 Polarization ray tracing

In order to address the vectorial nature of light in an imaging system, electric fields at the system's pupil have to be identified prior to evaluations of the vectorial diffraction integrals. Similar to a ray tracing technique in geometrical optics, polarization ray tracing using the generalized Jones matrix formalism traces the polarization state of light from the source to the the pupil in a three-dimensional way. Prior works [82, 118, 119] introduce several matrices for the systematic polarization tracing, but the signs of the traced fields seem physically inconsistent in some cases. Here, new sign conventions for those matrices are proposed as follows.

First, it is convenient to rotate the Cartesian coordinate (x, y, z), where the field is defined, with respect to the optical axis (z) so that a ray vector of consideration lies on the meridional plane. A default Cartesian coordinate in this dissertation, as illustrated in Fig.

2.2, is set: the x is horizontal (heading into the paper), the y is vertical, and the z is optical axis (to the right). Then, a coordinate rotation matrix $\mathbb{R}$ is given by

$$\mathbb{R}(\phi) = \begin{bmatrix} \cos\phi & \sin\phi & 0 \\ -\sin\phi & \cos\phi & 0 \\ 0 & 0 & 1 \end{bmatrix}, \tag{2.48}$$

where ϕ is an angle from the default x axis to the meridional plane (positive when revolved counterclockwise (CCW) about the z axis). Then the rotated xz-plane becomes the meridional plane for the ray, and the field is also separated into meridional and sagittal components.

Second, upon a refraction of a ray within the meridional plane, applied is a ray bending matrix $\mathbb{L}(\theta)$ for the refraction angle θ (positive if clockwise (CW) bending about the rotated y axis):

$$\mathbb{L}(\theta) = A(\theta) \begin{bmatrix} \cos\theta & 0 & -\sin\theta \\ 0 & 1 & 0 \\ \sin\theta & 0 & \cos\theta \end{bmatrix}. \tag{2.49}$$

This operation properly manages the depolarization in the meridional field upon the refraction, while maintaining the sagittal field unaffected. This matrix is typically for a lens and neglects any minor phase change and transmission loss inside the lens material. The apodization factor, $A(\theta)$, can be added to the matrix.

Third, in order to consider the Fresnel reflection/transmission at an interface (such as dielectric media and metallic mirror), another coordinate rotation matrix $\mathbb{D}$ that converts the field into p- and s-components is used as

$$\mathbb{D}(\theta) = \begin{bmatrix} \cos\theta & 0 & \sin\theta \\ 0 & 1 & 0 \\ -\sin\theta & 0 & \cos\theta \end{bmatrix}, \tag{2.50}$$

where θ is positive when rotated clockwise (CW) about the y axis. If properly converted from (x, y, z) to (p, s, ζ), the field is normal to $\vec{\zeta}$ (transverse) and contains the zero ζ component. For the same θ, $\mathbb{D}^{-1}(\theta) = \mathbb{L}(\theta)$.

Fourth, once the field is transformed into the (p, s, ζ) basis, any reflection/transmission can be accounted by applying

$$\mathbb{R}_F = \begin{bmatrix} r_p & 0 & 0 \\ 0 & r_s & 0 \\ 0 & 0 & r_p \end{bmatrix} \text{ and } \mathbb{T}_F = \begin{bmatrix} t_p & 0 & 0 \\ 0 & t_s & 0 \\ 0 & 0 & t_p \end{bmatrix}, \tag{2.51}$$

where the Fresnel coefficients (r_p, r_s, t_p, t_s) are found in [120]. Please note that some reference [121] defines these coefficients under different coordinate definition and thus requires a proper handedness inversion.

In addition, the generalized Jones matrix for a linear polarizer whose transmission axis is at an angle of γ from the horizontal x axis is represented [82] as

$$\mathbb{P}(\gamma) = \begin{bmatrix} \cos^2\gamma & \sin\gamma\cos\gamma & 0 \\ \sin\gamma\cos\gamma & \sin^2\gamma & 0 \\ 0 & 0 & 1 \end{bmatrix}, \tag{2.52}$$

while the generalized Jones matrix for a phase retardation plate is denoted [82, 122] as

$$\mathbb{W}(\gamma) = \begin{bmatrix} \cos\frac{\delta}{2} + i\cos(2\gamma)\sin\frac{\delta}{2} & i\sin(2\gamma)\sin\frac{\delta}{2} & 0 \\ i\sin(2\gamma)\sin\frac{\delta}{2} & \cos\frac{\delta}{2} - i\cos(2\gamma)\sin\frac{\delta}{2} & 0 \\ 0 & 0 & 1 \end{bmatrix}, \tag{2.53}$$

where δ is the relative retardation between the fast and slow axes and γ is the azimuthal angle of the fast axis from the x axis.

Compared to the prior research [82, 118, 119], the $\mathbb{L}(\theta)$ and the $\mathbb{P}(\theta)$ have opposite sign conventions here. Using the matrices above, several case examples of the polarization ray tracing follow.

Example of light focusing and collimation

In case of light focusing by a lens (neglecting its apodization) in Fig. 2.6(left), the the initial field $\vec{E}_i$ and the focused field $\vec{E}_f$ in the Cartesian coordinate are related by

$$\vec{E}_f = \mathbb{R}^{-1}(\phi)\mathbb{L}(\theta)\mathbb{R}(\phi)\vec{E}_i. \tag{2.54}$$

For a ray $\vec{k}_i = k_0[0;0;1]$ with a field $\vec{E}_i = E_0[0;1;0]$ at $\phi = \pi/2$ (the yz meridional plane), the field at focus is $\vec{E}_f = E_0[0;\cos\theta;\sin\theta]$. The physical signs of this results are correct because, for the initial field with positive E_y only, the final field should have positive E_y and positive E_z components as inferred in Fig. 2.6. The ray vector at focus is $\vec{k}_f = \mathbb{R}^{-1}(\pi/2)\mathbb{L}(\theta)\mathbb{R}(\pi/2)\vec{k}_i =$

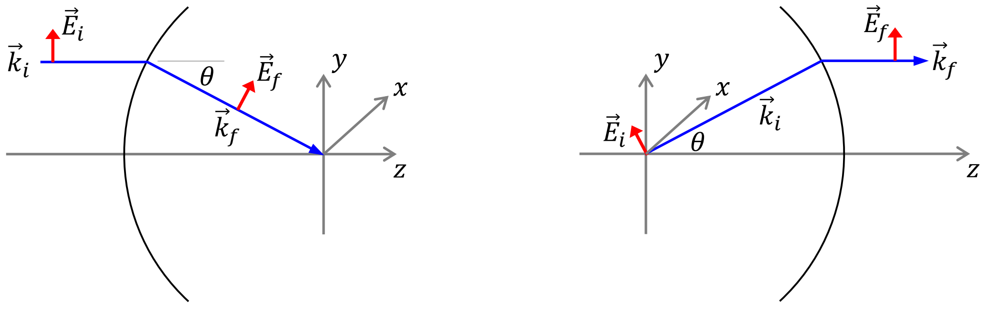

Figure 2.6: Simple examples of polarization ray tracing: (left) light focusing and (right) light collimation cases. The fields refracts at a lens modeled as a spherical surface.

$k_0[0;-\sin\theta;\cos\theta]$, whose physical direction is also correct. If the lens satisfies the sine condition, $A(\theta)=\sqrt{\cos\theta}$ (with the same media before and after the lens) can be multiplied to $\mathbb{L}(\theta)$. For dissimilar media, a constant factor of $\sqrt{n_{\text{inc}}/n_f}$ is added as explained in Section 2.4.

For the collimation case (neglecting the apodization) as shown in Fig. 2.6(right), the collimated field is calculated also as

$$\vec{E}_f = \mathbb{R}^{-1}(\phi)\mathbb{L}(\theta)\mathbb{R}(\phi)\vec{E}_i. \tag{2.55}$$

For a ray $\vec{k}_i = k_0[0;\sin\theta;\cos\theta]$ with an initial field $\vec{E}_i = E_0[0;\cos\theta;-\sin\theta]$ at $\phi=\pi/2$ (the yz meridional plane), the field becomes $\vec{E}_f = E_0[0;1;0]$ which is again physically right. The collimated ray vector yields $\vec{k}_f = \mathbb{R}^{-1}(\pi/2)\mathbb{L}(\theta)\mathbb{R}(\pi/2)\vec{k}_i = k_0[0;0;1]$ which is also true. Here the apodization factor can be similarly added as $\sqrt{n_f/n_{\text{col}}}\cos^{-\frac{1}{2}}\theta$ for an aplanatic lens where n_{col} denotes the refractive index of the medium at the collimated space. Also, one can check that $\mathbb{D}(-\phi)\mathbb{R}(\phi)\vec{E}_i$ leads to $E_\zeta=0$ as anticipated.

Example of imaging

In an image case with a dipole point source, $\vec{p}$, located at the origin of the object space in Fig. 2.7, the far-field radiation field is $\vec{E}_i = -\vec{k}_i\times(\vec{k}_i\times\vec{p})$ [86], where a general ray vector is $\vec{k}_i = k_o[\sin\theta\cos\phi;\sin\theta\sin\phi;\cos\theta]$ in the spherical object coordinate. Then the collimated field after the first aplanatic lens is calculated as

$$\begin{aligned}\vec{E}_c &= \frac{1}{\sqrt{\cos\theta_1}}\mathbb{R}^{-1}(\phi)\mathbb{L}(\theta_1)\mathbb{R}(\phi)\vec{E}_i \\ &= \frac{1}{\sqrt{\cos\theta_1}}\begin{bmatrix}\cos\theta_1\cos^2\phi+\sin^2\phi & (\cos\theta_1-1)\cos\phi\sin\phi & -\sin\theta_1\cos\phi \\ (\cos\theta_1-1)\cos\phi\sin\phi & \cos\theta_1\sin^2\phi+\cos^2\phi & -\sin\theta_1\sin\phi \\ 0 & 0 & 0\end{bmatrix}\vec{p},\end{aligned} \tag{2.56}$$

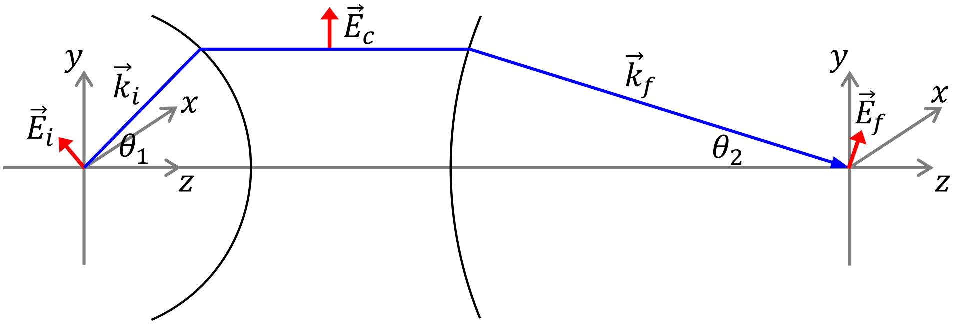

Figure 2.7: Example of polarization ray tracing for a simplified imaging system comprising an objective lens (left) and a tube lens (right) in air.

which is a collimated wave (no z component) as expected. And the field at the image space can be evaluated as

$$\begin{aligned} \vec{E}_f &= \sqrt{\frac{\cos\theta_2}{\cos\theta_1}}\mathbb{R}^{-1}(\phi)\mathbb{L}(\theta_2)\mathbb{L}(\theta_1)\mathbb{R}(\phi)\vec{E}_i \\ &= \sqrt{\tfrac{\cos\theta_2}{\cos\theta_1}}\begin{bmatrix} \cos\theta_1\cos\theta_2\cos^2\phi+\sin^2\phi & (\cos\theta_1\cos\theta_2-1)\cos\phi\sin\phi & -\sin\theta_1\cos\theta_2\cos\phi \\ (\cos\theta_1\cos\theta_2-1)\cos\phi\sin\phi & \cos\theta_1\cos\theta_2\sin^2\phi+\cos^2\phi & -\sin\theta_1\cos\theta_2\sin\phi \\ \cos\theta_1\sin\theta_2\cos\phi & \cos\theta_1\sin\theta_2\sin\phi & -\sin\theta_1\sin\theta_2 \end{bmatrix}\vec{p}. \end{aligned} \tag{2.57}$$

As a verification, if $\theta_1 = \theta_2 = \theta$ as a unit magnification system, the ray vector at the image space becomes $\vec{k}_f = k_o[-\sin\theta\cos\phi; -\sin\theta\sin\phi; \cos\theta]$ whose signs physically make sense. Also, it can be shown that $\vec{E}_f = (E_{ix}, E_{iy}, -E_{iz})$ which is geometrically correct.

All of the case studies above clearly shows that the polarization ray tracing with the sign convention defined here leads to correct output fields without any physical/geometrical inconsistency. The field calculated here is used to evaluate the vectorial diffraction integrals.

2.7 Numerical comparison: vector vs. scalar theory

This section shows an effectiveness of the vectorial theory in high aperture optical systems over the scalar theory. As an example, consider light focusing by a lens ($NA \approx a/f$) in air with a uniform, vertically polarized field. In scalar paraxial theory, from Eq. (2.9) the field around the focus in a cylindrical coordinate is derived, with a help of the formula[1] [107] or in [118], as

$$E(\rho,\phi',z) = \frac{2\pi a^2}{i\lambda f}\int_0^1 e^{-\frac{ika^2}{2f^2}z\rho_\xi^2} J_0\Big(\frac{ka}{f+z}\rho\rho_\xi\Big)\rho_\xi d\rho_\xi. \tag{2.58}$$

The scalar Debye theory, on the other hand, from Eq. (2.10) yields

$$E(\rho,\phi',z) = \frac{2\pi}{i\lambda}\int_0^\alpha \sqrt{\cos\theta}\, e^{ikz\cos\theta} J_0(k\rho\sin\theta)\sin\theta d\theta, \tag{2.59}$$

where $\alpha = \sin^{-1}(NA/n)$ and $\sqrt{\cos\theta}$ is the apodization. In vectorial diffraction theory, the field over the exit pupil is traced as $\vec{E}_s = e^{-ikf}/f\sqrt{\cos\theta}[(\cos\theta-1)\sin\phi\cos\phi; \cos\theta\sin^2\phi + \cos^2\phi; \sin\theta\sin\phi]$, and if plugged into Eq. (2.6), the focus field is derived as

$$\vec{E}(\rho,\phi',z) = \frac{\pi}{i\lambda}\int_0^\alpha \sqrt{\cos\theta}\begin{bmatrix} \sin(2\phi')(1-\cos\theta)J_2(k\rho\sin\theta) \\ (1+\cos\theta)J_0(k\rho\sin\theta) - (1-\cos\theta)J_2(k\rho\sin\theta)\cos(2\phi') \\ -2i\sin\phi'\sin\theta J_1(k\rho\sin\theta) \end{bmatrix} e^{ikz\cos\theta}\sin\theta d\theta. \tag{2.60}$$

The derived equations indicate that the scalar theory leads to a radially symmetric intensity distribution while the vectorial theory produces laterally anisotropic distribution, *i.e.*, a

---

[1] $\int_0^{2\pi}\begin{bmatrix}\cos(n\phi)\\ \sin(n\phi)\end{bmatrix} e^{it\cos(\phi-\phi')}\, d\phi = 2\pi i^n J_n(t)\begin{bmatrix}\cos(n\phi')\\ \sin(n\phi')\end{bmatrix}$, where n is an integer.

function of ϕ', for the linearly polarized input. Figure 2.8 shows the in-focus intensity PSF at 0.95 NA with $\lambda = 0.5\,\mu m$. Compared to the paraxial theory, adding the apodization in the scalar Debye theory minorly decreases PSF by about 4%. The vectorial PSF is elongated along the input polarization direction mainly due to the remarkable contribution from E_z (see Fig. 2.8). The full-width at half-maximum (FWHM) is around 33% broader along z and around 8% narrower along x than the paraxial FWHMs, respectively. Further analysis (not shown here) reveals that a portion of light power to I_z increases to 24.3% at 0.95 NA. Also, a deviation of the vectorial FWHM_y from the paraxial FWHM starts to exceed 10% at 0.67 NA.

As for the axial response of $E(0,0,z)$, from Eq. (2.60) the depolarized fields (E_x and E_z) by the lens cancel out and the on-axis vectorial PSF is solely determined by the E_y field. The reduced integral has an additional correction of $(1+\cos\theta)/2$ compared to the scalar Debye version, Eq. (2.59). This on-axis result is with the vertically polarized wave but remains unchanged for any type of input polarization states. The different appearance of the paraxial defocus term in Eq. (2.58) together with an approximation of $a/f \approx NA$ leads to an overestimation of the axial PSF by 46% in FWHM (see Fig. 2.9). This huge discrepancy may be corrected by *pseudo-paraxial* approximation [81], *i.e.*, $a/f = 2\sin(\alpha/2)$, and then the

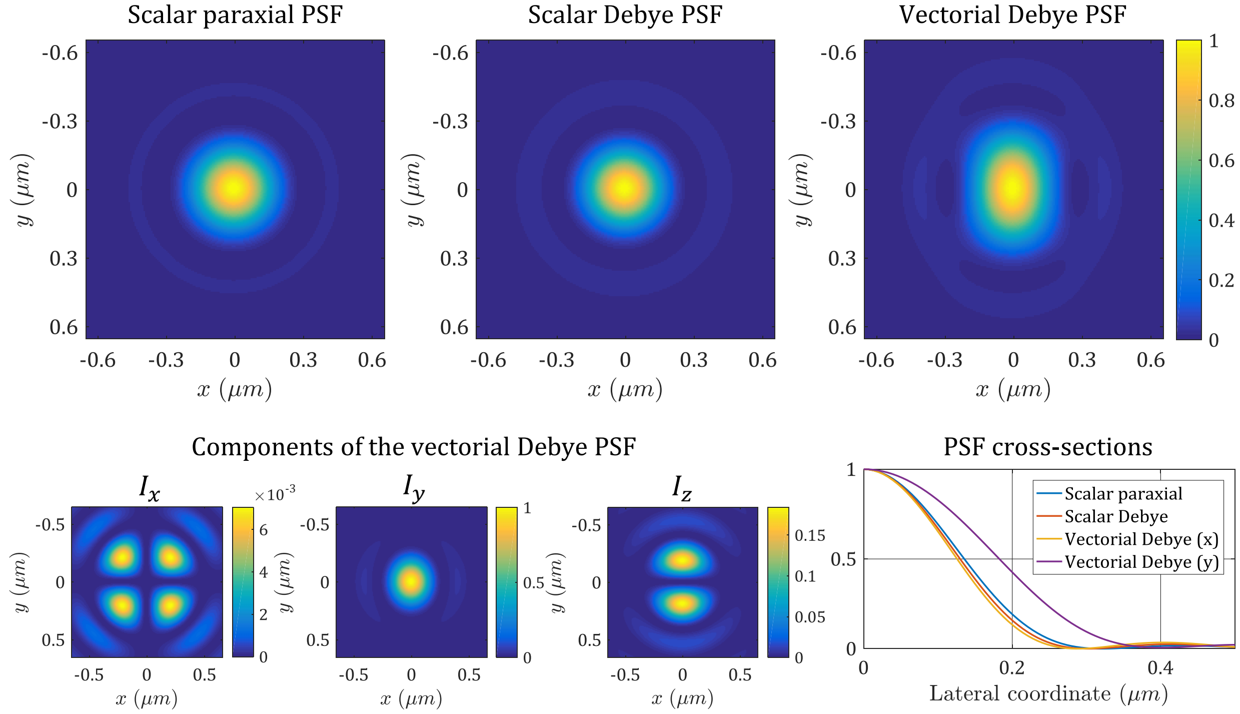

Figure 2.8: Comparison of intensity distribution at focus between scalar and vectorial diffraction theory. A collimated, uniform, vertically polarized field ($\lambda = 0.5\,\mu m$) is assumed to be focused by an aplanatic objective lens of 0.95 NA in air.

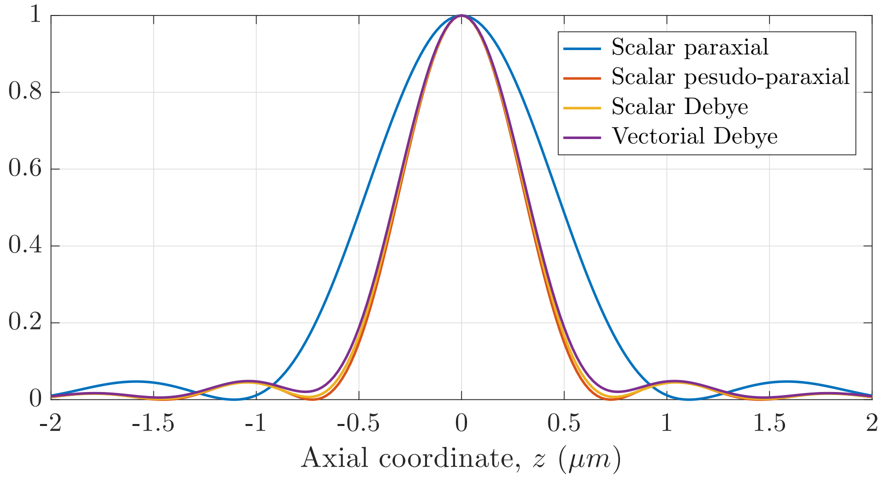

Figure 2.9: Comparison of axial intensity response between diffraction theories. Assumed is a collimated, uniform, vertically polarized field ($\lambda = 0.5\,\mu m$) incident on a 0.95 NA objective in air.

pseudoparaxial $\mathrm{FWHM_z}$ has now only 4% discrepancy compared with the vectorial FWHM. If the scalar paraxial theory is still used, a 10% overestimation in the axial FWHM begins to arise at 0.6 NA.

The simulation results clearly show the role of the vectorial approach that properly treats the polarization of the light unlike in the scalar theory. This methodology can be applied to any type of polarization states including the unpolarized state (see Chapter 4). For a broadband source, a PSF at each wavelength is first considered and the overall PSF could be obtained by summing all contributions over the spectral weighting.

Chapter 3

Oblique Plane Microscopy

While many cell-/tissue-level samples for biological study are three-dimensional, conventional wide-field optical microscopes offer only two-dimensional imaging. Scanning microscopes are capable of three-dimensional imaging but at a very slow speed. Many biological phenomena in questions occur in real-time and in three dimensions, but interestingly some of them have a principal plane of interest that is not usually aligned with the microscope's focal plane. Oblique plane microscopy (OPM) affords a cost-effective way of real-time 2D deep imaging along any plane of orientation in a 3D sample. Whereas the performance of scanning-type OPM has been studied, that of wide-field OPM has not been clearly understood yet. This chapter studies theoretical performance of wide-field oblique plane microscopy and experimentally demonstrates axial plane microscopy as a special case.

3.1 Introduction to wide-field OPM

Unlike conventional optical microscopy that images part of a specimen at the microscope's focal plane, oblique plane microscopy (OPM) [74–78, 123, 124] attempts to image an inclined section rather than the focal plane. OPM is obviously advantageous when a principal plane of the prepared sample is not in parallel with the coverslip or the focal plane [74, 77, 78], or when a living sample rapidly changes/evolves its structural orientation [78]. An extraction of oblique planar information from 3D scanning microscopy is possible but too slow due to lengthy 3D stack measurements. OPM offers a high-speed and cost-effective solution.

Commercial aplanatic objective lenses that allow only a shallow depth of field (λ/NA^2) may not seem compatible with the idea of OPM. However, an optical technique called remote focusing [125, 126] that relays two objective lenses back-to-back enables almost aberration-free 3D imaging for thick samples at the remote space. Then by putting another microscope at a tilted angle with respect to this 3D intermediate image, oblique plane imaging becomes feasible at the expense of partial usage of the pupil, thus lowering optical resolution.

Dunsby [75] roughly predicted imaging resolution of OPM from an effective NA concept, which however is not precise nor provides an analytical evidence on anisotropic lateral resolution. Anselmi *et al.* [76] demonstrated wide-field OPM by remote tilting technique, which has a simpler layout than Dunsbys. They pointed out two reasons of resolution degradation: a light clipping (vignetting in a broader sense) and an inclined detection PSF. In their experiment an oblique angle was adjusted only up to 14° where such causes are negligible, and no theoretical analysis on resolution was addressed. On the other hand, Smith *et al.* [77, 78] proposed point-scanning OPM using a remote scanning technique. They investigated anisotropic lateral resolution for all oblique angles in terms of spatial cutoff frequencies obtained from the 3D OTF. However, their approach does not apply to wide-field OPM as the scanning OPM undergoes no light clipping and its overall PSF is different. Hence accurate theoretical resolution of wide-field OPM is still open to question.

3.2 Schematic of direct oblique plane microscopy

A layout of oblique plane imaging system [76, 127] is illustrated in Fig. 3.1. The back focal planes of the two aplanatic objective lenses are connected by the L1-L2 relay optics to have

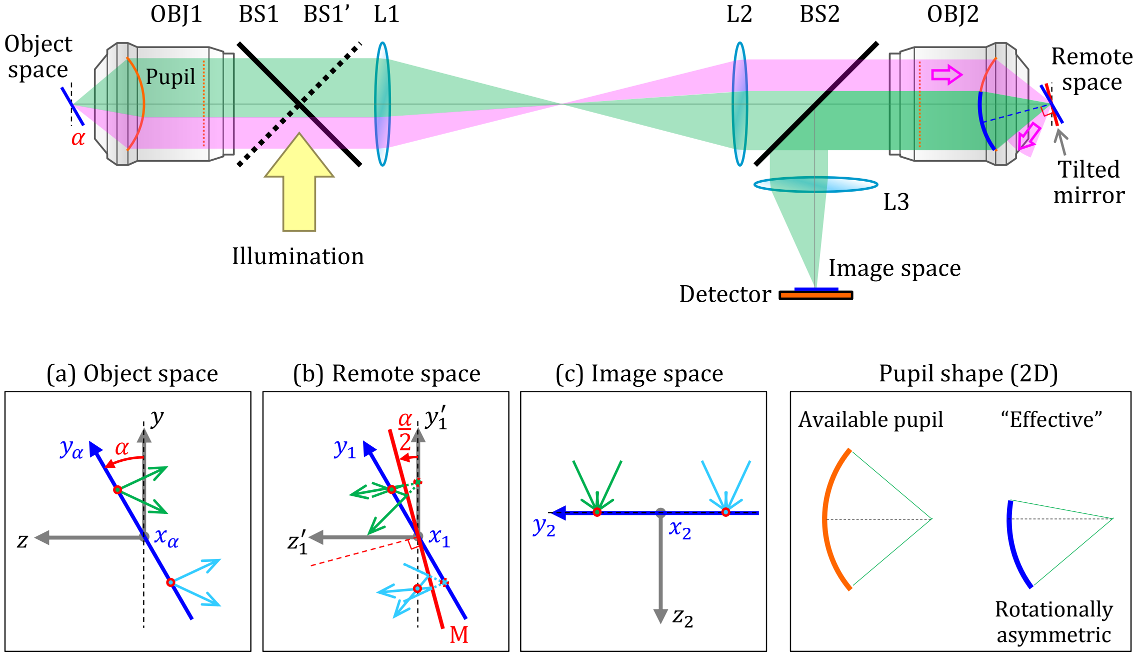

Figure 3.1: Conceptual arrangement of oblique plane imaging. OBJ: objective lens; BS: beam splitter; L: lens; M: mirror. The beam path for an on-axis point object is drawn in green, while the clipped beam at OBJ2 is shown in pink. Coordinates at (a) object space: an $x_\alpha y_\alpha$ oblique plane tilted by α about the xy focal plane of OBJ1, (b) remote space: the $x_1 y_1$ intermediate image plane is rotated to the $x_1' y_1'$ plane (OBJ2's focal plane) by the $\alpha/2$-tilted mirror, and (c) image space: the $x_2 y_2$ lateral plane is conjugate with the $x_\alpha y_\alpha$ object plane.

a 3D isotropic magnification as a ratio of object/remote medium indices. This configuration compensates for aberrated optical wavefronts originated from the defocused object positions by the pupil's odd parity condition [125, 126], thus extending the depth of field [126]. A 3D object lying within the extended range forms a diffraction-limited 3D image in the remote space. The OBJ2-L3 comprises another microscope to take an oblique plane image supported by the tilted remote mirror. Figure 3.1(a-c) elucidates that the α-tilted plane in the object space is optically conjugate with the image plane on a detector. The beam in pink in Fig. 3.1 illustrates how part of the light at the remote space is clipped at the OBJ2 caused by the tilted mirror. Such a one-dimensional light clipping that makes an effective pupil of the OBJ2 (the blue arc) rotationally asymmetric leads to an anisotropic resolution. To avoid a full light loss by the clipping, the OBJ2 should have a maximum half-cone angle or NA greater than the mirror tilt angle of $\alpha/2$. For instance, an axial plane imaging ($\alpha = 90°$) demands $NA > 0.71$ in air medium. Preferred is to use a higher NA objective to minimize both signal loss and optical resolution.

It should be noted that the optical configuration in Fig. 3.1 allows 2D imaging of any oblique plane if a tip-tilt of the small mirror M is properly controlled. Also, to shift an image plane of interest, the remote mirror could be instead translated in a three-dimensional way at no specimen agitation. Besides, the PSF formulated here for direct oblique plane imaging may be regarded as a detection PSF in other types of OPM that use either beam scanning or selective-plane illumination as long as the same light clipping occurs. Such illumination could be coupled through either BS1 or BS1' or other optical paths not illustrated in Fig. 3.1. The overall PSF of the imaging system may then be a multiplication of the according illumination and detection PSFs.

3.3 Formulation of vectorial PSF

Here a theoretical resolving power of the wide-field OPM is accurately calculated. A general 3D pupil function affected by the light clipping is mathematically derived for any oblique angle between 0° to 90°. From this, vectorial 2D intensity PSF is estimated to characterize lateral resolution. To examine the spatial cutoff frequency influenced by oblique angles, vectorial OTF was also evaluated by the Fourier transform of the PSF.

Effective pupil function

Assuming the remote NA equal to the object NA, the 3D normalized pupil function $P(\theta, \phi)$ at the pupil of the object space in a spherical coordinate is derived as follows. (In case of a remote NA larger than the object NA, see Chapter 4.) As shown in Fig. 3.2(a), an overlap of the original spherical pupil of the objective lens with its reflected pupil via a tilted virtual mirror constructs an effective pupil surface. If cut by the xy plane on the point C, the pupil surface can be divided into a rotationally symmetric part (Σ_1) and the rest asymmetric part (Σ_2). This separation is for mathematical convenience in evaluating the vectorial diffraction

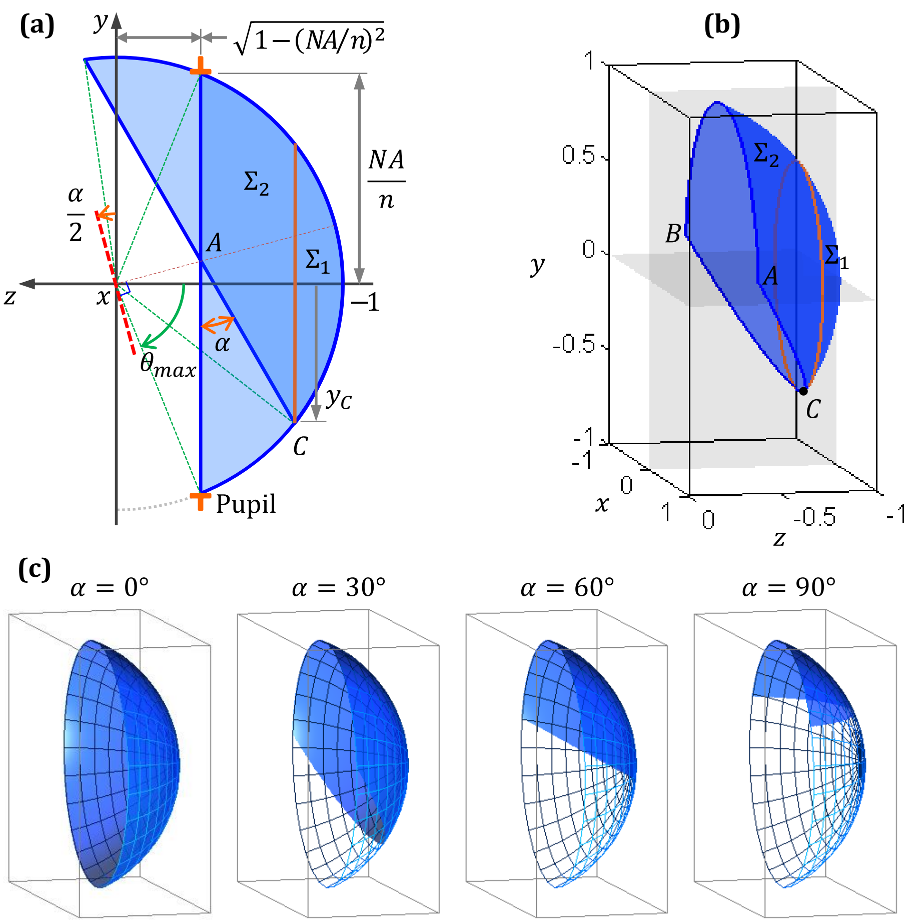

Figure 3.2: (a) 2D and (b) 3D effective pupil function in direct oblique plane imaging in a normalized object space. An areal overlap between the spherical cap of the objective's original pupil surface and its mirror image by the $\alpha/2$-tilted virtual mirror (red dashed line) forms an effective pupil. (c) Pupil functions at different oblique angles ($\theta_{\max}=67°$).

integrals. The Σ_1 ceases to exist at a higher α regime where the y-coordinate of the point C is positive ($y_C > 0$). Hence, the general pupil function for both Σ_1 and Σ_2 can be defined as

$$\begin{aligned} P_{\Sigma_1}(\theta,\phi) &= \begin{cases} 1, & \theta \in [0,\theta_C],\ \phi \in [0,2\pi], \text{ and } y_C < 0 \\ 0, & \text{otherwise} \end{cases}, \\ P_{\Sigma_2}(\theta,\phi) &= \begin{cases} 1, & \theta \in [\theta_C,\theta_{\max}] \text{ and } \phi \in [\phi_1(\theta),\phi_2(\theta)], \text{ and } y_C > 0 \\ 0, & \text{otherwise} \end{cases}, \end{aligned} \tag{3.1}$$

where the pupil boundaries of θ_C, $\theta_{\max}$, $\phi_1(\theta)$, and $\phi_2(\theta)$ are discovered as follows.

First, the coordinate of the point C in Fig. 3.2(a) is found, by plugging a plane $\overline{ABC}$ equation ($y - z\cot\alpha - \sqrt{1-(NA/n)^2}\csc\alpha = 0$) into the unit sphere equation ($x^2+y^2+z^2=1$)

at $x=0$, as

$$(x_C, y_C, z_C) = \left(0, -\frac{NA}{n}\cos\alpha + \sqrt{1-\left(\frac{NA}{n}\right)^2}\sin\alpha, -\frac{NA}{n}\sin\alpha - \sqrt{1-\left(\frac{NA}{n}\right)^2}\cos\alpha\right). \tag{3.2}$$

By setting a Cartesian-to-spherical coordinate relation to $(x, y, z) \equiv (\sin\theta\cos\phi,\ \sin\theta\sin\phi,\ -\cos\theta)$, the bounds of the pupil surface are derived as

$$\begin{aligned}
\theta_C &= \cos^{-1}|z_C| = \cos^{-1}\left|\frac{NA}{n}\sin\alpha + \sqrt{1-\left(\frac{NA}{n}\right)^2}\cos\alpha\right|,\\
\theta_{\max} &= \sin^{-1}\left(\frac{NA}{n}\right),\\
\phi_1(\theta) &= \sin^{-1}\left(\frac{y}{\sin\theta}\right) = \sin^{-1}\left|-\cot\alpha\cot\theta + \sqrt{1-\left(\frac{NA}{n}\right)^2}\csc\alpha\csc\theta\right|,\\
\phi_2(\theta) &= \pi - \phi_1(\theta),
\end{aligned} \tag{3.3}$$

where the bounds of θ, ϕ are expressed as a function of α, NA, and n. As shown in Fig. 3.2(c), the derived mathematical expressions well represent pupil functions in any oblique angle.

Vectorial PSF for a linearly polarized wave

It was clearly shown in Section 2.7 that the depolarization in a high aperture system creates a broader mainlobe of the vectorial PSF especially along the incident polarization direction than the scalar (Debye) PSF. To accurately predict optical resolution of OPM for any oblique angle and NA regime, the vectorial Debye theory is adopted here. This is simpler than the vectorial Kirchhoff integral, while still equally accurate because most of the commercial microscope objectives of any NA meet $N_F > 100$. It was confirmed that when this criterion is satisfied, the vectorial PSF obtained from between the vectorial Kirchhoff integral Eq. (2.5) and the vectorial Debye integral Eq. (2.6) has almost no discrepancy (especially in the mainlobe of PSF).

In calculating the PSF, assumed is that a uniform electric field from a quasimonochromatic point source at infinity is incident on the exit pupil of OPM. Additional assumption made here is that this field is linearly polarized at an azimuthal angle of ϕ_0 with reference to the x-axis, thus $\vec{E}_i = E_0[\cos\phi_0; \sin\phi_0; 0]$. Then the electric field at the exit pupil for the aplanatic oblique plane imaging system is calculated, using the polarization ray tracing (introduced in Chapter 2), as

$$\vec{E}_S = \sqrt{\cos\theta}\,\mathbb{R}^{-1}(\phi)\mathbb{L}(\theta)\mathbb{R}(\phi)\vec{E}_i = E_0\begin{bmatrix}\cos\theta\cos(\phi-\phi_0)\cos\phi + \sin(\phi-\phi_0)\sin(\phi)\\ \cos\theta\cos(\phi-\phi_0)\sin\phi - \sin(\phi-\phi_0)\cos(\phi)\\ \sin\theta\cos(\phi-\phi_0)\end{bmatrix}, \tag{3.4}$$

where a constant ratio of the dissimilar medium indices is neglected. Substituting this field to the vectorial Debye integral, one can calculate the electric field near focal regions in the Cartesian coordinate (x, y, z), if the prefactor is ignored, as

$$\vec{E}_{\phi_0}(x,y,z) = \oiint_{\Sigma} \vec{E}_S \sqrt{\cos\theta}\big[P_{\Sigma_1}(\theta,\phi)+P_{\Sigma_2}(\theta,\phi)\big] e^{ik(-x\sin\theta\cos\phi - y\sin\theta\sin\phi + z\cos\theta)} \sin\theta \, d\theta d\phi. \tag{3.5}$$

Since the $x_\alpha y_\alpha$ oblique plane is related to the (x, y, z) coordinate as (x, y)=$(x_\alpha$,$y_\alpha \cos\alpha - z_\alpha \sin\alpha)$, the two-dimensional, in-focus intensity PSF on the oblique plane is derived as

$$\vec{I}_{\phi_0}(x_\alpha, y_\alpha) = I_0 \left| \begin{array}{l} \displaystyle\oiint_{\Sigma} \begin{bmatrix} \cos\theta\cos(\phi-\phi_0)\cos\phi + \sin(\phi-\phi_0)\sin(\phi) \\ \cos\theta\cos(\phi-\phi_0)\sin\phi - \sin(\phi-\phi_0)\cos(\phi) \\ \sin\theta\cos(\phi-\phi_0) \end{bmatrix} \\ \quad \times \sqrt{\cos\theta}\big[P_{\Sigma_1}(\theta,\phi)+P_{\Sigma_2}(\theta,\phi)\big] \\ \quad \times e^{ik\left(-x_\alpha \sin\theta\cos\phi - y_\alpha(\cos\alpha\sin\theta\sin\phi - \sin\alpha\cos\theta)\right)} \sin\theta \, d\theta d\phi \end{array} \right|^2, \tag{3.6}$$

where $I_0 = |E_0|^2$.

Vectorial PSF for a unpolarized wave

For a unpolarized field, the above result can be still used to calculate the 2D vectorial intensity PSF [107] as

$$\vec{I} = \frac{1}{2\pi}\int_0^{2\pi} \vec{E}^*_{\phi_0} \cdot \vec{E}_{\phi_0} \, d\phi_0 = \frac{1}{2}\Big(\big|\vec{I}_C\big|^2 + \big|\vec{I}_S\big|^2\Big), \tag{3.7}$$

where $\vec{I}_C$ and $\vec{I}_S$ are expressed as

$$\vec{I}_C = I_0 \oiint_{\Sigma_1+\Sigma_2} \sqrt{\cos\theta} \begin{bmatrix} \cos\theta\cos^2\phi + \sin^2\phi \\ \cos\theta\cos\phi\sin\phi - \cos\phi\sin\phi \\ \sin\theta\cos\phi \end{bmatrix} e^{ik\left(-x_\alpha \sin\theta\cos\phi - y_\alpha(\cos\alpha\sin\theta\sin\phi - \sin\alpha\cos\theta)\right)} \sin\theta \, d\theta d\phi, \tag{3.8}$$

$$\vec{I}_S = I_0 \oiint_{\Sigma_1+\Sigma_2} \sqrt{\cos\theta} \begin{bmatrix} \cos\theta\cos\phi\sin\phi - \cos\phi\sin\phi \\ \cos\theta\sin^2\phi + \cos^2\phi \\ \sin\theta\sin\phi \end{bmatrix} e^{ik\left(-x_\alpha \sin\theta\cos\phi - y_\alpha(\cos\alpha\sin\theta\sin\phi - \sin\alpha\cos\theta)\right)} \sin\theta \, d\theta d\phi. \tag{3.9}$$

As both Eq. (3.6) and Eq. (3.7) show even symmetry about x_α and y_α, a numerical evaluation of any one quadrant is sufficient. The Eq. (3.7) can be further manipulated for faster numerical calculations as derived in Appendix B in [127]. It reduces the double integrals for the rotationally symmetric pupil (Σ_1) to the single integral regarding θ by introducing the Bessel functions for the integral over ϕ. For the asymmetric pupil (Σ_2), it uses the half of the symmetric integral bound for ϕ as $[\phi(\theta), \pi-\phi(\theta)] \rightarrow [\phi(\theta), \pi]$ and double the result.

3.4 Numerical PSF and OTF in OPM

The two same oil-immersion ($n = 1.52$) objective lenses were considered for several NAs of 1.30, 1.40, and 1.49, together with a unity magnification for the L1-L2 optics. As the Fresnel numbers of these NAs well exceed 1000, the Debye approximation is validated. A unpolarized and quasimonochromatic source at a vacuum wavelength (λ_0) of 519 nm was considered.

Vectorial PSF

The 2D intensity PSF from Eq. (3.7) was calculated as shown in Fig. 3.3. The PSF at $\alpha = 0°$ is the conventional PSF in circular aperture systems with isotropic lateral resolution.

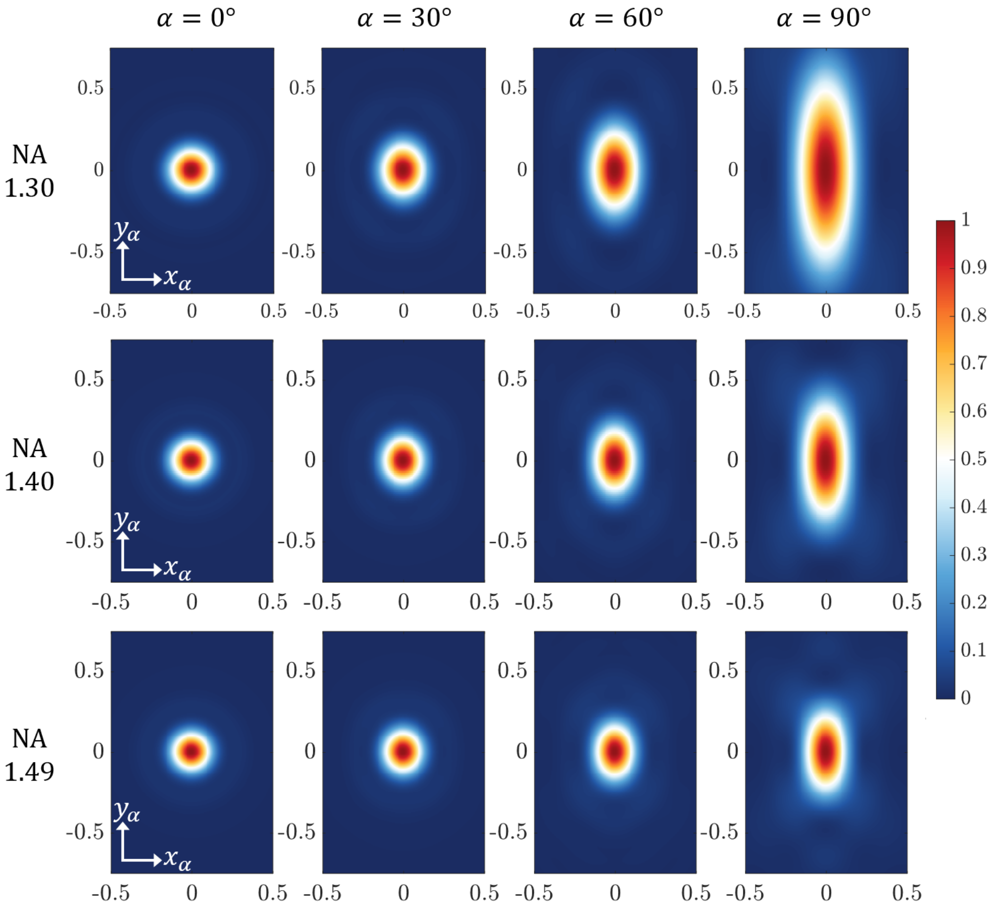

Figure 3.3: 2D vectorial intensity PSF of oblique plane imaging at different oblique angles (α) and NAs. $\lambda_0 = 519$ nm (unpolarized), $n = 1.52$ (oil immersion). The axis unit is μm. The PSF stretches vertically where the serious light clipping occurs in OPM. A higher NA improves the undesirable anisotropic resolving power.

At higher oblique angles, the mainlobe of the PSF stretches to the y_α direction more obviously because of more reduced pupils, resulting in anisotropic lateral resolving power. The simulation results also exhibit a slight PSF stretch along the x_α direction which is expected due to the minor collateral pupil loss existing along that direction as seen in Fig. 3.2(c).

The FWHM was calculated in Fig. 3.4 to quantitatively interpret the calculated PSFs. The optical resolution decreases as the oblique angle increases from $\alpha = 0^\circ$ (conventional lateral imaging) to $\alpha = 90^\circ$ (axial plane imaging) owing to the narrowed effective NA. The FWHM ratio at such two extremes with NA 1.30 (1.40, 1.49) is 1.33 (1.16, 1.06) and 4.39 (2.92, 2.09) along x_α and y_α, respectively.

Moreover, the FWHM in oblique plane imaging was compared with that obtained from the inclined PSF as illustrated in the inset in Fig. 3.4. Here, the 3D vectorial PSF in a conventional circular aperture system was rotated by α with respect to the x-axis to calculate FWHMs along that slice (which may be done misleadingly in oblique plane imaging). This way remains the FWHM along the x_α-axis unchanged (green dotted curve), while deteriorates FWHM along the y_α-axis (green line curve) stemming from the well-known "ellipsoidal" PSF. Hence the inclined PSF slows down the slope of the $\mathrm{FWHM_y}$ curve near 90° and the FWHM along the y_α-axis converges to the $\mathrm{FWHM_z}$ of the 3D PSF of the circular aperture. This behavior is certainly dissimilar from 1) the sharp rise of FWHM along the y_α direction near 90° and 2) its value not limited to the $\mathrm{FWHM_z}$ of the conventional PSF (it can be worse than that). Also the rotation of the conventional PSF fails to predict the collateral resolution loss along the x_α direction over oblique angles. It is clear that the inclined slice of the conventional 3D PSF is thus different from the light-clipped 2D PSF in wide-field OPM.

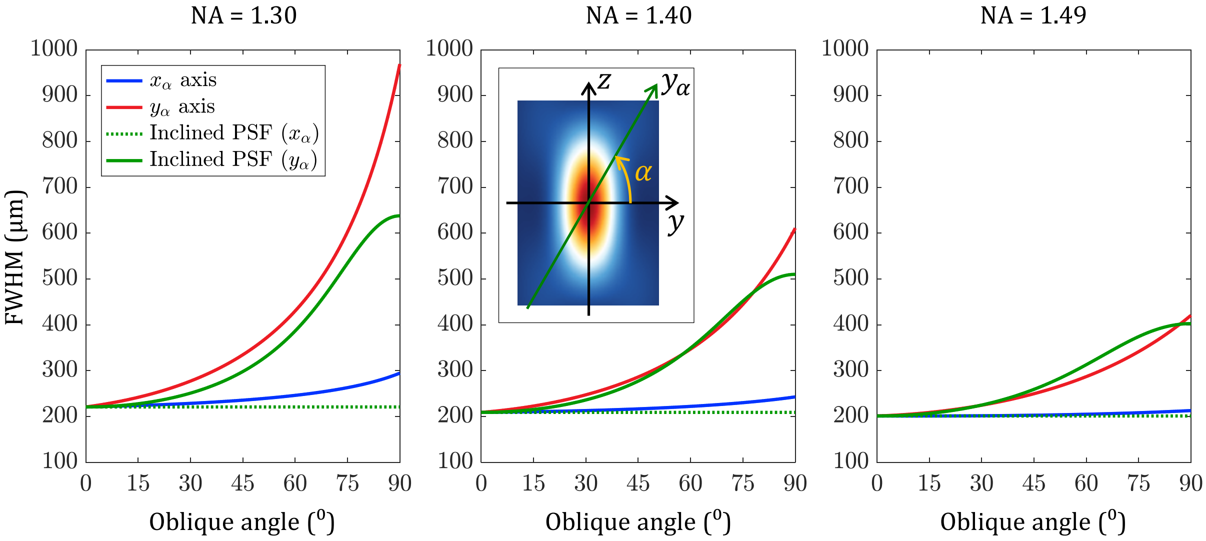

Figure 3.4: FWHM of the vectorial PSF at different NA over the oblique angle. The FWHMs from the inclined 3D vectorial PSF in a circular aperture (the inset in the middle) are plotted for comparison, which fails to explain the anisotropic resolution in wide-field OPM.

Vectorial OTF

As explained in Section 2.5, no known explicit forms of 2D or 3D vectorial OTFs were found. Yet vectorial OTFs can be numerically calculated by either the Fourier transform of the vectorial PSF or an autocorrelation of the vectorial pupil functions. Here the former method was chosen.

In order to verify an accuracy of the FFT method, the Fourier transform was performed for the scalar Debye intensity PSF for a circular aperture system ($\alpha = 0°$). Alternatively, the 2D scalar Debye OTF was also calculated by the 2D projection of the analytical scalar Debye 3D OTF with a normalization with $4\sin^2(0.5\sin^{-1}(NA/n))$. The OTFs from such two different methods were compared as shown in Fig. 3.5. It turned out that in the FFT approach PSF data with a plenty number of sidelobes is critical for exact results: although outer sidelobes have several orders lower intensity than the peak of the mainlobe, they still influence much on OTF curves particularly at low-to-middle spatial frequency regimes. A FFT-based OTF from the 2D PSF data including up to 25 sidelobes agreed well with the analytical (2D projected) OTF, with a relative error in MTF value smaller than 0.013 over the entire frequency range. An almost perfect match resulted if more than 60-sideslobes were used at the expense of 6 times or longer computational time.

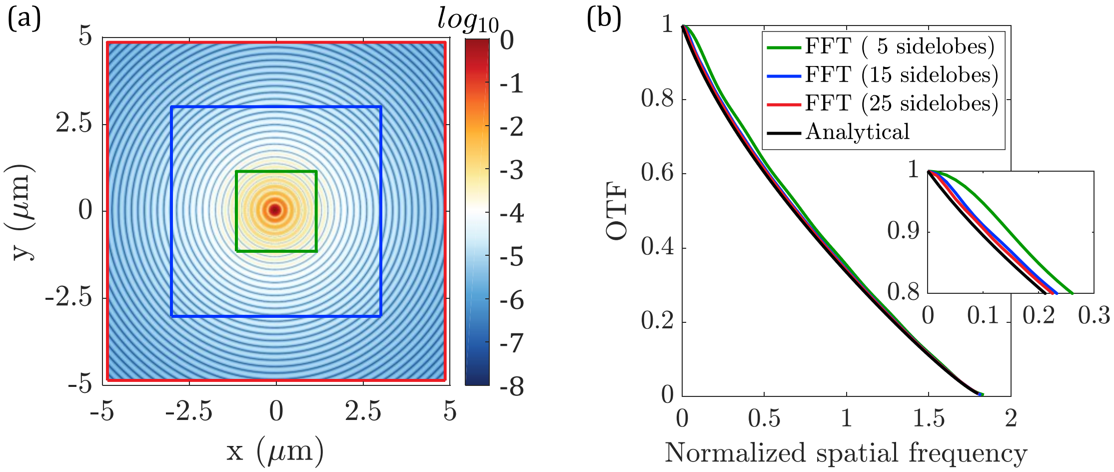

Figure 3.5: (a) Scalar Debye intensity PSF utilized to calculate a FFT-based OTF ($NA = 1.4$, $n = 1.52$, $\lambda_0 = 519$ nm, and $\alpha = 0°$). The green, blue, and red rectangles embrace 5, 15, and 25 sidelobes respectively. (b) Comparison between FFT-based and analytical scalar Debye OTFs in the spatial frequency normalized by n/λ_0. The PSF data with sufficient sidelobes is vital for accurate OTF calculations. The inset shows details at the low frequency regions.

After confirming the accuracy of 2D OTF from the FFT method, the vectorial OTF in oblique plane imaging was identically calculated. The Eq. (3.7) was first evaluated in MATLAB's parallel computing environment to acquire the vectorial PSF with 25-sidelobes along the x_α and y_α directions, followed by the FFT operation. The results are plotted in

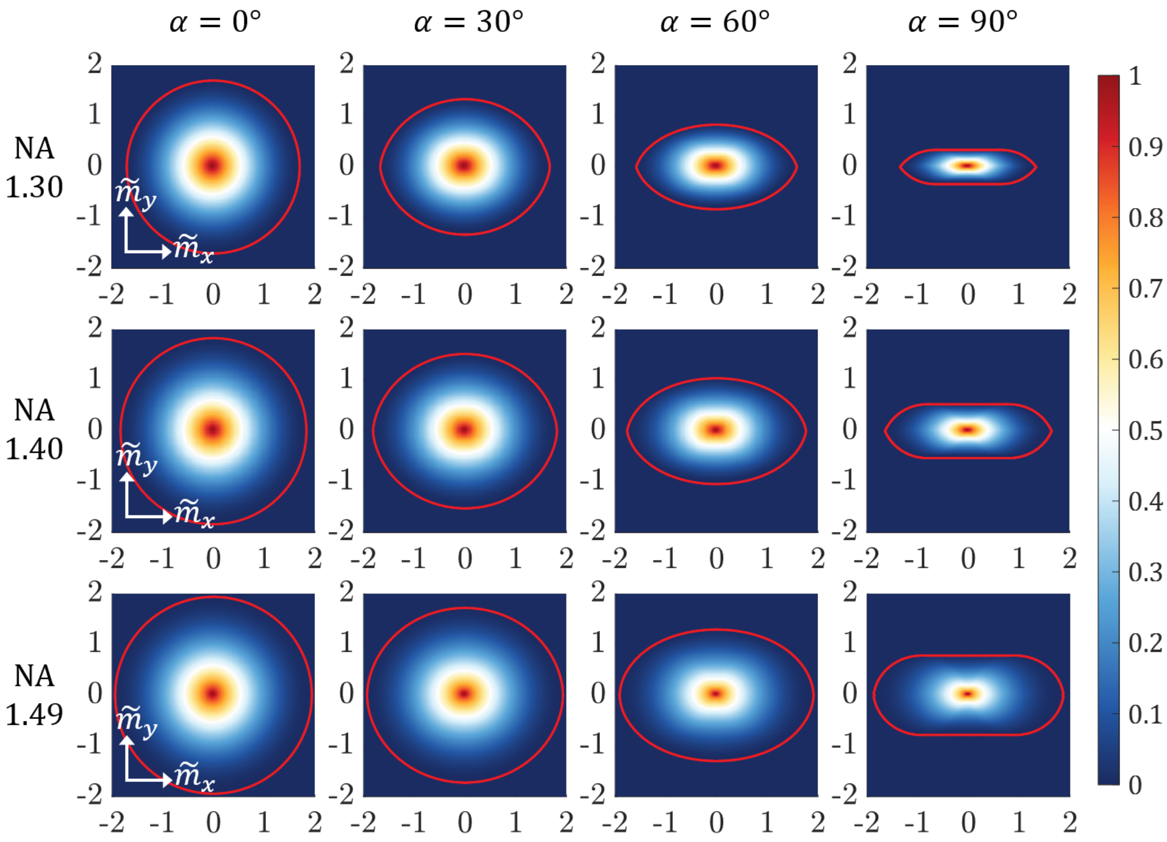

Figure 3.6: 2D vectorial OTF of oblique plane imaging over oblique angle (α) and NA ($\lambda_0 = 519$ nm, $n = 1.52$) at frequencies normalized by n/λ_0. Red contours are MTF cutoffs.

Fig. 3.6. The bandwidth (or cutoff frequency) along the $\tilde{m}_y$ direction (corresponding to the y_α-axis in real space) reduces much faster than along the $\tilde{m}_x$ direction at higher oblique angles, which is self-evident from the anisotropic PSF trend in Fig. 3.3. Cross-sections of these OTFs were compared in Fig. 3.7. The vectorial OTF has lower modulations over the whole frequency extent than the scalar Debye OTF (α=0°). This lower MTF results mainly from the depolarized field along the optical axis that broadens the vectorial PSF, which is ignored in the scalar theory. The cutoff frequency in the scalar Debye theory is $2NA/n$, *i.e.*, 1.71 (1.84, 1.96) at the NA of 1.30 (1.40, 1.49), corresponding to 5.0 (5.4, 5.7) cycles/μm in physical frequency. The numerical cutoff frequency of the vectorial OTF was determined at a threshold MTF of 0.01% to neglect minor MTF oscillations near and above the cutoff frequency (numerical artifacts). The estimated vectorial cutoff frequencies for $\alpha = 0°$ agreed with the analytical $2NA/n$ within 1% error.

The OTF cross-sections for α = 60, 90° in Fig. 3.7 clearly show a downward trend in both MTF curves and cutoff frequencies at higher oblique angle, which is plotted in Fig. 3.8. The $\tilde{m}_x$ cutoff is lowered by 21% (10%, 5%) at the NA of 1.30 (1.40, 1.49) as the oblique angle increases from 0° to 90°. Likewise, the cutoff frequency along the $\tilde{m}_y$ axis reduces up to 80% (71%, 60%). The degradation of the MTF cutoff is relatively smaller at higher NA.

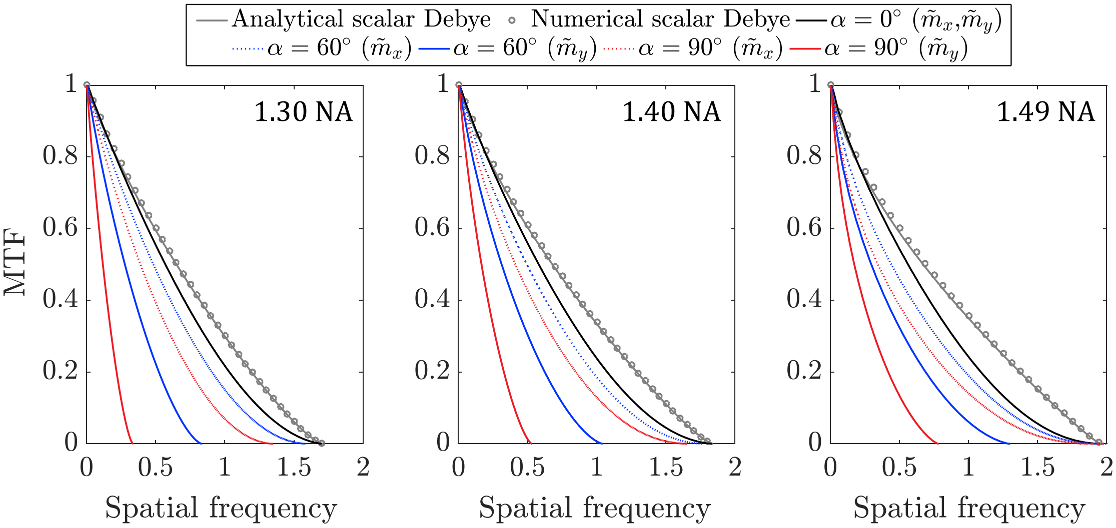

Figure 3.7: Vectorial OTF cross-sections along the $\tilde{m}_x$ and $\tilde{m}_y$ directions for $\alpha = 0$, 60, and 90°, at spatial frequencies normalized by n/λ_0 ($\lambda_0 = 519$ nm, $n = 1.52$). The scalar Debye OTF for $\alpha = 0°$ is added for comparison.

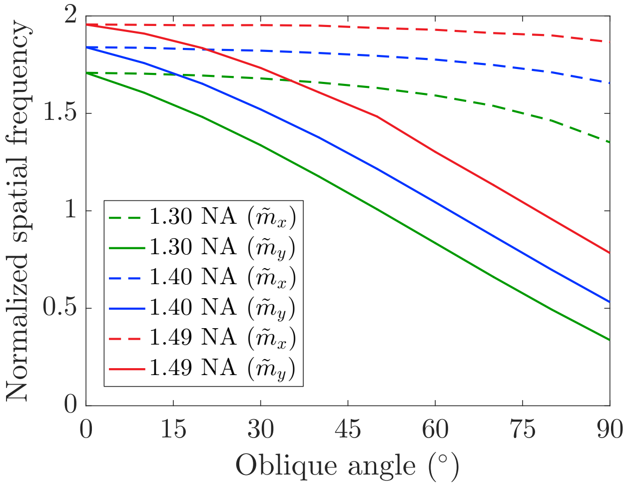

Figure 3.8: Spatial cutoff frequency of the vectorial OTF over oblique angles.

From the numerical results discussed so far, one could neglect the light clipping at the lower oblique angle regime. The simulation indicates a FWHM increase less than 10% along the mirror-tilt direction for an oblique angle up to 16° (20°, 27°) at the NA of 1.30 (1.40, 1.49) in oil medium with $\lambda_0 = 519$ nm. This conclusion is from the assumed uniform, unpolarized electric field incident on the exit pupil.

3.5 Axial depth of field in remote focusing

The remote focusing eliminates only the lowest-order primary aberrations, and thus the depth of field is limited. From the paraxial scalar theory with the residual aberration function considered, this depth range was analytically derived by inspecting the Strehl ratio (S) [126] as

$$S = 1 - \frac{4n_2^2k_0^2z_1^4(3+16\cos\alpha_2+\cos(2\alpha_2))\sin^8(\alpha_2/2)}{75f_2^2(3+8\cos\alpha_2+\cos(2\alpha_2))}, \tag{3.10}$$

where f and α_2 denote focal length and half-cone angle of the two identical objectives in the symmetric remote focusing geometry ($|M_R|=1$ in Fig. 3.9). Also, it was predicted that there occurs a high NA diffraction defocus (δz) from the higher-order residual aberration that breaks a constant transformation of $\vec{x}_2 = (n_1/n_2)\vec{x}_1$. Again in the symmetric remote focusing, this defocus is given as [126]

$$\delta z = \frac{12z_1^2\cos^2(\alpha_2/2)(3+6\cos\alpha_2+\cos(2\alpha 2))}{5f(3+8\cos\alpha_2+\cos 2\alpha_2)}. \tag{3.11}$$

This section more rigorously investigates the axial working depth in a general non-symmetric remote focusing using the advanced diffraction theory. The aberration function, or optical path difference, associated with a defocused point object ($\vec{x}_1$) being imaged to a remote image point ($\vec{x}_2$), valid in smaller displacements only, is expressed as

$$\begin{aligned} W(\vec{x}_1,\vec{x}_2) &= n_1\big(|\vec{f}_1-\vec{x}_1|-f_1\big)+n_2\big(|\vec{f}_2+\vec{x}_2|-f_2\big) \\ &= n_1\Big(\sqrt{f_1^2+x_1^2-2\vec{f}_1\cdot\vec{x}_1}-f_1\Big)+n_2\Big(\sqrt{f_2^2+x_2^2+2\vec{f}_2\cdot\vec{x}_2}-f_2\Big), \end{aligned} \tag{3.12}$$

which cancels out up to the first-order approximation of the root terms by the Taylor series expansion if $f_1 \gg |\vec{x}_1|$ and $f_2 \gg |\vec{x}_2|$. Then the residual higher-order aberrations left are

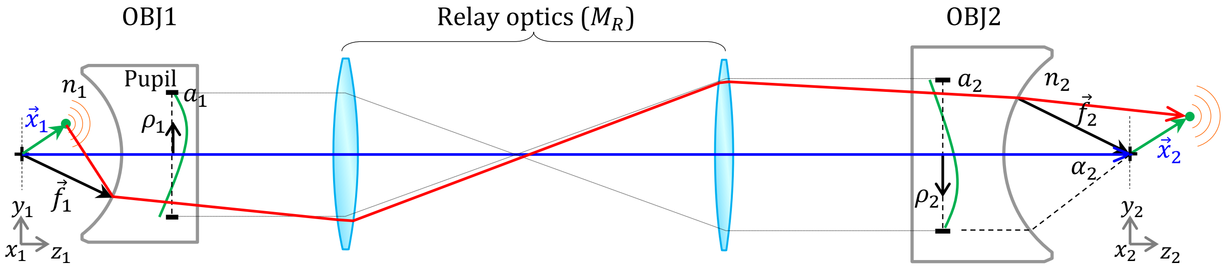

Figure 3.9: A remote focusing geometry for an extended depth of field. The pupils of the two objectives are matched by a relay optics of $|M_R| = n_2f_2/(n_1f_1)$ to satisfy $\vec{x}_2 = (n_1/n_2)\vec{x}_1$.

given, for on-axis objects for simplicity without losing generality, by

$$W(\rho_2,\phi_2;z_1,z_2)=\frac{\sin^2\alpha}{2}\Big(\frac{\rho_2}{a_2}\Big)^2\Big\{\frac{n_1z_1^2}{f_1}+\frac{n_2z_2^2}{f_2}+\Big[1-\frac{5}{4}\Big(\frac{\rho_2}{a_2}\Big)^2\sin^2\alpha\Big]\Big(\frac{n_1z_1^4}{f_1^3}+\frac{n_2z_2^4}{f_2^3}\Big)+\dots\Big\}, \tag{3.13}$$

where ρ denotes a radial pupil coordinate, a a pupil radius, $|\vec{f}|$ a focal length, n a medium refractive index, z a defocus from the focal plane, and $\alpha=\alpha_1=\alpha_2$ the half-cone angle. In the remote focusing condition, if $z_2=(n_1/n_2)z_1$, every z_2-related terms in the parenthesis are paired with the according z_1 terms, reducing to $W(\rho_2,\phi_2;z_1)$. The magnitude of the residual aberrations is dominantly proportional to $nf^{-1}z^2\sin^2\alpha$, aggravating aberrations to the squares of the defocus and the half-cone angle, and to the inverse of the focal length. This radially symmetric aberration function can be plugged into the scalar Debye integral to evaluate the Strehl ratio derived as

$$S\equiv\frac{I(z_2;z_1)\big|_{\max}}{I(0;0)\big|_{W=0}}=\frac{\big|\int_0^\alpha e^{ik_0(W(\theta,\phi;z_1)+n_2z_2\cos\theta)}\,\sin\theta\,d\theta\big|^2_{\max}}{\big|1-\cos\alpha\big|^2}, \tag{3.14}$$

where $\theta=\rho_2/(n_2f_2)=\rho_1/(n_1f_1)$. Here an isotropic point source is assumed to locate at z_1. The $\sqrt{\cos\theta}$ apodization of the two objectives are inversely related and thus removed.

On the other hand, strictly speaking, the vectorial approach is nontrivial here because the polarization ray tracing for defocused object points in high NA aplanatic objectives may be a new ray bending matrix. For smaller defocus displacements, however, the Eq. (2.60) may still be approximately used with $\sqrt{\cos\theta}$ deleted for the same reason. Since the axial response keeps unchanged for any input polarization state as studied in Section 2.7, the vectorial Strehl ratio, if the aberrations are considered, may be derived as

$$S\equiv\frac{I(z_2;z_1)\big|_{\max}}{I(0;0)\big|_{W=0}}=\frac{\big|\int_0^\alpha(1+\cos\theta)e^{ik_0(W(\theta,\phi;z_1)+n_2z_2\cos\theta)}\,\sin\theta\,d\theta\big|^2_{\max}}{\big|5/4-\cos\alpha-1/4\cos(2\alpha)\big|^2}. \tag{3.15}$$

Numerical simulation was conducted for the derived equations in Fig. 3.10. The scalar Debye and the vectorial Debye theory yield almost identical axial responses. The peak intensity at each object defocus, z_1, indicates the Strehl ratio and its shifted position is an amount of the diffraction defocus. As expected, as the object defocus increases, the Strehl ratio drops and the diffraction defocus occurs towards the positive z_2 direction (farther away from the remote objective lens). As shown in Fig. 3.11, the scalar and the vectorial Debye theories predict less severe drops in the Strehl ratio at $|z_1|>40\,\mu m$. The range of axial field depth, based on the conventional diffraction-limited cutoff at $S=0.81$, is around 80 μm in all cases. The diffraction defocus predicted is almost the same among the three theories, while the vectorial Debye defocus resides between the paraxial defocus and the scalar Debye defocus.

Similar arguments could be made for off-axis object points, which may further limit the lateral and axial working range.

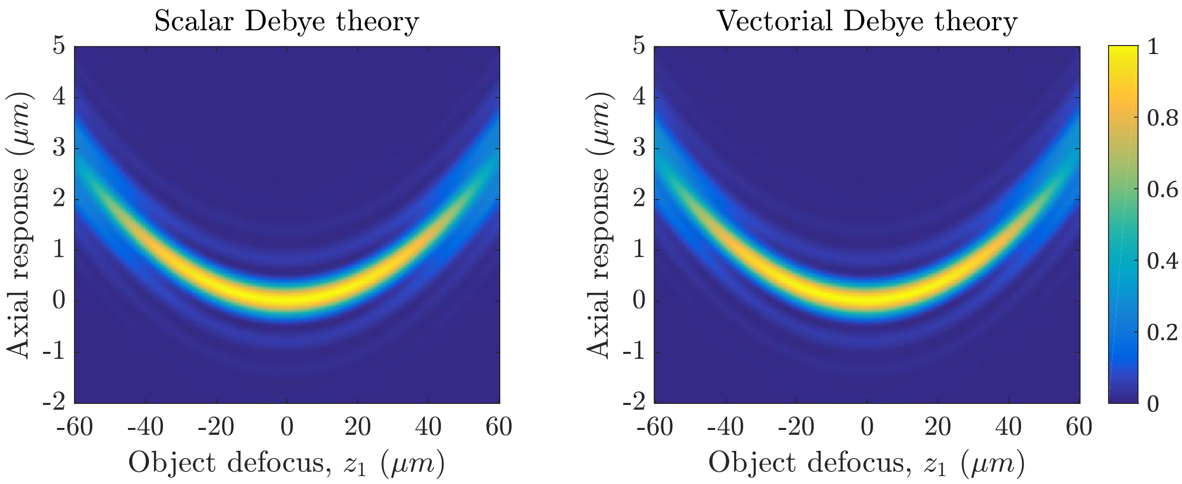

Figure 3.10: Axial responses in the remote focusing from (left) scalar Debye theory (right) vectorial Debye theory. Objective NA: 1.4 ($f = 1.8$ mm), $n = 1.52$, $\lambda_0 = 519$ nm.

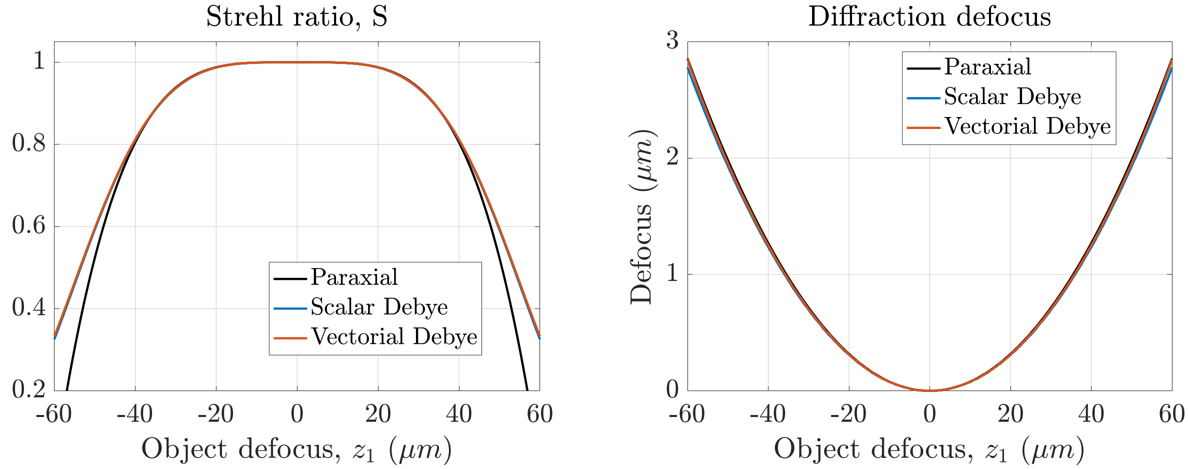

Figure 3.11: Strehl ratio and diffraction defocus in the remote focusing with different diffraction theories. Objective NA: 1.4 ($f = 1.8$ mm), $n = 1.52$, $\lambda_0 = 519$ nm.

3.6 Experimental demonstration

After the theoretical study of oblique plane imaging, an experimental demonstration of the method was performed. Here an optical setup for an oblique angle of 90°, termed axial plane microscopy (APM), was built. The two apochromatic objective lenses (1.4 NA, oil immersion, 100x, Carl Zeiss) with all other lenses with $f = 150$ mm were chosen. Two imaging modes were considered. First, a conventional lateral imaging (XY plane) was achieved by putting a tube lens above the BS2 (50:50 unpolarized beam splitter) in Fig. 3.1 together with a white light illumination via the BS1. Second, an axial plane imaging (XZ) was implemented by

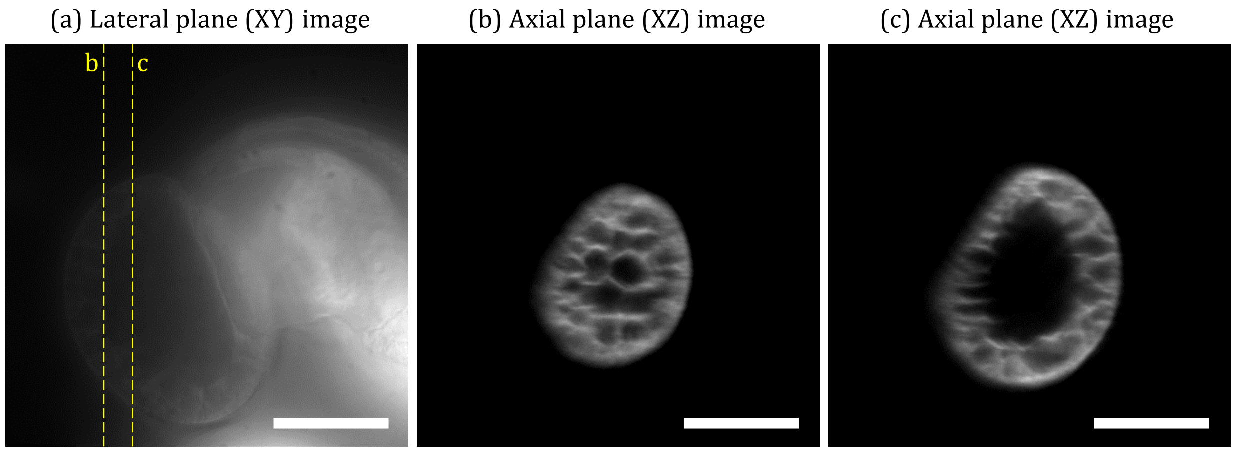

Figure 3.12: Autofluorescence imaging of a pine pollen grain in axial plane microscopy. (a) conventional lateral plane (XY) imaging with a wide-field illumination. (b, c) axial plane (XZ) imaging at the section b and c respectively with an axial lightsheet illumination. The scale bar is 20 μm.

putting the 45° mirror (made with a piece of a cleaved Si wafer with Al deposition on it) at the remote space. In this mode, a pair of cylindrical lens with a laser beam was employed to provide an axial lightsheet illumination [128] along the axial plane. The lightsheet was around 2 μm in thickness at focus.

It was experimentally proved in [129] that APM has around one-micron resolution along the axial direction over a 70 μm depth. One imaging example is shown in Fig. 3.12. It is clear that the axial image with the lightsheet illumination (enabling optical sectioning) provides a higher contrast and thus an improved signal-to-background noise ratio than the lateral image with the conventional wide-field illumination.

The APM demonstrated here is an innovative imaging tool that works in real-time to image any plane of a 3D sample without beam scanning. If combined with conventional microscopy, APM simultaneously provides two orthogonal plane images of a 3D sample. Using the light-sheet illumination, it enables fast, high-contrast, and convenient 3D imaging of structures that are hundreds of microns beneath the surfaces of large biological tissues. The potential application may include 1) high speed *in vivo* 3D diagnosis of early stage tissue-related diseases such as noninvasive detection of skin caner, 2) live cell/tissue study [130] such as neuronal activity [131], quantitative monitoring of blood flow in vascular tubes, and 3) flow cytometry with at least one order improved throughput.

Chapter 4

Super-Resolution Oblique Plane Microscopy

The existing far-field super-resolution technique (such as STORM, PALM, and FPALM), here called STORM from now on for convenience, has been successful to boost new biological study in nano-scale [132–134]. A typical STORM setup is somewhat similar to total internal reflection fluorescence (TIRF) microscopy. The TIR illumination via high NA objective lens is good to minimize background fluorescence noises by confining the evanescent illumination fields only near the glass-to-sample boundary over a depth of around a couple of 100 nm. This illumination method works well with STORM where a fluorescence signal from each single molecule is extremely weak, but also limits an available imaging depth only to the sample's surface. By adjusting an illumination angle just below the critical angle (where the TIR begins to occur), a penetration depth can be increased by a few microns from the surface. Yet this may not be sufficient at whole cell or tissue-level study. In addition, the TIR based illumination inherently requires an index-mismatch between the coverslip and sample media, which thus induces detrimental optical aberrations. This could be compensated by adaptive optics (AO) [135] with a complicated optical setup, but accessing a few microns depth from the sample's surface is still nontrivial.

In order for STORM to achieve super-resolution deep imaging, oblique plane super-resolution microscopy, termed *oblique*STORM, is proposed. *oblique*STORM combines wide-field oblique plane microscopy (in Chapter 3) with conventional STORM. Oblique lightsheet illumination is employed to minimize background fluorescence noise, which is free from the index-mismatch requirement present in TIRF microscopy. Thus by using objectives (such as water-, silicon-, or glycerol-immersion) that are best matched with the sample index, penetration depth can be easily extended to tens of microns without adaptive optics.

This chapter covers an analytical study of *oblique*STORM. The PSF in oblique plane fluorescence microscopy is first formulated by the vectorial diffraction theory, to figure out the best way to configure the optical setup. Then, the achievable super-resolution with the proposed method is estimated over all possible oblique angles. Also, axial working depth associated with tilted remote focusing in fluorescence microscopy is studied. Furthermore, an experimental setup to demonstrate the proposed method is introduced with several factors to consider in building the setup for the best performance. Several experimental results that support the theoretical prediction are included. Preliminary test results associated with super-resolution imaging are summarized, followed by listing future work.

4.1 Schematic of *oblique*STORM

The proposed schematic of *oblique*STORM is illustrated in Fig. 4.1. As for illumination, a single laser could be enough for direct STORM (dSTORM [136]), but here multiple lasers could be employed for multi-color excitations and/or for an efficient activation. As an example, the commonly used wavelengths are written on the laser heads. A weak activation laser could be at UV (ultraviolet) or near 405 nm light. Further laser heads could be also added in parallel upon a preference on selections of fluorescent dyes. Each laser may have a variable neutral density filter to properly tune optical power and a beam expander to match the beam sizes as required upon the illumination design. After coupled into a single circular Gaussian beam by a dichroic beam splitter in free space, they may be shrunken as a slit beam by a pair of cylindrical lenses. This slit beam is demagnified by the L1-OBJ1 optics to the sample space with an oblique angle steered by the oblique angle adjuster mirror. This is how the oblique lightsheet illumination is implemented. The beam expanders mentioned could be used as compensators for chromatic aberrations among laser lines if exist, to make

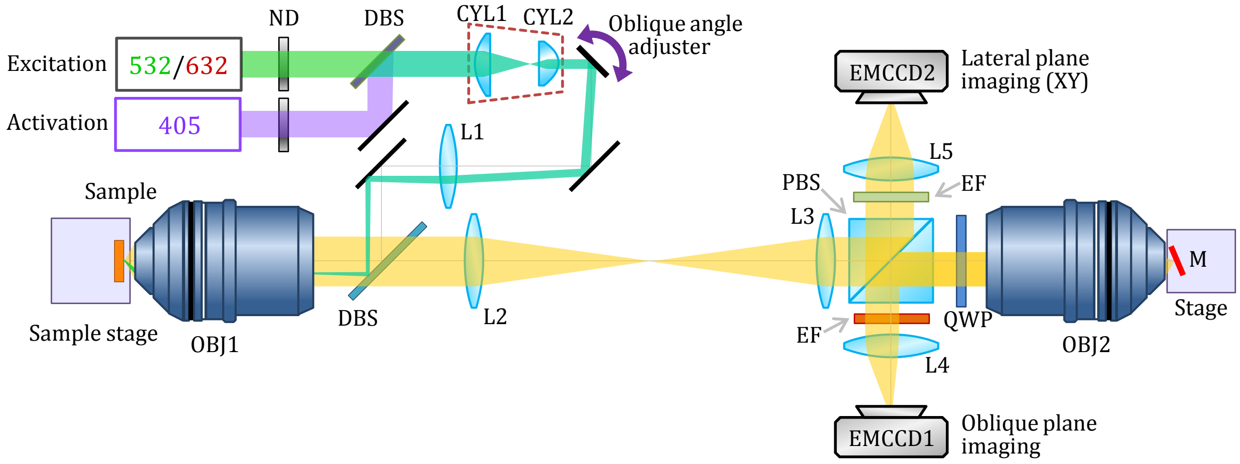

Figure 4.1: Schematic of *oblique*STORM (top view). ND: neutral density attenuator, DBS: dichroic beam splitter, CYL: cylindrical lens, L: lens, OBJ: objective lens, PBS: polarizing beam splitter, QWP: quarter wave plate, M: mirror, EF: emission filter, EMCCD: electron multiplying charge coupled device. An oblique lightsheet illumination to a sample is provided by steering a field angle of a slit beam formed by a pair of cylindrical lenses. The STORM signals on the oblique plane are recorded by EMCCD1 through the oblique mirror M.

sure that all the lightsheets for each color are formed at the same object depth. The OBJ1 and OBJ2 are remotely connected by the L2-L3 relay optics with a total magnification of n_1/n_2 (refractive index ratio). A remote mirror rotates the intermediate image of the 3D object such that an oblique plane image (Oblique mode) is formed at the EMCCD1 camera via the L4 tube lens. The PBS and the QWP were used to minimize signal loss compared with when a non-polarizing BS is used. The other half of the signal coming out from PBS is used for conventional lateral plane imaging (XY mode) via the L5 tube lens. The image at the EMCCD2 could be used for many purposes. It may allow simultaneous super-resolution imaging at both the oblique and lateral planes. It can be also used to compensate image drifts during the STORM data acquisition. The DBS and emission filters (EF) could be multi-bands to accommodate various fluorophores across the visible spectrum. To easily switch the lightsheet illumination to wide-field epi-illumination and vice versa, the pair of cylinder lenses could be mounted on a magnetic base to easily take them out without impairing the alignment. In that case, a Gaussian-to-TopHat beam shaper could be optionally placed on the magnetic base to provide a uniform square illumination for conventional wide-field fluorescence microscopy. It is recommended to mount the sample and the remote mirror on precision stages with a motion control capability, to correct any undesirable motion drifts in real-time while recording STORM data.

4.2 PSF formulation in XY imaging mode

The XY imaging mode can be simplified for PSF calculation as shown in Fig. 4.2. Only the s-polarized (or vertically polarized) field from the PBS contributes to the XY mode, and thus a linear polarizer at 90° (vertical) is put equivalently in the model. The total lateral magnification is determined by $M_{\mathrm{XY}} = (f_2/f_{\mathrm{OBJ1}})\cdot(f_5/f_3)$ where f_j is a focal length of the j^{th} lens. The numerical aperture of the OBJ1 is denoted as $NA_1 = n_1 \sin\alpha_1$.

The fluorescence emission from a fluorophore molecule could be modeled as an electric dipole radiation with an emission dipole moment of $\vec{p}$. Its strength partly depends on the angle between the absorption dipole moment and the field vector of illumination. Typically dye molecules in fluorescence microscopy are in solution, where they rapidly reorient by a

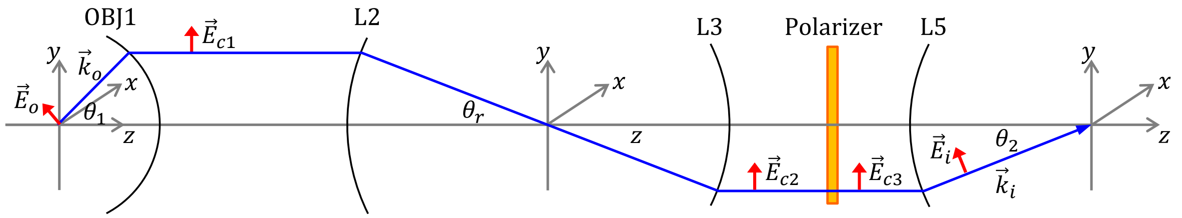

Figure 4.2: A simplified model of XY imaging mode in *oblique*STORM. All the lenses are assumed to be aplanatic. The PBS is replaced by a polarizer. The object and image cone angles are related by $n_1 \sin\theta_1 = M_{\mathrm{XY}} n_2 \sin\theta_2$ with $n_2 = 1$ (in air).

rotational diffusion. In this case the dipole moment $\vec{p}$ is assumed free to rotate in calculating PSF. If fluorophores are fixed, a certain orientation of $\vec{p}$ needs to be considered. For *oblique*STORM the former situation can be used. The electric dipole field is analytically expressed [86] as

$$\vec{E} = \frac{1}{4\pi\epsilon_0}\Big\{k^2(\vec{n}\times\vec{p})\times\vec{n}\frac{e^{ikr}}{r} + [3\vec{n}(\vec{n}\cdot\vec{p}) - \vec{p}]\Big(\frac{1}{r^3} - \frac{ik}{r^2}\Big)e^{ikr}\Big\}, \tag{4.1}$$

where $\vec{n}$ denotes the unit vector from the dipole center to a observation point. Since far-field radiations are of interest, the radiation field from an on-axis fluorophore could be approximated as

$$\vec{E}_o = -\vec{k}_o \times (\vec{k}_o \times \vec{p}), \tag{4.2}$$

where $\vec{k}_o = [\sin\theta_1\cos\phi_1, \sin\theta_1\cos\phi_1, \cos\theta_1]$ is a unit propagation vector in the object spherical coordinate (r_1, θ_1, ϕ_1). Here, assuming the field is a narrowband ($\bar{\lambda} \gg \Delta\lambda$), the prefactor associated with the wavelength is neglected. This would be justified as a typical fluorescence emission band after an emission filter is only several tens of nm.

From the polarization ray tracing introduced in Section 2.6, the field right before the polarizer in Fig. 4.2 is calculated as

$$\begin{aligned}\vec{E}_{c2} =& \sqrt{\frac{1}{\cos\theta_1}}\mathbb{R}^{-1}(\pi+\phi_1)\mathbb{L}(\theta_r)\mathbb{R}(\pi+\phi_1)\mathbb{R}^{-1}(\phi_1)\mathbb{L}(\theta_r)\mathbb{L}(\theta_1)\mathbb{R}(\phi_1)\vec{E}_o \\ =& \sqrt{\frac{1}{\cos\theta_1}}\begin{bmatrix} \cos\theta_1\cos^2\phi_1+\sin^2\phi_1 & -(1-\cos\theta_1)\cos\phi_1\sin\phi_1 & -\sin\theta_1\cos\phi_1 \\ -(1-\cos\theta_1)\cos\phi_1\sin\phi_1 & \cos\theta_1\sin^2\phi_1+\cos^2\phi_1 & -\sin\theta_1\sin\phi_1 \\ 0 & 0 & 0 \end{bmatrix}\vec{p},\end{aligned} \tag{4.3}$$

which is a transverse field equal to $\vec{E}_{c1}$. After passing the vertical polarizer (only the y-component of $\vec{E}_{c2}$ survives), the final field strength at the exit pupil right after the L5 lens is given by

$$\begin{aligned}\vec{E}_i =& \sqrt{\cos\theta_2}\mathbb{R}^{-1}(\pi+\phi_1)\mathbb{L}(\theta_2)\mathbb{R}(\pi+\phi_1)\mathbb{P}(90^\circ)\vec{E}_{c2} \\ =& \sqrt{\frac{\cos\theta_2}{\cos\theta_1}}\begin{bmatrix} (1-\cos\theta_1)(1-\cos\theta_2)\cos^2\phi_1\sin^2\phi_1 & -(1-\cos\theta_2)\cos\phi_1\sin\phi_1(\cos\theta_1\sin^2\phi_1+\cos^2\phi_1) & (1-\cos\theta_2)\sin\theta_1\cos\phi_1\sin^2\phi_1 \\ -(1-\cos\theta_1)\cos\phi_1\sin\phi_1(\cos\theta_2\sin^2\phi_1+\cos^2\phi_1) & (\cos\theta_1\sin^2\phi_1+\cos^2\phi_1)(\cos\theta_2\sin^2\phi_1+\cos^2\phi_1) & -\sin\theta_1\sin\phi_1(\cos\theta_2\sin^2\phi_1+\cos^2\phi_1) \\ (1-\cos\theta_1)\sin\theta_2\cos\phi_1\sin^2\phi_1 & -\sin\theta_2\sin\phi_1(\cos\theta_1\sin^2\phi_1+\cos^2\phi_1) & \sin\theta_1\sin\theta_2\sin^2\phi_1 \end{bmatrix}\vec{p},\end{aligned} \tag{4.4}$$

where θ_2 denotes the polar angle at the image space. The medium index of the object space is neglected in the apodization factor. One can also check that the same series of the tracing matrices yield the final wave vector $\vec{k}_i = [\sin\theta_2\cos\phi_1; \sin\theta_2\sin\phi_1; \cos\theta_2]$ as expected. A converging wave feature at the exit pupil by the L5 lens can be reflected by multiplying $\frac{e^{-ikf_5}}{f_5}$ to $\vec{E}_i$. The PSF is calculated by plugging this field strength to the vectorial Debye integral Eq. (2.6) with $\hat{N} = [\sin\theta\cos\phi_1; \sin\theta\sin\phi_1; \cos\theta]$ where $\theta = \pi - \theta_2$. The pupil for the

XY mode is circular and thus the amplitude PSF in the cylindrical image coordinate (ρ, ϕ, z) can be derived as

$$\vec{E} = \frac{1}{i\bar{\lambda}}\frac{\pi}{4}\begin{bmatrix} A_0^2 - A_4^1\cos(4\phi) & A_2^3\sin(2\phi) - A_4^1\sin(4\phi) & iA_1^2\cos\phi + iA_3^1\cos(3\phi) \\ A_2^2\sin(2\phi) - A_4^1\sin(4\phi) & A_0^1 - A_2^1\cos(2\phi) + A_4^1\cos(4\phi) & -iA_1^1\sin\phi + iA_3^1\sin(3\phi) \\ iA_1^4\cos\phi + iA_3^2\cos(3\phi) & -iA_1^3\sin\phi + iA_3^2\sin(3\phi) & A_0^3 + A_2^4\cos(2\phi) \end{bmatrix}\vec{p}, \tag{4.5}$$

where

$$A_p^q = \int_0^{\alpha_2}\sqrt{\frac{\cos\theta_2}{\cos\theta_1}}\,F_p^q(\theta_1,\theta_2)\,J_p(k\rho\sin\theta_2)\,e^{i\bar{k}z\cos\theta_2}\sin\theta_2\,d\theta_2, \tag{4.6}$$

where $\alpha_2 = \sin^{-1}\left(\frac{NA_1}{M_{\mathrm{XY}}}\right)$ with

$$\begin{aligned}
F_0^1(\theta_1,\theta_2) &= (3+\cos\theta_1+\cos\theta_2+3\cos\theta_1\cos\theta_2), & F_0^2(\theta_1,\theta_2) &= (1-\cos\theta_1)(1-\cos\theta_2),\\
F_0^3(\theta_1,\theta_2) &= 4\sin\theta_1\sin\theta_2, & F_1^1(\theta_1,\theta_2) &= 2\sin\theta_1(1+3\cos\theta_2),\\
F_1^2(\theta_1,\theta_2) &= 2\sin\theta_1(1-\cos\theta_2), & F_1^3(\theta_1,\theta_2) &= 2(1+3\cos\theta_1)\sin\theta_2,\\
F_1^4(\theta_1,\theta_2) &= 2(1-\cos\theta_1)\sin\theta_2, & F_2^1(\theta_1,\theta_2) &= 4(1-\cos\theta_1\cos\theta_2),\\
F_2^2(\theta_1,\theta_2) &= 2(1-\cos\theta_1)(1+\cos\theta_2), & F_2^3(\theta_1,\theta_2) &= 2(1+\cos\theta_1)(1-\cos\theta_2),\\
F_2^4(\theta_1,\theta_2) &= 4\sin\theta_1\sin\theta_2, & F_3^1(\theta_1,\theta_2) &= 2\sin\theta_1(1-\cos\theta_2),\\
F_3^2(\theta_1,\theta_2) &= 2(1-\cos\theta_1)\sin\theta_2, & F_4^1(\theta_1,\theta_2) &= (1-\cos\theta_1)(1-\cos\theta_2).
\end{aligned}$$

The averaged intensity PSF for a fluorophore in solution (free to rotate) is then calculated from Eq. (4.5) by

$$I = \sum_{x,y,z}\oiint \vec{E}\cdot\vec{E}^*\sin\theta_p d\theta_p d\phi_p = \frac{4\pi}{3}\sum_{u=1,v=1}^{3,3}|E_{uv}|^2, \tag{4.7}$$

where $\vec{p} = \sin\theta_p\cos\phi_p\hat{x} + \sin\theta_p\sin\phi_p\hat{y} + \cos\theta_p\hat{z}$ (non-zero contributions result only from $\iint p_j^2\sin\theta_p d\theta_p d\phi_p = 4\pi/3$ where $j = x, y, z$), E_{uv} is each component of $\vec{E}$ in Eq. (4.5). This is an incoherent summation of all possible dipole orientations over the 4π solid angle.

Experimental verification

The derived PSF was first numerically calculated at the following parameter setting: $\bar{\lambda} = 683$ nm, objective lens: Olympus 100x, 1.4 NA (oil index: 1.512), tube lens focal length: 150 mm. As shown in Fig. 4.3, the x- and z-component of the intensity PSF are negligible compared to the y-component (primary polarization), mainly due to insignificant depolarizations at the low NA tube lens. The vertically elongated PSF results from a rotationally asymmetric pupil distribution by the $\mathbb{P}(90°)$ polarizer that selectively chooses the dipole field only for the vertical and near-vertical dipole orientations whose angular emission across x-axis is uniform and the strongest (while angularly decays along the y-axis as $\cos^2\theta$). This reason is different from the depolarization during the light focusing that results in an anisotropic

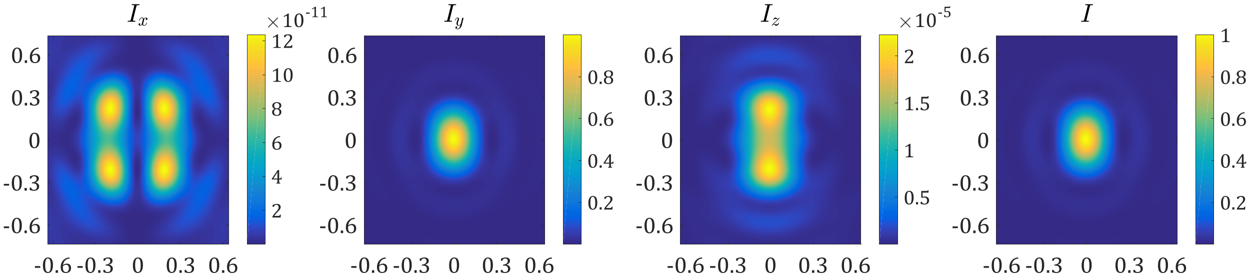

Figure 4.3: Theoretical intensity PSF (each component and overall) in XY imaging mode ($NA_1 = 1.4$, $\bar{\lambda} = 683$ nm). The axis unit is μm. Due to the negligible depolarization at the low NA tube lens, the PSF is governed by the pupil distribution of the E_y field. The vertically elongated PSF is predicted. FWHMx: 235.6 nm, FWHMy: 330.5 nm.

PSF in Section 2.7. In that case, by putting a QWP or HWP (half wave plate) right before the focusing lens, the PSF could be manipulated to be isotropic if desired. However, here it is not the depolarization but the pupil distribution itself that determines the shape of PSF. Placing such wave-plates still keeps the field distribution at the exit pupil unchanged, thus yielding the same anisotropic PSF. If a horizontal polarizer is used in Fig. 4.2, the intensity PSF should be the same but rotated by 90° (due to the geometrical symmetry).

An experimental PSF was measured using 46-nm-diameter dark red fluorescent beads (F8789, Molecular Probes™) at a peak emission at 683 nm. A drop of 20 μL of a 10^5x diluted bead solution in deionized water was dried on an oxygen plasma-etched coverslip. Then the coverslip was put on a microscope slide glass with 10 μL antifade mounting medium (Vectashield, H-1000, Vector Laboratories) and shielded by a nail polish. An optical setup was built with the Olympus UPLSAPO objective (100XO, 1.4 NA), the L2-L3 relay optics ($f = 200$ mm, AC254-200-A-ML, Thorlabs), the L5 tube lens ($f = 150$ mm, AC254-150-A-ML, Thorlabs), and a visible PBS (CM1-PBS251, Thorlabs). The prepared sample was excited by a 641 nm laser (OBIS 640LX-40, Coherent) via a quanband dichroic beam splitter (Di03-R405/488/532/635-t1-25x36, Semrock), and fluorescent signals were filtered by a quad-band emission filter over 659-748 nm (FF01-446/510/581/703-25, Semrock). The XY image was captured by a sCMOS camera (pixel: 3.75 μm, CM3-U3-13S2M-CS, Point Grey) and analyzed in Fig. 4.4.

The experimental PSF well agrees with the theoretical prediction with FWHM errors of 6.0% (x) and 1.3% (y), respectively. The PSF was also measured for reference right after the L2 lens in Fig. 4.1 where unpolarized fluorescence signals form a circular PSF. The average FWHM measured there was 291 nm, which is 5.0% larger than the theoretical FWHM. It appears that there are no noticeable size effects of the beads (20% the $\mathrm{FWHM_x}$ in size) on PSF measurement here. From this experiment, it turned out that the vectorial analysis is a precise method on estimating a PSF of high NA imaging systems. On the other hand, the paraxial scalar theory, leading to an isotropic FWHM of 251.7 nm, does not predict such an anisotropic behavior on PSF.

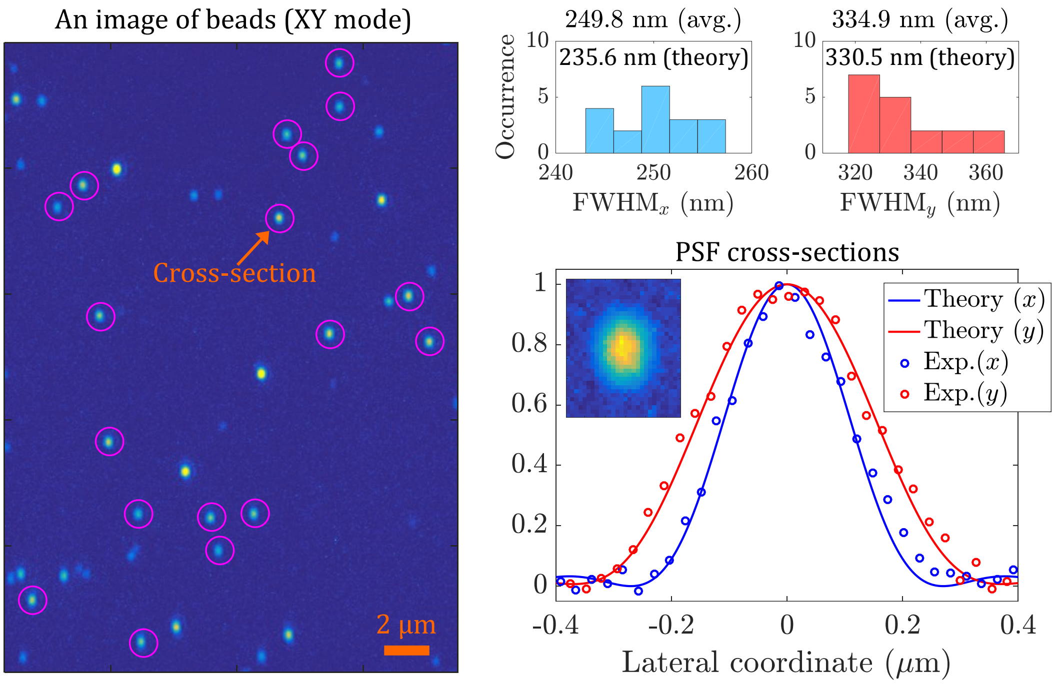

Figure 4.4: Measurement of PSF using 46 nm fluorescent beads (1.4 NA at $\bar{\lambda} = 683$ nm). The average FWHMs for 18 beads (pink circles) from Gaussian fittings are 249.8 nm (x) and 334.9 nm (y), which are larger than the theoretical FWHMs by 6.0% and 1.3%, respectively.

4.3 PSF formulation in oblique imaging mode

Now that an effectiveness of the vectorial diffraction theory was experimentally confirmed in previous section, the same methodology could be applied to the oblique imaging mode simplified as shown in Fig. 4.5 . The PBS this time is replaced by two linear polarizers: horizontal for forward propagation and vertical for backward propagation. There is an oblique remote mirror at the OBJ2 space that reflects the beam back to the OBJ2 (dashed blue ray).

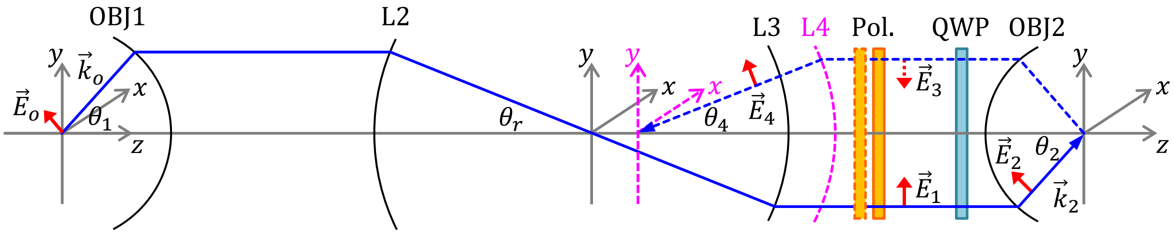

Figure 4.5: A simplified model of oblique imaging mode in *oblique*STORM. All the lenses are assumed to be aplanatic. The PBS is replaced by two polarizers (one for forward path, the other for backward path).

The reflected beam travels backwardly through the L4 tube lens and forms an oblique image at the dashed pink xy-coordinate. The polar angle between the remote space and the imaging space (in air) is related by $n_2 \sin\theta_2 = M \sin\theta_4$, where $M = (f_4/f_{\mathrm{OBJ2}}) = (n_2 \sin\alpha_2)/\sin\alpha_4$ is the lateral magnification of the detection microscope (the OBJ2-L4 optics). The total lateral magnification from the sample to the final image is determined by $M_{\mathrm{O}} = (n_1/n_2)M$.

Effective pupil function

The effective pupil function in oblique imaging mode is not rotationally symmetric about the optical axis. In Chapter 3, the pupil function was derived when the object NA and the remote NA were identical. Here the similar process is applied to derive an effective pupil function when the remote NA (NA_2) is larger than the objective NA (NA_1), since a higher remote NA is preferred to maximize the transmission efficiency, thus enhancing a localization precision of the STORM.

From Fig. 4.6, the effective pupil in oblique imaging mode would be an areal overlap between the NA_2 spherical cap (dark blue) and the reflected NA_1 cap (light blue) by the remote mirror tilted by $\alpha/2$. As illustrated, there is an additional pupil area by choosing a higher remote numerical aperture. The line $\overline{AC}$ equation is given by $z + x\tan\alpha + \sec\alpha\sqrt{1-(NA_1/n_1)^2} = 0$ from its slope of $\tan\alpha$ and the coordinate of the point A, *i.e.*, $(x_A,\ z_A) = (-\tan(\alpha/2)\sqrt{1-(NA_1/n_1)^2}, -\sqrt{1-(NA_1/n_1)^2})$. Plugging this into a unit circle equation ($x^2 + z^2 = 1$) provides the coordinate of point C as

$$(x_C, z_C) = \left(\frac{NA_1}{n_1}\cos\alpha - \sin\alpha\sqrt{1-\left(\frac{NA_1}{n_1}\right)^2}, -\frac{NA_1}{n_1}\sin\alpha - \cos\alpha\sqrt{1-\left(\frac{NA_1}{n_1}\right)^2}\right). \tag{4.8}$$

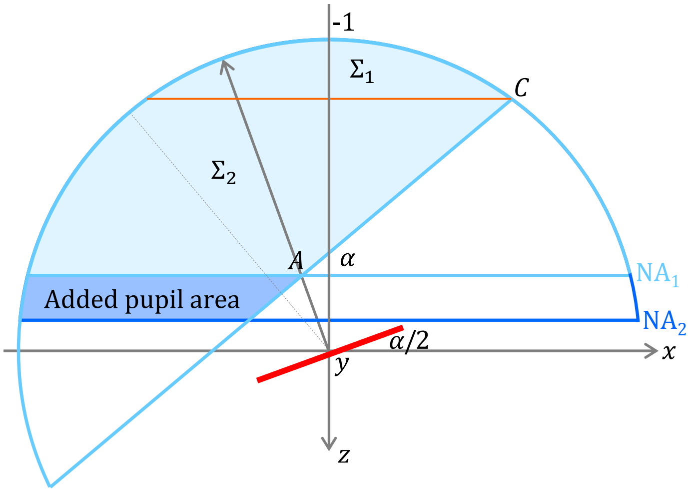

Figure 4.6: Effective pupil function in oblique imaging mode in the normalized remote space. A higher remote NA ($NA_2 > NA_1$) enlarges the effective pupil area determined by an overlap of the reflected NA_1 spherical cap by the tilted remote mirror with the NA_2 spherical cap.

Then the separated pupil functions, for mathematical convenience, are defined as

$$\begin{aligned}
P_{\Sigma_1}(\theta_2,\phi_2) &= \begin{cases} 1, & \theta_2 \in [0,\theta_C],\ \phi_2 \in [0,2\pi], \text{ and } x_C > 0 \\ 0, & \text{otherwise} \end{cases}, \\
P_{\Sigma_2}(\theta_2,\phi_2) &= \begin{cases} 1, & \theta_2 \in [\theta_C,\theta_{\max}] \text{ and } \phi_2 \in [\phi_{2,\min}(\theta_2),\phi_{2,\max}(\theta_2)], \text{ and } x_C < 0 \\ 0, & \text{otherwise} \end{cases},
\end{aligned} \tag{4.9}$$

where Σ_1 is a rotationally symmetric part, Σ_2 is an asymmetric part, and (θ_2,ϕ_2) is the normalized spherical remote coordinate. At a higher oblique angle where $x_C < 0$, the symmetric Σ_1 no longer exists and only $P_{\Sigma_2}(\theta_2,\phi_2)$ remains. The pupil boundaries are derived, using $(x,y,z) \equiv (\sin\theta\cos\phi, \sin\theta\sin\phi, -\cos\theta)$, as

$$\begin{aligned}
\theta_C &= \cos^{-1}|z_C| = \cos^{-1}\left|\frac{NA_1}{n_1}\sin\alpha + \sqrt{1-\left(\frac{NA_1}{n_1}\right)^2}\cos\alpha\right|, \\
\theta_{\max} &= \sin^{-1}\left(\frac{NA_2}{n_2}\right), \\
\phi_{2,\min}(\theta_2) &= \cos^{-1}\left(\frac{y}{\sin\theta_2}\right) = \cos^{-1}\left|\cot\alpha\cot\theta_2 - \sqrt{1-\left(\frac{NA_1}{n_1}\right)^2}\csc\alpha\csc\theta_2\right|, \\
\phi_{2,\max}(\theta_2) &= 2\pi - \phi_{2,\min}(\theta_2).
\end{aligned} \tag{4.10}$$

Since a vectorial PSF calculation requires a pupil function at the exit pupil, the bounds obtained above could be converted to those based on the exit pupil spherical coordinate by $(\theta_4,\phi_4) = (\sin^{-1}(n_2/M\sin\theta_2),\phi_2)$, leading to

$$\begin{aligned}
\theta_{4,C} &= \sin^{-1}\left[\frac{n_2}{M}\sin\left(\cos^{-1}\left|\frac{NA_1}{n_1}\sin\alpha + \sqrt{1-\left(\frac{NA_1}{n_1}\right)^2}\cos\alpha\right|\right)\right], \\
\theta_{4,\max} &= \sin^{-1}\left(\frac{NA_2}{M}\right), \\
\phi_{4,\min}(\theta_4) &= \cos^{-1}\left|\cot\alpha\cot\left(\sin^{-1}\left(\tfrac{M}{n_2}\sin\theta_4\right)\right) - \sqrt{1-\left(\tfrac{NA_1}{n_1}\right)^2}\csc\alpha\csc\left(\sin^{-1}\left(\tfrac{M}{n_2}\sin\theta_4\right)\right)\right|, \\
\phi_{4,\max}(\theta_4) &= 2\pi - \phi_{4,\min}(\theta_4).
\end{aligned} \tag{4.11}$$

PSF formulation

The polarization ray tracing at the oblique mirror would be challenging, for it involves a new coordinate rotation to correctly decompose the field incident on the mirror into *p*- and *s*-components. The $\mathbb{D}(\theta)$ matrix, that works only for an interface normal to the z-axis, is not applicable to the oblique mirror with a surface normal vector of $\vec{M}_N = [-\sin(\alpha/2); 0; -\cos(\alpha/2)]$. Thus, an additional coordinate rotation about the propagation vector, $\vec{k}$, has to be operated, of which matrix may be known as the Rodrigues's rotation matrix [137] given by

$$\mathbb{D}_R(\theta_R) = \mathbb{I} + \sin\theta_R\,\mathbb{K} + (1-\cos\theta_R)\mathbb{K}^2, \tag{4.12}$$

where $\mathbb{I}$ denotes an identity matrix, $\mathbb{K} = [0\ -k_3\, k_2;\ k_3\, 0\ -k_1;\ -k_2\, k_1\, 0]$ with $\vec{k} = (k_1, k_2, k_3)$, and θ_R a rotation angle. The θ_R can be mathematically derived from the definition of the inner product between the $\vec{s}$ vector (the direction of the s-component found with tracing matrices up to the $\mathbb{D}(\theta)$ applied) and the desired $\vec{s}_R$ vector created by the requirements that $\vec{s}_R \perp \vec{k}$ and $\vec{s}_R \perp \vec{M}_N$ in the Fresnel reflection geometry. Moreover, another Rodrigues's rotation has to be applied to return the reflected field to the default Cartesian coordinate (x, y, z) basis to proceed further polarization ray tracing. This whole process is in principle possible but mathematically too complicated. This section avoids such an effort with certain assumptions that do not harm PSF prediction.

The two critical questions to be answered in this section are as follows. First, the oblique mirror in the remote space distorts the amplitude and phase of the intermediate image due to the large cone-angle there. Whether this Fresnel reflection over a large range of incident angles significantly degrades image quality has to be examined. Second, a rotationally asymmetric pupil function results in anisotropic PSF, while the use of PBS and QWP also induces another anisotropy in PSF. Whether it is a p- or s-component to be used for the optimal PSF in the oblique imaging mode needs to be determined.

In order to see the effect of the Fresnel reflection at the remote mirror on imaging quality, PSF is first formulated for a flat mirror at zero oblique angle ($\alpha = 0°$). This situation may be the worst case because the range of incidence angles to the mirror is maximized. In Fig. 4.5, the field $\vec{E}_1$ contains only the x-component due to the horizontal polarizer, given as

$$\begin{aligned}\vec{E}_1 &= \sqrt{\frac{1}{\cos\theta_1}}\,\mathbb{P}(0°)\mathbb{R}^{-1}(\pi+\phi_1)\mathbb{L}(\theta_r)\mathbb{R}(\pi+\phi_1)\mathbb{R}^{-1}(\phi_1)\mathbb{L}(\theta_r)\mathbb{L}(\theta_1)\mathbb{R}(\phi_1)\vec{E}_o \\ &= \sqrt{\frac{1}{\cos\theta_1}}\begin{bmatrix}\cos\theta_1\cos^2\phi_1+\sin^2\phi_1 & -(1-\cos\theta_1)\cos\phi_1\sin\phi_1 & -\sin\theta_1\cos\phi_1 \\ 0 & 0 & 0 \\ 0 & 0 & 0\end{bmatrix}\vec{p}.\end{aligned} \tag{4.13}$$

The generalized Jones matrix for a QWP at an azimuthal angle of 45° is expressed from Eq. (2.53) as

$$\mathbb{W}(45°) = \frac{1}{\sqrt{2}}\begin{bmatrix}1 & i & 0 \\ i & 1 & 0 \\ 0 & 0 & \sqrt{2}\end{bmatrix}. \tag{4.14}$$

The recollimated $\vec{E}_3$ field after the reflection from the oblique mirror is then calculated as

$$\begin{aligned}\vec{E}_3 &= \mathbb{W}(45°)\mathbb{R}^{-1}(\phi_2)\mathbb{L}(-\theta_2)\mathbb{D}(\pi-\theta_2)\mathbb{R}_F\mathbb{D}(-\theta_2)\mathbb{R}(\phi_2)\mathbb{R}^{-1}(\pi+\phi_2)\mathbb{L}(\theta_2)\mathbb{R}(\pi+\phi_1)\mathbb{W}(45°)\vec{E}_1 \\ &= \frac{1}{2\sqrt{\cos\theta_1}}\begin{bmatrix}-(r_p+r_s)(\cos\phi_1+i\sin\phi_1)^2(\cos\theta_1\cos^2\phi_1+\sin^2\phi_1) & (r_p+r_s)(\cos\phi_1+i\sin\phi_1)^2(1-\cos\theta_1)\cos\phi_1\sin\phi_1 & (r_p+r_s)(\cos\phi_1+i\sin\phi_1)^2\sin\theta_1\cos\phi_1 \\ -i(r_p-r_s)(\cos\theta_1\cos^2\phi_1+\sin^2\phi_1) & i(r_p-r_s)(1-\cos\theta_1)\cos\phi_1\sin\phi_1 & i(r_p-r_s)\sin\theta_1\cos\phi_1 \\ 0 & 0 & 0\end{bmatrix}\vec{p},\end{aligned} \tag{4.15}$$

where $\theta_1 = \theta_2$ (in the remote focusing), $\phi_1 = \phi_2$, and the Fresnel reflection coefficients for a metallic mirror [120], whose complex refractive index is $N = n + i\kappa$, are

$$r_p = \frac{N^2\cos\theta_1 - n_2\sqrt{N^2 - n_2^2\sin^2\theta_1}}{N^2\cos\theta_1 + n_2\sqrt{N^2 - n_2^2\sin^2\theta_1}} \text{ and } r_s = \frac{n_2\cos\theta_1 - \sqrt{N^2 - n_2^2\sin^2\theta_1}}{n_2\cos\theta_1 + \sqrt{N^2 - n_2^2\sin^2\theta_1}}. \tag{4.16}$$

Two things can be noticed here by comparing $\vec{E}_3$ with $\vec{E}_1$. First, for a perfect metallic mirror where $r_p + r_s = 0$, the x-component of $\vec{E}_3$ completely vanishes. For a real metallic mirror the field strength would be very close to zero. This field is blocked anyway by the horizontal polarizer afterward in the following beam path. Second, after the double passes through the QWP the initial direction of linear polarization rotates by 90° (changed into vertical polarization), but its field distribution keeps unchanged up to the additional apodization factor, $-(r_p - r_s)/2$. For a perfect metallic mirror, this factor becomes a constant of -1. The depolarization by the low NA L4 tube lens is negligible, and thus an anisotropy of PSF is governed by the pupil distribution. This means that for a perfect metallic mirror with a circular pupil, the normalized intensity PSF here is exactly the same with the 90°-rotated intensity PSF in XY imaging mode.

The final field at the exit pupil is given by

$$\begin{aligned}\vec{E}_4 =& \sqrt{\cos\theta_4}\mathbb{R}^{-1}(\phi_1)\mathbb{L}(-\theta_4)\mathbb{R}(\phi_1)\mathbb{P}(90^\circ)\vec{E}_3 \\ =& \frac{i(r_s - r_p)}{2}\sqrt{\frac{\cos\theta_4}{\cos\theta_1}}\begin{bmatrix} -(\cos\theta_1\cos^2\phi_1 + \sin^2\phi)(1-\cos\theta_4)\cos\phi_1\sin\phi_1 & (1-\cos\theta_1)(1-\cos\theta_4)\cos^2\phi_1\sin^2\phi_1 & (1-\cos\theta_4)\sin\theta_1\cos^2\phi_1\sin\phi_1 \\ (\cos\theta_1\cos^2\phi_1 + \sin^2\phi_1)(\cos\theta_4\sin^2\phi_1 + \cos^2\phi_1) & -(1-\cos\theta_1)\cos\phi_1\sin\phi_1(\cos\theta_4\sin^2\phi_1 + \cos^2\phi_1) & -\sin\theta_1\cos\phi_1(\cos\theta_4\sin^2\phi_1 + \cos^2\phi_1) \\ -(\cos\theta_1\cos^2\phi_1 + \sin^2\phi_1)\sin\theta_4\sin\phi_1 & (1-\cos\theta_1)\sin\theta_4\cos\phi_1\sin^2\phi_1 & \sin\theta_1\sin\theta_4\cos\phi_1\sin\phi_1 \end{bmatrix}\vec{p}.\end{aligned} \tag{4.17}$$

It can be found that the final wave vector with the same tracing matrices results in $\vec{k}_4 = [-\sin\theta_4\cos\phi_1; -\sin\theta_4\sin\phi_1; -\cos\theta_4]$ as anticipated. Multiplying a converging wave feature at the exit pupil of $\frac{e^{-ikf_4}}{f_4}$ to $\vec{E}_4$, followed by an evaluation of the vectorial Debye integral Eq. (2.6) with $\hat{N} = [-\sin\theta_4\cos\phi_1; -\sin\theta_4\sin\phi_1; -\cos\theta_4]$ over the circular exit pupil, yields the amplitude PSF in the cylindrical image coordinate (ρ, ϕ, z) as

$$\vec{E} = \frac{1}{i\bar{\lambda}}\frac{\pi}{4}\begin{bmatrix} A_2^3\sin(2\phi) + A_4^1\sin(4\phi) & A_0^2 - A_4^1\cos(4\phi) & -iA_1^2\sin\phi + iA_3^1\sin(3\phi) \\ A_0^1 - A_2^2\cos(2\phi) - A_4^1\cos(4\phi) & A_2^1\sin(2\phi) - A_4^1\sin(4\phi) & iA_1^1\cos\phi - iA_3^1\cos(3\phi) \\ iA_1^4\sin\phi + iA_3^2\sin(3\phi) & -iA_1^3\cos\phi - iA_3^2\cos(3\phi) & -A_2^4\sin(2\phi) \end{bmatrix}\vec{p}, \tag{4.18}$$

where

$$A_p^q = \int_0^{\alpha_4}\sqrt{\frac{\cos\theta_4}{\cos\theta_1}}\frac{i(r_s - r_p)}{2}\,F_p^q(\theta_1,\theta_4)\,J_p(k\rho\sin\theta_4)\,e^{-i\bar{k}z\cos\theta_4}\sin\theta_4\,d\theta_4, \tag{4.19}$$

where $\alpha_4 = \sin^{-1}\left(\frac{NA_2}{M}\right)$ with

$$\begin{aligned}
F_0^1(\theta_1,\theta_4) &= (1+3\cos\theta_1+3\cos\theta_4+\cos\theta_1\cos\theta_4), & F_0^2(\theta_1,\theta_4) &= (1-\cos\theta_1)(1-\cos\theta_4), \\
F_1^1(\theta_1,\theta_4) &= 2\sin\theta_1(3+\cos\theta_4), & F_1^2(\theta_1,\theta_4) &= 2\sin\theta_1(1-\cos\theta_4), \\
F_1^3(\theta_1,\theta_4) &= 2(1-\cos\theta_1)\sin\theta_4, & F_1^4(\theta_1,\theta_4) &= 2(3+\cos\theta_1)\sin\theta_4, \\
F_2^1(\theta_1,\theta_4) &= 2(1-\cos\theta_1)(1+\cos\theta_4), & F_2^2(\theta_1,\theta_4) &= 4(\cos\theta_1-\cos\theta_4), \\
F_2^3(\theta_1,\theta_4) &= 2(1+\cos\theta_1)(1-\cos\theta_4), & F_2^4(\theta_1,\theta_4) &= 4\sin\theta_1\sin\theta_4, \\
F_3^1(\theta_1,\theta_4) &= 2\sin\theta_1(1-\cos\theta_4), & F_3^2(\theta_1,\theta_4) &= 2(1-\cos\theta_1)\sin\theta_4, \\
F_4^1(\theta_1,\theta_4) &= (1-\cos\theta_1)(1-\cos\theta_4). & &
\end{aligned}$$

The averaged intensity PSF can be calculated by incoherently summing the above intensity for $\vec{p}$ over the 4π solid angle, Eq. (4.7).

The derived PSF was numerically evaluated to see how critical is to consider the Fresnel reflection in PSF formulation. The simulation parameters for the optical setup were set as follows: two identical oil-immersion objective lenses with $n = 1.516$ at $\bar{\lambda} = 572$ nm (for two NA cases: 1.40 and 1.49), and the L4 focal length of 200 mm. Three different metals as potential oblique mirrors were considered: gold (Au) with its complex refractive index of $0.24904+i2.8974$, silver (Ag) with $0.14802+i3.3563$, and aluminium (Al) with $1.0424+i6.6303$ at around 572 nm [138]. As shown in Fig. 4.7, the metallic mirrors slightly stretch the PSF compared to the perfect mirror case. More stretch occurs along the narrower PSF direction (y), at the higher NA, and for metals: Au > Ag > Al. The FWHM is a key parameter in

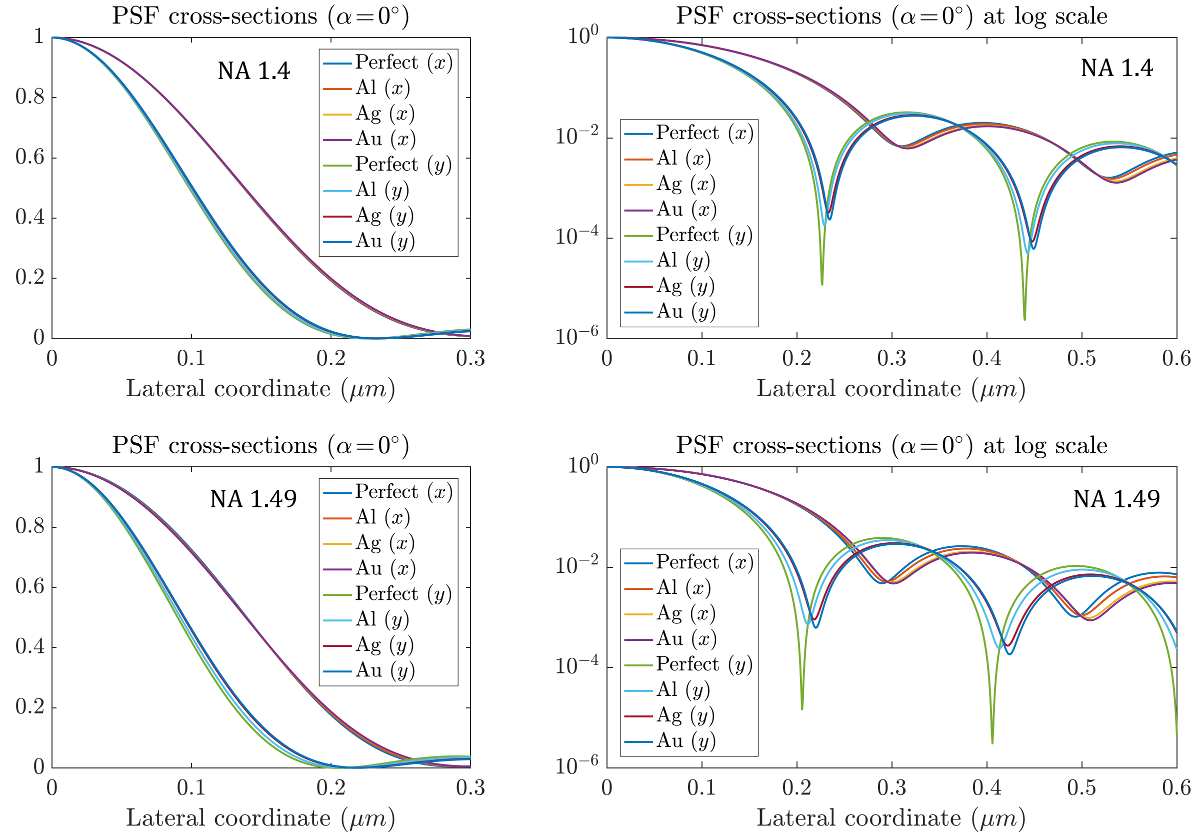

Figure 4.7: Cross-sections of theoretical PSFs at $\alpha = 0°$: (top row) 1.4 NA, FWHM_x: 275.1, 275.4 (+0.1%), 276.3 (+0.4%), 276.5 nm (+0.5%) for the perfect, Al, Ag, Au mirrors ($\bar{\lambda} =$ 572 nm), respectively. FWHM_y: 196.8, 198.6 (+0.9%), 201.4 (+2.3%), 202.1 nm (+2.7%). (bottom row) 1.49 NA, FWHM_x: 277.8, 278.0 (+0.1%), 278.3 (+0.2%), 279.1 nm (+0.5%), FWHM_y: 180.1, 184.3 (+2.3%), 189.0 (+4.9%), 190.0 nm (+5.5%). The metallic mirror increases the FWHM to a negligible degree.

STORM that determines a localization precision. The largest FWHM deviation compared with the perfect mirror case is at 1.49 NA with a gold mirror by 5.5% (y) and 0.47% (x), respectively. At 1.4 NA, it is smaller: 2.7% (y) and 0.5% (x) with the Au mirror. These FWHM increases are still negligibly small and the oblique mirror could be considered as a perfect mirror. (If such metallic mirrors have any protection coatings or oxidized layers, their effects need to be investigated.)

Interestingly, while the first minimum of PSF$_\mathrm{x}$ (highly related to the OTF cutoff frequency or the pupil size) occurs earlier at 1.49 NA than at 1.40 NA as expected, the FWHM$_\mathrm{x}$ at 1.49 NA is rather slightly larger. To unravel this more closer examination on pupil distributions would be necessary.

Another viewpoint of indirectly looking at the influence of the oblique mirror on PSF is to inspect the added complex apodization term: $(r_s – r_p)/2$ (see Fig. 4.8). At $\alpha = 0^\circ$ this term may be approximated as the $\sqrt{\cos\theta}$ apodization. The phase change is much smaller than the conventional diffraction-limited criteria (RMS wavefront error $< 0.071\lambda$) and thus could be neglected. If so, it was already found in Chapter 2 that such the apodization minorly influences on PSF. Moreover, as an oblique angle increases, the average AOI over the pupil is lowered except at the two corners around θ_max (see the AOI maps). Hence, the PSF would be less affected by this complex amplitude term to a negligible extent.

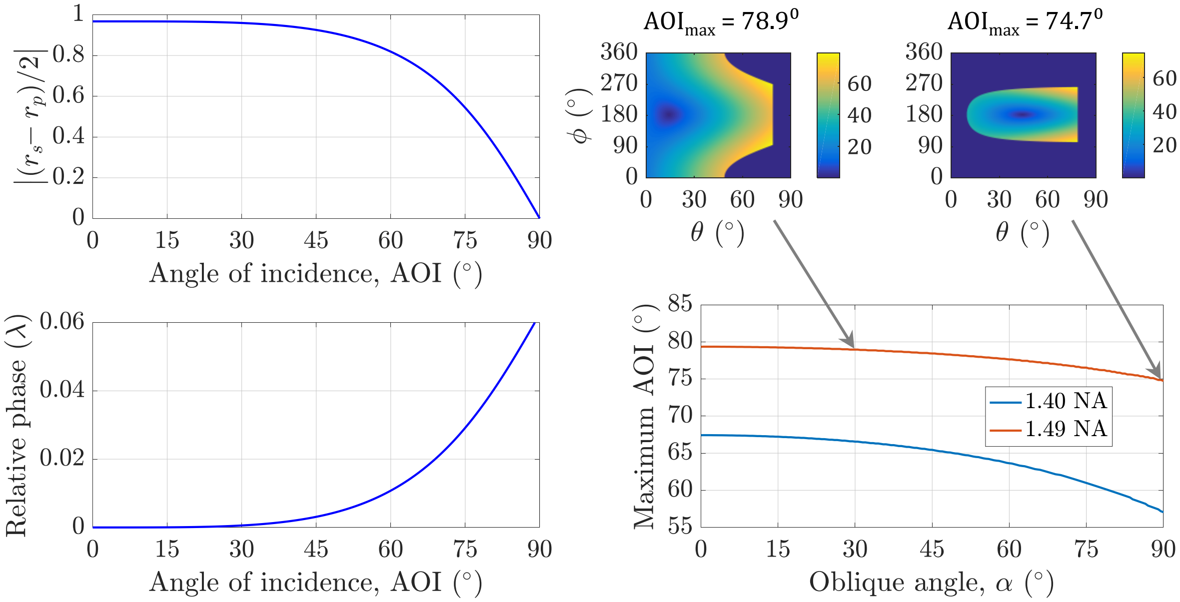

Figure 4.8: Interpretation of the complex amplitude term $(r_s - r_p)/2$ added on PSF formulation. (left) the magnitude and relative phase of the term over an incident angle (AOI) with an Ag mirror ($n = 1.516$). (right) maximum AOI calculated over oblique angles. The term may be approximated as a constant for $NA < 1.40$ (AOI $< 67.4^\circ$) or roughly the $\sqrt{\cos\theta}$ apodization near 1.49 NA, either of which negligibly changes the mainlobe of PSF.

Based on these considerations, the actual intensity PSF in oblique mode could be evaluated using the vectorial Debye integral over the oblique pupil, Eq. (4.9), with an approximate field strength at the exit pupil as Eq. (4.17) with $(r_s - r_p)/2 \approx -1$. This field is correct for a perfect oblique mirror even when $NA_2 > NA_1$. Then, of course, the half-cone angle θ_1 has to be replaced by θ_2 in the equations. Another case of interest is when the incoming light right after the L3 lens in Fig. 4.5 is vertically polarized. This can be realized by axially rotating the PBS by 90°, in the model equivalently being a vertical polarizer for the forward beam path and a horizontal polarizer for the backward beam path. In that case, the field at the exit pupil can be approximately found as

$$\vec{E}_4 = i\sqrt{\frac{\cos\theta_4}{\cos\theta_1}} \begin{bmatrix} (1-\cos\theta_1)\cos\phi_1\sin\phi_1(\cos\theta_4\cos^2\phi_1+\sin^2\phi_1) & -(\cos\theta_1\sin^2\phi_1+\cos^2\phi_1)(\cos\theta_4\cos^2\phi_1+\sin^2\phi_1) & \sin\theta_1\sin\phi_1(\cos\theta_4\cos^2\phi_1+\sin^2\phi_1) \\ -(1-\cos\theta_1)(1-\cos\theta_4)\cos^2\phi_1\sin^2\phi_1 & (\cos\theta_1\sin^2\phi_1+\cos^2\phi)(1-\cos\theta_4)\cos\phi_1\sin\phi_1 & -(1-\cos\theta_4)\sin\theta_1\cos\phi_1\sin^2\phi_1 \\ -(1-\cos\theta_1)\sin\theta_4\cos^2\phi_1\sin\phi_1 & (\cos\theta_1\sin^2\phi_1+\cos^2\phi_1)\sin\theta_4\cos\phi_1 & -\sin\theta_1\sin\theta_4\cos\phi_1\sin\phi_1 \end{bmatrix} \vec{p}. \tag{4.20}$$

Alternatively, one could keep the field as Eq. (4.17) while rotating the boundary of $\phi_2(\theta_2)$ by 90° in Eq. (4.9).

The intensity PSF was simulated for the two different directions of input polarization at the extreme oblique angle of 90° as shown in Fig. 4.9. It was previously found from the XY mode analysis that the field distribution over a circular aperture for the horizontal input polarization elongates PSF$_x$. On top of that, in oblique mode the narrower pupil along the

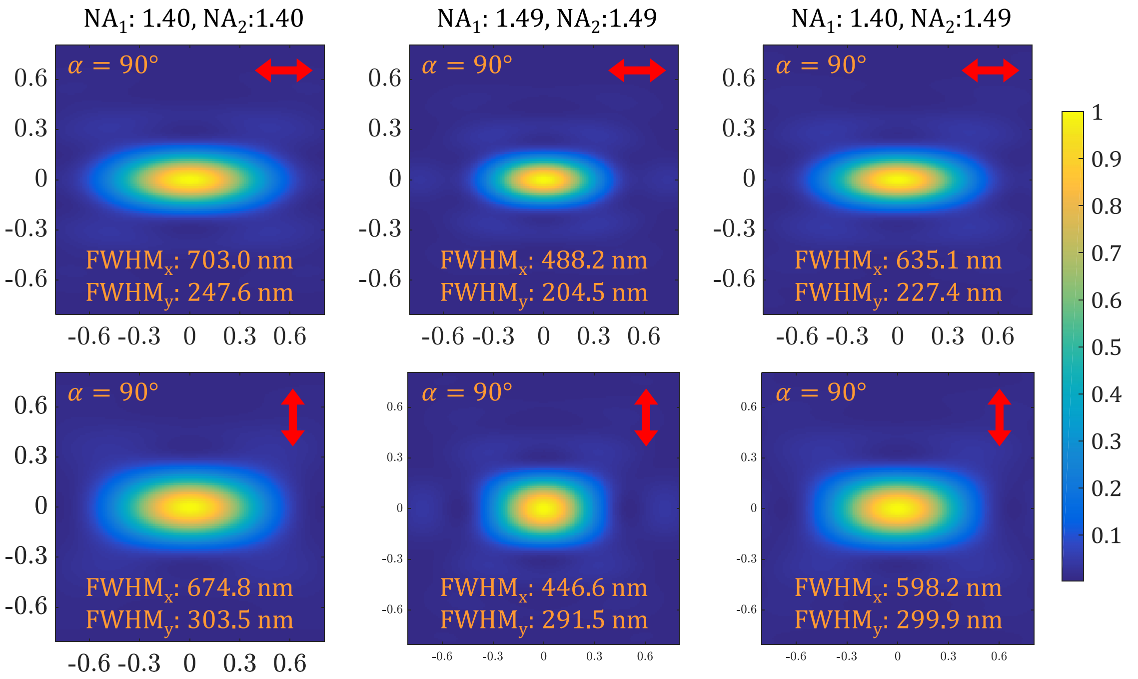

Figure 4.9: Theoretical in-focus intensity PSF in oblique mode ($\alpha = 90°$) with horizontal or vertical directions (red arrows) of input polarization ($n = 1.516$ at $\bar{\lambda} = 581\,nm$). The axis unit is μm. Vertical input polarization helps to relax the anisotropy of the PSF.

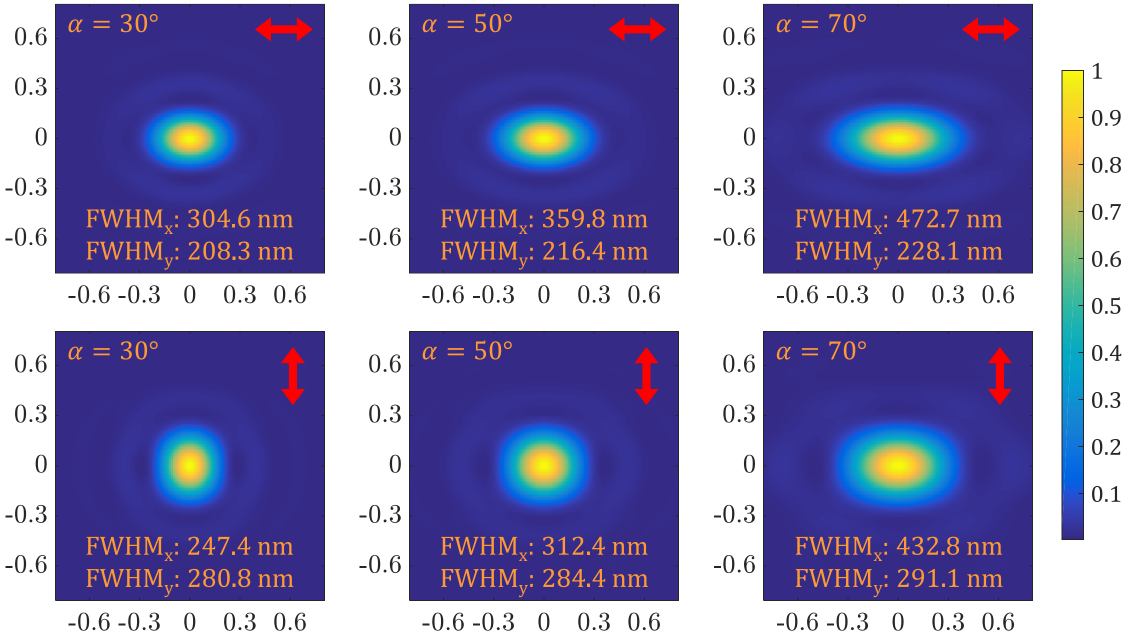

Figure 4.10: Theoretical in-focus intensity PSF at different oblique angles with horizontal and vertical directions of input polarization (NA$_1$=NA$_2$=1.40 with n=1.516 at $\bar{\lambda}$=581 nm). The axis unit is μm. Overall, a less elliptical PSF results with vertical input polarization.

horizontal direction due to the pupil loss even further stretches the resulting PSF (top row). The double stretches could be avoided by applying vertical input polarization. The bottom row in Fig. 4.9 shows such a situation. At $\alpha = 90°$, however, the FWHM$_x$ is enhanced only by less than 10% at the expense of FWHM$_y$ degradation more than 20%. Thus horizontal input polarization may still be better considering the localization precision that results in STORM. At other smaller oblique angles, vertical input polarization certainly improves the ellipticity of PSF (see Fig. 4.10). At $\alpha = 30°$, the PSF elongation along x direction due to the pupil loss occurs in a less degree than its vertical stretch due to the pupil distribution from vertical input polarization. At $\alpha = 50°$, the pupil loss slightly exceeds the pupil distribution effects, resulting in the horizontally stretched PSF. A ratio of FWHM$_y$ to FWHM$_x$ is calculated in Fig. 4.11. As discussed in Chapter 3, the major and minor pupil loss occurs along the x and y direction respectively, and thus the change in the FWHM$_x$ is more sensitive to the oblique angle. With the vertically polarized input wave, the initial FWHM$_y$ at $\alpha = 0°$ starts at above the FWHM$_x$. Thus a balanced oblique angle where the PSF becomes isotropic exists: 42° at 1.4 NA and 60° at 1.49 NA.

It is concluded that the layout of the PBS in Fig. 4.1 which affects the PSF's anisotropy in oblique imaging mode needs to be carefully designed. In general microscopy applications where an isotropic resolution is preferred, the s-polarized (vertical) input wave should be configured perpendicular to the narrower pupil direction caused by the oblique mirror.

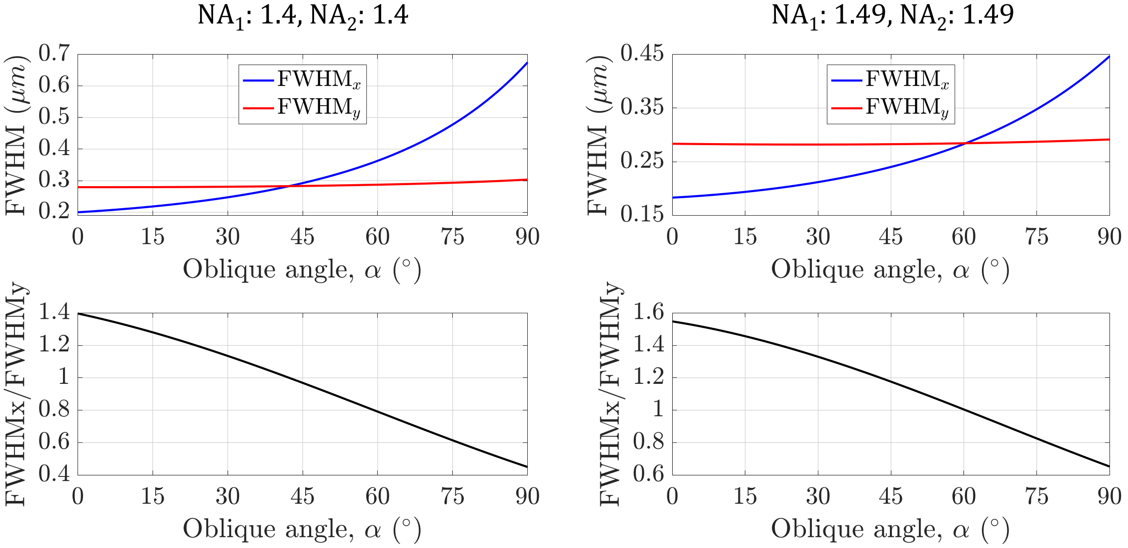

Figure 4.11: A FWHM$_y$/FWHM$_x$ ratio over oblique angles with vertical input polarization (n = 1.516 at $\bar{\lambda}$ = 581 nm). An isotropic PSF occurs at 42° (1.4 NA) and 60° (1.49 NA).

4.4 Analysis on super-resolution

Spatial resolution in localization microscopy is determined by both a labeling density and a localization precision. If a sample has enough dye molecules labeled above the Nyquist sampling criteria (at least 2x denser labeling than the required resolution, for example, $>10^4$ dyes/μm^2 for 20 nm resolution), then the resolution is mainly related with the 2D localization precision (σ) approximately given [139] by

$$\sigma \approx \sqrt{\frac{\sigma_{\mathrm{PSF}^2}}{N_P} + \frac{p^2/12}{N_P} + \frac{8\pi\sigma_{\mathrm{PSF}}^4\sigma_{\mathrm{bg}}^2}{p^2N_P^2}}, \tag{4.21}$$

where σ_{PSF} denotes typically the size (1σ) of PSF, N_P the number of photons collected, p the size of the sampling pixel ($p < \sigma_{\mathrm{PSF}}$), σ_{bg} background noise. The three terms inside the root consider shot noise, pixelation noise, and background noise, respectively. Or simply the shot-noise limited precision is widely used as a quick estimate: $\sigma \geq \sigma_{\mathrm{PSF}}/\sqrt{N_P}$ [140]. The FWHM-based localization precision is often considered as STORM resolution: $\mathrm{FWHM} = 2\sqrt{2\,ln(2)}\sigma$ for a Gaussian PSF.

For more practical estimation of resolution in *oblique*STORM, not only σ_{PSF} and N_P but also an empirical constant that connects the simplified inequality above would be necessary. For this purpose, three representative STORM studies [134, 141, 142] were referenced. On average, the lateral localization precision of around 8.5 nm was reported with the average 5200 photons/switching over typically 40-50 ms dwell time. In their experimental condition (1.4 NA with Alexa Fluor 647 dyes, $\bar{\lambda} \approx 671\,nm$), theoretically $\sigma_{\mathrm{PSF}} \approx 115\,nm$. This may

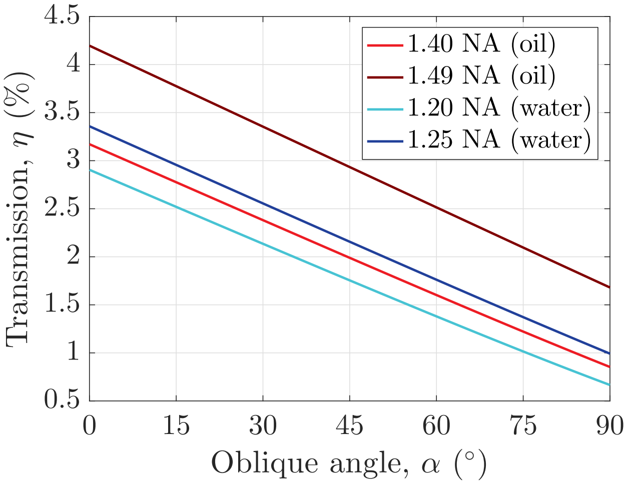

Figure 4.12: Overall transmission in *oblique*STORM at different objective NA ($n_{\text{oil}} = 1.516$, $n_{\text{water}} = 1.333$ at $\bar{\lambda} = 581\,nm$). For comparison, conventional STORM shows typically $\eta = 10\%$.

lead to an approximate empirical relation: $\sigma = C \cdot \sigma_{\text{PSF}}/\sqrt{N_P}$ with $C = 5.33$ for organic dye molecules. Typical overall transmission of these systems is around 10% (1.4 NA) from the multiplication of a spatial efficiency (objective's solid angle and each optical component's transmission) and a spectral efficiency (pass bands of emission filters and the EMCCD's quantum yield) (the detailed calculation is excluded here). The efficiency in *oblique*STORM is lower than the conventional STORM setup due to the use of additional remote objective lens (usually 85% per pass) and its pupil loss as well as the PBS loss (50%). Taking these and other minor transmission losses into account, the overall efficiency is roughly estimated as shown in Fig. 4.12. If a relative transmission value of the pupil loss is considered geometrically compared with the circular pupil ($\alpha = 0°$) area, it decreases from 1 ($\alpha = 0°$) to 0.269 ($\alpha = 90°$) with almost a linear slope of -0.008154/α. Compared with the typical STORM efficiency of 10%, the proposed method shows approximately 3-10x lower efficiency depending on the oblique angle.

The resolution of *oblique*STORM is finally estimated for both an oil-immersion system (Fig. 4.13) and a water-immersion system (Fig. 4.14). The PSF was calculated at the preferred system geometry about polarization (concluded in the previous section) at a wavelength of 581 nm (which is an average emission wavelength of Cy3B organic dyes.) The same 5200 reference photon counts at 10% efficiency was used here for Cy3B dyes whose photon yields could be adjusted to the similar level by controlling illumination density [143]. For the oil immersion system, the resolution is superior thanks to the smaller PSF from the higher immersion index. At $\alpha = 42°$, isotropic sub-50-nm resolution (46 nm) with a widely used 1.4 NA objective is attainable. It was reported that 3.5x more photons can be easily extracted with the conventional STORM buffer with the cyclooctatetraene (COT) added in organic dyes thanks to the direct quenching mechanism [144]. If used, sub-25-nm resolution at 42°

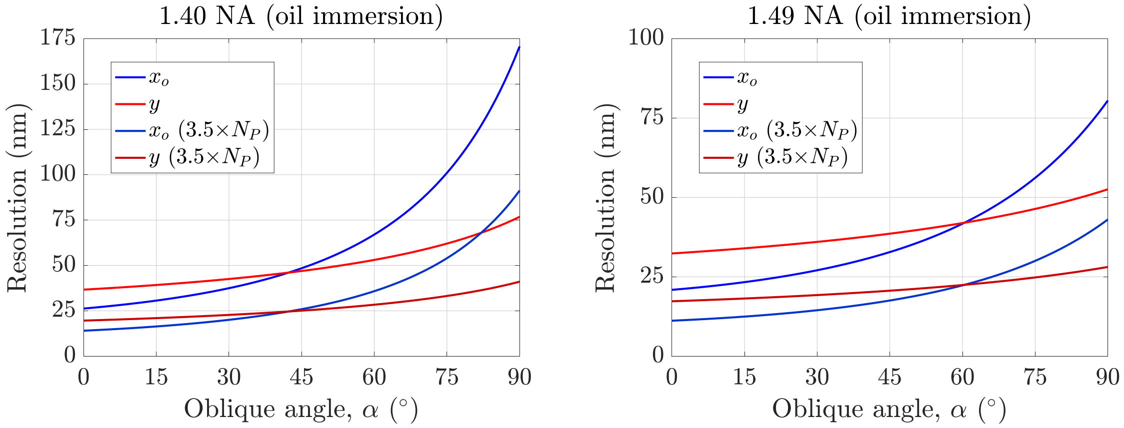

Figure 4.13: Predicted resolution of oil-immersion *oblique*STORM (x_o: oblique axis (horizontal), y: vertical axis) over oblique angles. The PSF was evaluated at $\bar{\lambda}=581$ nm. Improved resolution curves with 3.5x more photons are also estimated.

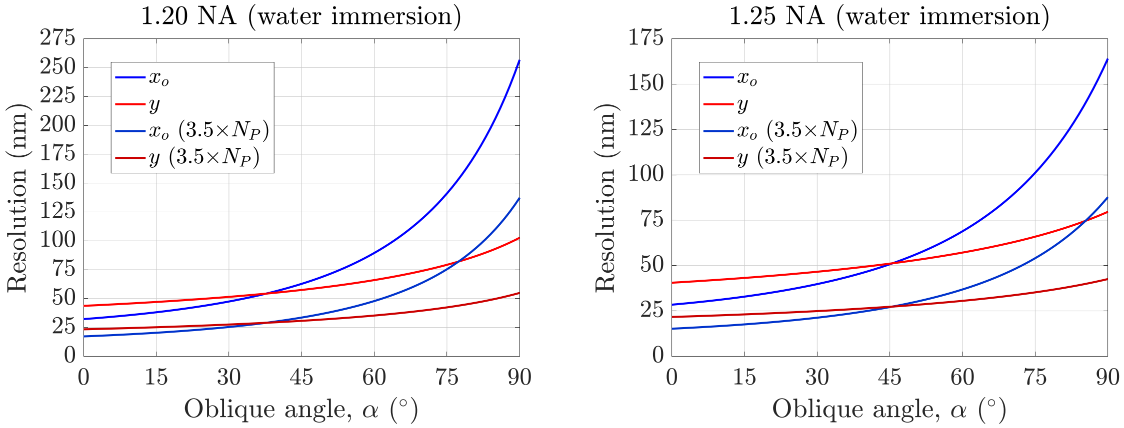

Figure 4.14: Predicted resolution of water-immersion *oblique*STORM (x_o: oblique axis (horizontal), y: vertical axis) over oblique angles. The PSF was evaluated at $\bar{\lambda} = 581$ nm. Improved resolution curves with 3.5x more photons are also estimated.

and sub-100-nm resolution over all possible oblique angles would be possible. At 1.49 NA (which is less practical), an isotropic resolution of 42 nm (or 23 nm with COT) is predicted at $\alpha = 61°$. A reduced oblique angle to 42° lowers resolution to 38 nm (or 20 nm with COT). Since a maximum oblique angle for lightsheet illumination is limited by the objective NA, an available oblique angle should be larger than 24° (11°) at 1.40 NA (1.49 NA). The actual operating angle may depend on many requirements such as resolution, penetration depth, sample orientation, etc. In general lower oblique angles offer better resolution but less penetration depth. For the resolution point of view an operating angle smaller than 45° may be preferred, while for larger penetration depth an oblique angle larger than 45° is recommended. Given that the number of pixels available in EMCCD is finite (typically 1000 pixels for each dimension) and the best pixel size [139] is about equal to $\sigma_{\mathrm{PSF}} = 122$ nm at 1.4 NA ($\alpha = 45°$), penetration depth would be more or less 86 μm along the axial direction. In a subpixel readout (in practice), penetration depth could still be maintained by keeping the whole pixels on along that direction.

For biological samples, water immersion system could be used with an isotropic resolution of 55 nm (or 29 nm with COT) at $\alpha = 38°$ with 1.2 NA. The 1.2 NA is widely used and sub-100-nm resolution with COT would be achievable. The 1.25 NA is also available, which slightly enhances resolution to 50 nm (or 27 nm with COT). A larger PSF in water immersion system may allow larger spatial sampling resolution and thus further extend penetration depth by around 10%.

If only one oblique angle has to be chosen in *oblique*STORM, the best angle would be around 42° which gives an isotropic resolution between oil and water immersion systems if switched back and forth.

4.5 Penetration depth in ***oblique*STORM**

In previous section, penetration depth in the aspect of a camera's field of view was around 80 μm. However, actual working depth would be limited by the residual aberration associated with the remote focusing. As was done in Section 3.5, the working range in *oblique*STORM is similarly investigated here.

The vectorial Strehl ratio in fluorescence imaging (with a freely rotating dipole point source) would have a sightly different form from Eq. (3.15). In fact, for the suggested PBS/QWP layout, the electric field (or axial response) at the remote space along the optical axis at $\alpha = 0°$ can be derived as

$$\vec{E}(z_1; z_2) = \frac{\pi}{i\bar{\lambda}4\sqrt{2}} \int_o^{\alpha_2} \begin{bmatrix} -i(1-\cos\theta)^2 & i(1+6\cos\theta+\cos^2\theta) & 0 \\ i(1-\cos\theta)^2 & (3+2\cos\theta+3\cos^2\theta) & 0 \\ 0 & 0 & -4\sin^2\theta \end{bmatrix} \vec{p} \times e^{i\bar{k}(W(\theta; z_1, z_2)+n_2 z_2\cos\theta)} \sin\theta \, d\theta d\phi, \tag{4.22}$$

where $\alpha_2 = \sin^{-1}(NA_2/n_2)$ and $W(\theta; z_1, z_2)$ denotes the aberration function in the remote focusing given in Eq. (3.12). If the polarizer/QWP is replaced by a nonpolarizing beam splitter, the axial response is calculated as

$$\vec{E}(z_1; z_2) = \frac{\pi}{i\bar{\lambda}} \int_o^{\alpha_2} \begin{bmatrix} 1+\cos^2\theta & 0 & 0 \\ 0 & 1+\cos^2\theta & 0 \\ 0 & 0 & -2\sin^2\theta \end{bmatrix} \vec{p} e^{i\bar{k}(W(\theta; z_1, z_2)+n_2 z_2\cos\theta)} \sin\theta \, d\theta d\phi. \tag{4.23}$$

The normalized intensity axial response for fluorophores free to rotate is obtained by $\sum_{uv} |E_{uv}|^2$, Eq. (4.7), normalized by the maximum intensity when $z_1 = z_2 = 0$. Considering the Strehl ratio primarily governed by the exponential term in the above equations rather than the

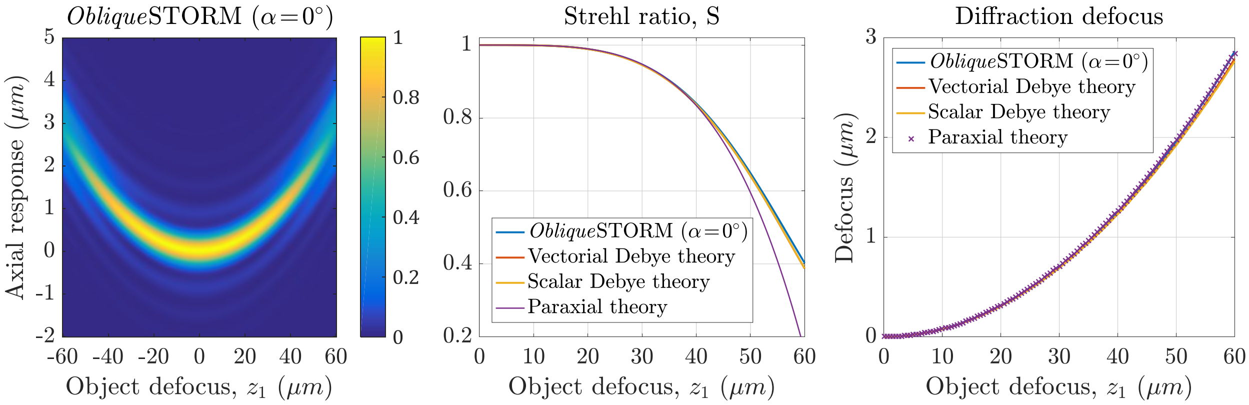

Figure 4.15: Simulation of Strehl ratio and diffraction defocus in *oblique*STORM at $\alpha = 0°$. Objective NA: 1.4 ($f = 1.8$ mm, $n = 1.516$ at $\bar{\lambda} = 572$ nm).

apodization matrix, the two different derivations would result in very similar behavior, even similar with the scalar Debye Strehl ratio in Eq. (refeqn:ScalarDebyeStrehlRatio). In fact, as calculated in Fig. 4.15 for 1.4 NA (oil immersion), they all produce almost the same Strehl ratio and diffraction defocus within a few % tolerance, except the paraxial Strehl ratio. Based on the diffraction-limit cutoff ($S = 0.81$), an axial working range is predicted to be 84 μm which is as deep as the maximum available FOV estimated in previous section. There occurs a diffraction defocus of a few microns which would need to be compensated during post processing of localization data. Penetration depth in a water-immersion system would be deeper thanks to less residual aberration in Eq. (3.13) as water-immersion objectives typically have smaller numerical aperture and longer focal length.

In order to experimentally verify working range, on top of the optical setup described in Section 4.2 for PSF measurement in XY mode, additional optical components were aligned to have a complete configuration of the oblique imaging mode: another Olympus UPLSAPO objective (100XO, 1.4 NA) in the remote space, a protected Ag remote mirror (PF10-03-P01, Thorlabs) at $\alpha = 0$, L4 tube lens (AC254-200-A-ML), achromatic QWP (AQWP05M-600, Thorlabs). The 200-nm-diameter orange fluorescent beads (F8809, Molecular Probes™) were prepared with the similar steps detailed in Section 4.2 with a 300x dilution. An average emission wavelength was 572 nm based on the spectra of the bead fluorescence and the emission filter used. A solid state green laser (532 nm) was added for sample excitation.

To measure Strehl ratio and diffraction defocus, a PZT (piezoelectric transducer) actuator on the sample stage (z_1 axis) was stepped by 10 μm through focus and another PZT actuator on the remote mirror (z_2 axis) was tuned to yield the best (well focused) PSF seen by an oblique mode camera (Luca R, Andor). The bead images were recorded at each stepping and post processed to obtain an experimental Strehl ratio as obtained in Fig. 4.16. The data from the six beads were used to extract Strehl ratio. The fluorescence signal was faded away as the measurement goes on, and thus the peak intensity of each bead was normalized by its beam power (estimated from 2D Gaussian beam fittings). Experimental working depth

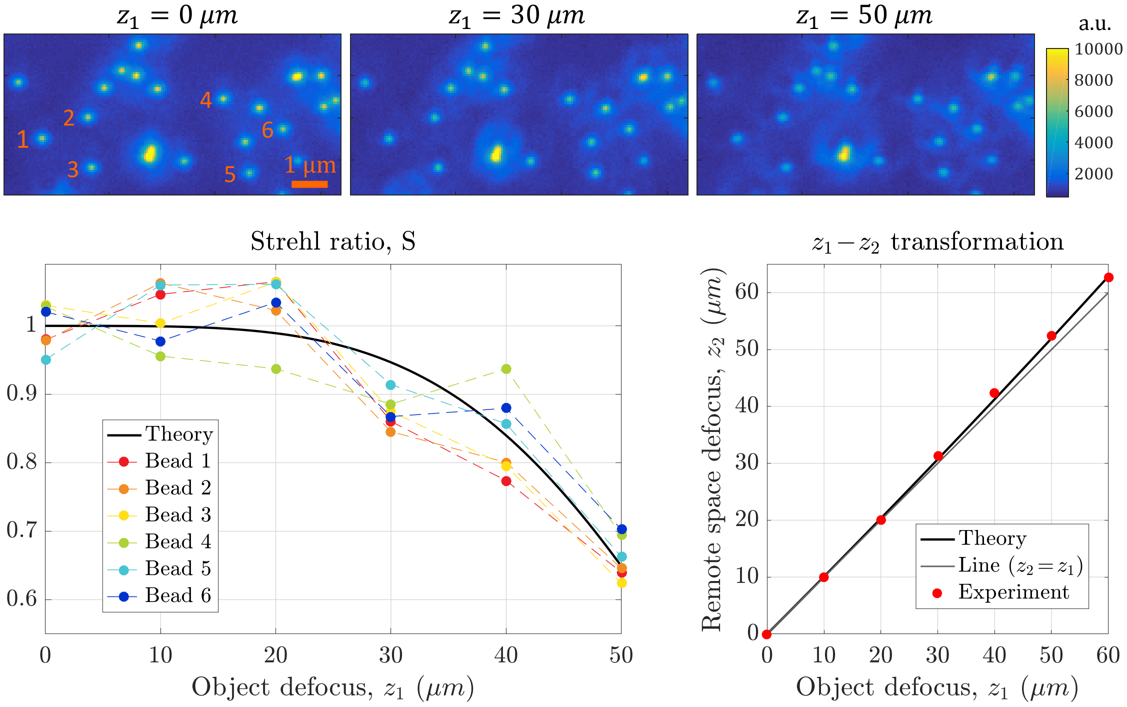

Figure 4.16: Measurement of Strehl ratio and z_1–z_2 relation in oblique imaging mode ($\alpha = 0°$) using 200-nm-diameter orange fluorescent beads. For the beads located at different z_1, the position of the remote mirror (z_2) was tuned to find the best PSF as shown in the top three bead images. The experimental Strehl ratio and the coordinate relation corroborate the theory. Working depth is found to be around 80 μm.

turned out to be around 80 μm which agrees well with the theoretical prediction. The stretch of the z_2 coordinate due to the diffraction defocus also greatly follows the theory.

At higher oblique angles, it is expected that working depth would be at least maintained or even extended due to the reduced pupil area, *i.e.*, smaller RMS wavefront error, of which argument may still need experimental confirmation. Throughout this section, any non-ideal effects of samples (scattering and autofluorescence, etc) that may potentially further limit actual penetration depth have not been included. These would also need experimental validation.

4.6 Preliminary super-resolution experiment

Experimental setup of *oblique*STORM

Figure 4.17 shows an experimental setup of *oblique*STORM on an anti-vibration table. The typical up-right or inverted microscope configuration was avoided to minimize mechanical

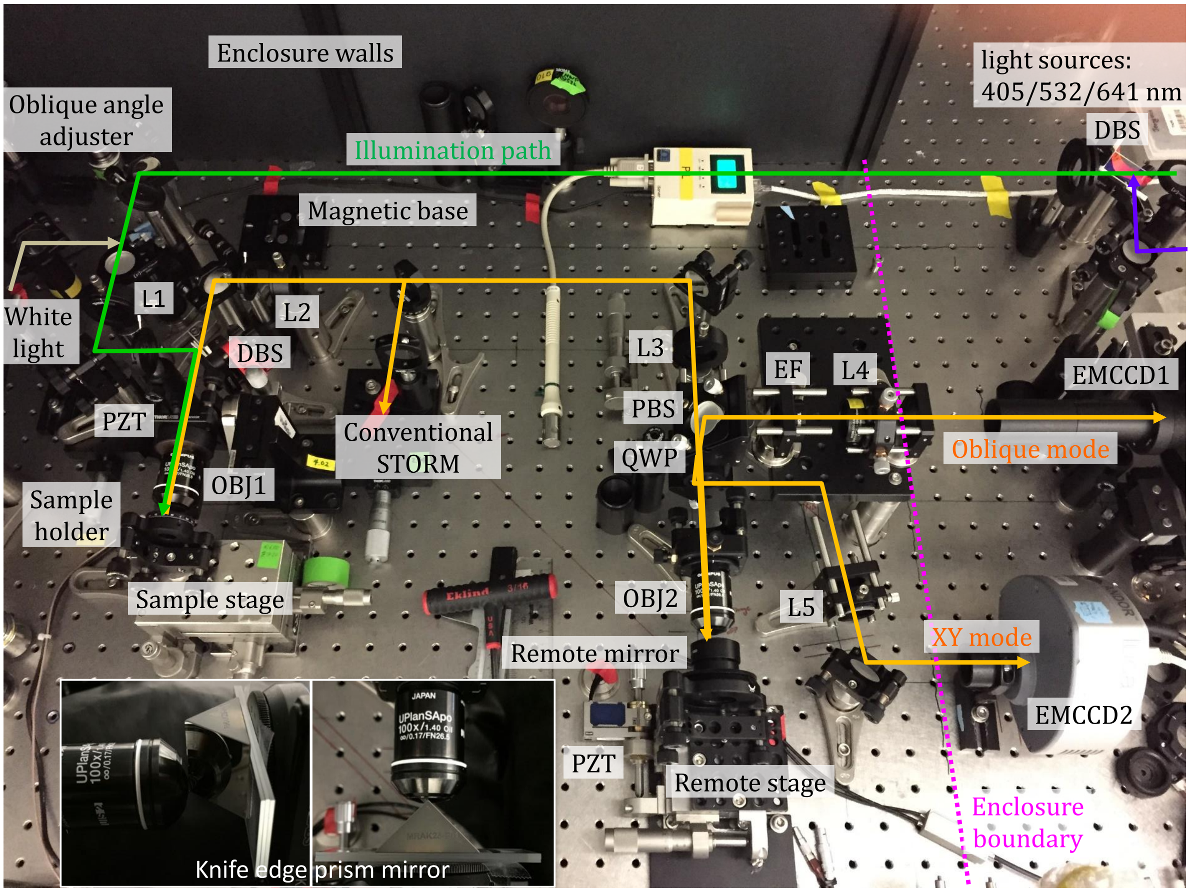

Figure 4.17: Experimental setup of *oblique*STORM. A pair of cylinder lenses that can be mounted on the magnetic base is not shown here. The PBS was placed to direct the s-polarized light (XY mode) downward to the table and the p-polarized light upward (oblique mode). The inset shows photos of a knife edge prism mirror for $\alpha = 90°$. The whole setup is closed by an optical enclosure (not fully shown) excluding laser heads and EMCCD cameras.

vibrations and drifts.

There are several important considerations needed to build *oblique*STORM. The flatness of the dichroic beam splitter (DBS) and its thickness can be critical. For a quality lightsheet profile (diffraction-limited performance), the DBS's flatness should be at least better than 1/2 wave P-V per inch. The remote focusing involves non-collimated beams passing through the DBS and thus its thickness should be as thin as possible to minimize undesirable aberrations induced. A marginal thickness was estimated around 1 mm according to geometrical ray tracing in ZEMAX software. Many commercial DBS has very good flatness ($< \lambda/10$) at 3 mm thickness, but this would be unsatisfactory. A 1-mm thickness DBS should be chosen with as good flatness as available. A thickness of another DBS in the laser source side (collimated beams) can be thick as long as its flatness is satisfactory. Also, typical STORM setups introduce a single mode (or multi-mode) fiber to combine multiple laser sources which then no longer requires optical alignment color by color. In *oblique*STORM, this schematic may not be practically a good idea if multiple lasers are to be simultaneously used for illumination. Unless the whole illumination optics are super-achromatized, a lightsheet alignment done at one wavelength would not remain as good in other wavelengths. Thus coupling lasers in free space is recommended. Each laser may have a beam expander to individually tune thickness and focus of lightsheet illumination as desired. Moreover, objective lenses should be carefully chosen. These days many objective lenses are designed with infinity corrections yet still partly rely on a particular tube lens for LCA (lateral chromatic aberration) correction. Thus the internally corrected objective lenses (for example, Olympus) are required to guarantee performance of remote focusing. Besides, for minimal image drifts, the mechanical stages for a sample and the remote mirror should be carefully chosen, especially if real-time drift compensation is not available. A commercial stainless steel, precision XYZ positioning stage (562-XYZ, Newport Corporation) showed a drift of less than 20 nm for 10 minutes in all dimensions.

Super-resolution test using SiO_2 nanowire

To test STORM, monodispersed silicone nanowires (diameter: 40 nm) were oxidized in a furnace (in air) at 800°C for two hours for transparency (also to ensure that wire surfaces have -OH). The oxidized nanowires were then aminosilanated by 3-Aminopropyltriethoxysilane (APTS, 440140, Sigma-Aldrich), followed by labeling with Alexa Fluor 647 NHS ester (A20006, Molecular Probes™) dissolved in DMSO (D12345, Molecular Probes™). A simple STORM buffer (Vectashield, H-1000, Vector Laboratories) [145] was utilized as a mounting medium. The prepared sample was excited by the 641 nm laser alone at an illumination density at around 2 $\mathrm{kW/cm^2}$ and fluorescence signals were captured by the Olympus UPLSAPO objective (100XO, 1.4 NA) with two bandpass emission filters (FF01-446/510/581/703-25, Semrock). STORM video were recorded at 20 Hz (frame transfer mode) by an EMCCD camera (Luca R, Andor), and then processed with home-built MATLAB codes for both localization and image reconstruction. Figure 4.18 shows a fluorescence image of a nanowire at lower illumination intensity (< 0.1 $\mathrm{kW/cm^2}$) and its super-resolution image reconstructed. The diameter of the nanowire was measured to be 50-60 nm in STORM. This would be a correct dimension due to the increased diameter after the oxidization step of the 40 nm Si nanowires.

Future work

The fundamental analysis necessary to design and build *oblique*STORM and corresponding experimental corroboration were conducted in this chapter. A whole cycle of super-resolution imaging from sample preparation, optical setup to data processing was learned. Using the optical setup, more experimental characterization on the super-resolution over oblique angles is required at both oil-immersion and water-immersion systems. More assessment on the me-

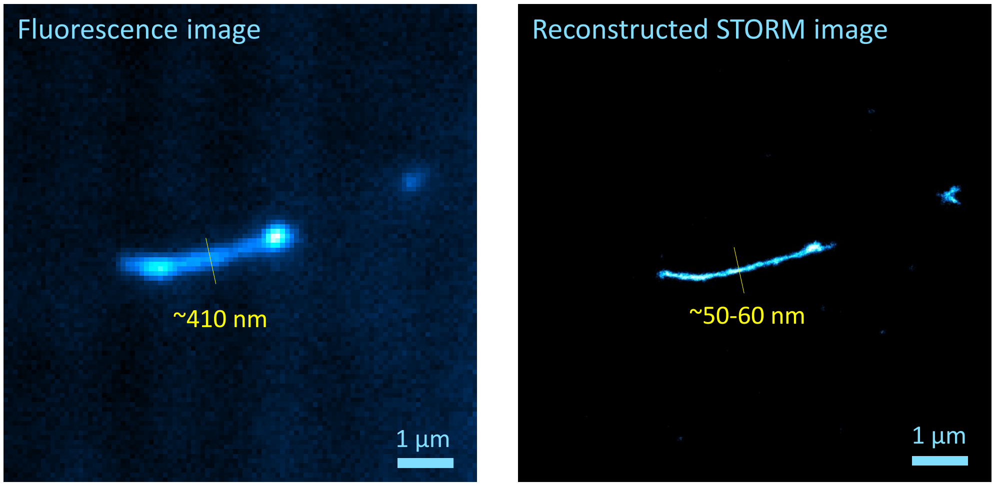

Figure 4.18: Super-resolution test with Si nanowire (40 nm diameter before oxidization) labeled with Alexa Fluor 647. (left) conventional fluorescence image (right) super-resolution image reconstructed in STORM.

chanical drifts of the system would be prerequisite and if necessary proper drift compensation means would have to be implemented prior to an actual use of the setup for super-resolution imaging. A demonstration of deep-tissue super-resolution imaging would complete the feasibility study of the proposed method. Then this tool could be used to answer any interesting biological questions at the whole cell or tissue level.

Chapter 5

Nonparaxial DPC Microscopy

Since the invention of phase contrast optical microscopy by Zernike [63], phase contrast imaging techniques have been revolutionized. Among many approaches developed so far, differential phase contrast (DPC) imaging may be the simplest method which was first proposed in scanning transmission electron microscopy in 1974 [146]. A decade later, optical DPC microscopy was proposed in scanning microscopy with a split detector, which relates phase gradients of a sample to differential intensity [147, 148]. The X-Ray DPC microscopy was proposed in 1897 [149]. Electron DPC microscopy has been advanced towards atomic resolution capability for studies on materials and biological molecules [150]. For optical DPC microscopy, other DPC formats were proposed such as asymmetric illumination contrast [151], tomographic DPC for 3D imaging [152] and wide-field DPC [153]. These days, conventional microscope illumination sources are being replaced by LED sources, or by an LED array with coded illumination capability. The latter enabled many emerging computational imaging techniques [154, 155].

Optical DPC microscopy could be the best candidate for live biological samples, but the existing paraxial DPC image formation theory only covers a lower NA regime. For high resolution DPC microscopy, however, a more advanced DPC imaging theory is necessary for accurate phase retrieval but has not been studied. Motivated by such a situation, this chapter develops nonparaxial scalar DPC theory for high resolution quantitative phase imaging. More specifically, the transmission cross-coefficient (TCC) that is used for phase reconstruction of samples is derived for the high NA DPC system. The formulation considers the apodization in the high NA objective lens, nonparaxial light propagation, and varied layouts of LED array sources with different angular distributions. The nonparaxial TCC derived was numerically compared with the conventional paraxial TCC to investigate major differences. Two possible simplifications of the nonparaxial TCC for practical use in high NA DPC image formation are introduced. Challenges associated with developing a vectorial DPC imaging theory are briefly explained. Also, the experimental verification of the proposed nonparaxial DPC theory as future work is discussed.

5.1 Wide-field DPC system

Schematic of direct DPC microscopy

A wide-field DPC system with a split source is considered as illustrated in Fig. 5.1. The split source may be implemented by a programmable LED array [154]. The existing paraxial DPC theory was derived from the Type 1 scanning DPC system [147], which is a reciprocal equivalent of the wide-field DPC system due to the reciprocity theory of Helmholtz [153]. Similarly, here nonparaxial theory is formulated for the scanning DPC imaging (whose beam path is from left to right) in Fig. 5.1 without losing generality. For the split source/detector, both planar and spherical surfaces are taken into account.

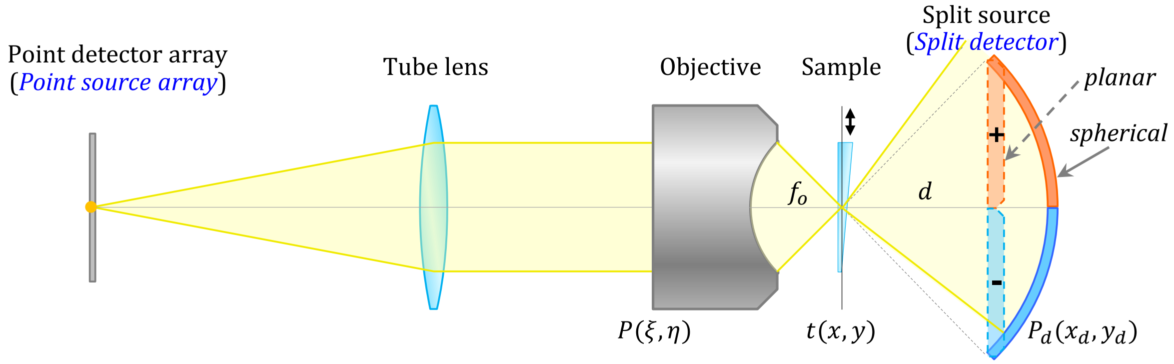

Figure 5.1: Schematic of a wide-field DPC imaging system from a split source to a point detector array (right-to-left). Its reciprocal equivalent is a scanning DPC system from a point source to a split detector (left-to-right). Phase gradients in a sample yields differential intensity. The split source/detector geometry may be planar or spherical. Pupils for an objective lens and the split source/detector are denoted as $P(\xi,\eta)$ and $P_d(x_d,y_d)$, respectively.

In scanning DPC microscopy, an on-axis point source is illuminated on a sample in scanning motion. While the field passes through the sample, it redirects the propagation direction upon the sample's local phase gradient. The split detector senses this laterally shifted field in a differential way for all scanning positions sequentially. Thus a phase gradient of the sample is directly related to the differential intensity in DPC microscopy. The wide-field DPC microscopy works exactly in the reverse way. Each pixel in the point detector array (typically 2D image sensors) senses differential intensity at its conjugated sample location, enabling a direct 2D DPC imaging without scanning.

High NA point spread function

A proper model of the point spread function (PSF), $h(x,y)$ from the point source array to the sample plane in Fig. 5.1 is prerequisite to formulate a DPC imaging equation. This PSF model is obtained by considering light propagation from an on-axis point source to the tube lens and the objective lens in order. Assuming an "isotropic" quasimonochromatic point source collimated by a low NA tube lens (typically $NA_{\text{tube}} < 0.03$), the field amplitude incident to the objective lens would still be almost uniform across the aperture. This assumption conversely means that each pixel of the detector, such as CCD/CMOS cameras, has a uniform angular sensitivity over a few degrees, which is generally true. The field near the geometrical focus of the aplanatic objective lens may be given by the scalar Debye integral (valid at the Fresnel number $N_F \gg 1$) as

$$E(\vec{x}) = -\frac{ik}{2\pi} \oiint_{\Sigma} \sqrt{\cos\theta}\, P(\theta,\phi)\, e^{ik\hat{N}\cdot\vec{x}} \sin\theta\, d\theta d\phi, \tag{5.1}$$

where $P(\theta,\phi)$ is a uniform spherical pupil of the objective lens and $\hat{N}$ is a surface normal unit vector to the pupil surface pointing to the geometrical focus. Transforming the integral geometry from the spherical coordinate to a Cartesian pupil coordinate, Eq. (5.1) is converted to

$$E(\vec{x}) = -\frac{ik}{2\pi f_o^2} \oiint_{\Sigma} \left(1 - \frac{\xi^2+\eta^2}{f_o^2}\right)^{-\frac{1}{4}} P(\xi,\eta)\, e^{-\frac{ik}{f_o}\left(\xi x + \eta y - \sqrt{f_o^2-\xi^2-\eta^2}\, z\right)}\, d\xi d\eta, \tag{5.2}$$

where f_o denotes the focal length of the objective lens. Hence, the field at focus ($z = 0$) is calculated simply by a 2D Fourier transform of an effective pupil function, if the prefactor is neglected, defined as

$$P_{\mathit{eff}}(\xi,\eta) = \left(1 - \frac{\xi^2+\eta^2}{f_o^2}\right)^{-\frac{1}{4}} P(\xi,\eta), \tag{5.3}$$

where $P(\xi,\eta)$ denotes a conventional paraxial pupil function that is a circular function. The effective pupil function includes the apodization factor transformed to the Cartesian coordinate, which has a stronger pupil weighting at the rim of the pupil.

Nonparaxial light propagation

As a high NA objective lens is considered here, the light propagation thereafter from the sample to the detector should be treated nonparaxially. Here a Debye-like approximation is made for two different detector geometries: planar vs. spherical as shown in Fig. 5.1.

For a *planar* detector, as the sample-to-detector distance (d as a constant) is much larger than the wavelength, the scalar field at the detector, $E(\vec{x}_d)$, could be given by the first Rayleigh-Sommerfeld diffraction integral, Eq. (2.8), as

$$E(\vec{x}_d) = -\frac{ik}{2\pi} \oiint_{\Sigma_S} E(\vec{x}) \frac{e^{ikR}}{R} \hat{N}\cdot\hat{R}\, d^2\vec{x}, \tag{5.4}$$

where $E(\vec{x})$ denotes the field right after the sample defined over a planar diffraction geometry Σ_S, $\hat{N} = \vec{z}$ the surface normal vector, and $R = \sqrt{d^2 + (x_d - x)^2 + (y_d - y)^2}$ a distance from a sample position to a detector position.

Then, assuming a much smaller sample than either the split detector dimension or the sample-to-detector distance (in other words, $\vec{x}$ is very close to the origin similar to the Debye approximation), $\vec{R}$ could be approximated as $\vec{R} = \vec{x}_d - \vec{x} \approx \vec{M}(R_d - \hat{M}\cdot\vec{x})$ where $\vec{M} = (x_d/R_d, y_d/R_d, d/R_d)$ is a unit vector from the origin to a detector point with $R_d = \sqrt{d^2 + x_d^2 + y_d^2}$. Alternatively, as the assumption implies $R_d^2 \gg 2(xx_d + yy_d)$, the same result follows simply from the first-order Taylor series approximation of R, *i.e.*, $R \approx R_d - (x_d x + y_d y)/R_d$. Additional approximations, $1/R \approx 1/R_d$ and $\hat{N}\cdot\hat{R} \approx \vec{z}\cdot\vec{M} = d/R_d$, reduce Eq. (5.4) to

$$E(\vec{x}_d) = -\frac{ik}{2\pi}\frac{e^{ikR_d}}{R_d}\frac{d}{R_d}\oiint_{\Sigma_S} E(\vec{x})\,e^{-ik\hat{M}\cdot\vec{x}}\,d^2\vec{x}. \tag{5.5}$$

Both the inverse square law ($1/R_d$) and the inclination factor (d/R_d) in the Fresnel-Huygens principle are properly reflected in the nonparaxial approximations made above. Comparatively, there are neglected in the classical paraxial approximation where $R \approx d + [(x_d - x)^2 + (y_d - y)^2]/(2d^2)$, $1/R \approx 1/d$, and $\hat{N}\cdot\hat{R} \approx 1$.

For a *spherical* detector whose radius is r_d, the similar argument could be made. For a smaller sample (or $\vec{x}$ is very close to the origin), $\vec{R} = \vec{x}_d - \vec{x} \approx \hat{M}(r_d - \hat{M}\cdot\vec{x})$ where $\hat{M} = (\sin\theta_d\cos\phi_d, \sin\theta_d\sin\phi_d, \cos\theta_d)$. Since $\hat{N}\cdot\hat{R} \approx \vec{z}\cdot\hat{M} = \cos\theta_d$, the field arriving at the spherical observation surface is calculated by

$$E(r_d, \theta_d, \phi_d) = -\frac{ik}{2\pi}\frac{e^{ikr_d}}{r_d}\cos\theta_d \oiint_{\Sigma_S} E(\vec{x})\,e^{-ik\hat{M}\cdot\vec{x}}\,d^2\vec{x}. \tag{5.6}$$

The inverse square law vanishes here as the spherical detector maintains almost the equal propagation length. The inclination factor still remains.

LED array source modeling

The LED (light-emitting diode) has an angular emission pattern depending mainly on a shape of the lens encompassing the LED chip. Typically a spherical lens yields an isotropic distribution while a planar lens does a Lambertian pattern. As illustrated in Fig. 5.2, such an emission distribution of the LED source may be modeled as

$$I(\theta, g) = I_S \cos^g\theta, \tag{5.7}$$

where θ represents a polar angle and g determines a type of source. In the schematic of the DPC imaging system under consideration, the g factor could be important in a planar LED array source as all the laterally displaced LEDs illuminate a sample's position with different angular strength. If the system includes a condenser optics thanks to an availability of much more compact LED arrays than now, then the condenser's apodization function would be much more influential than the LED's angular radiation spectrum. On the other hand, a spherical LED array would not be affected by the g factor, because all the LEDs point to the origin in the sample with equal intensity.

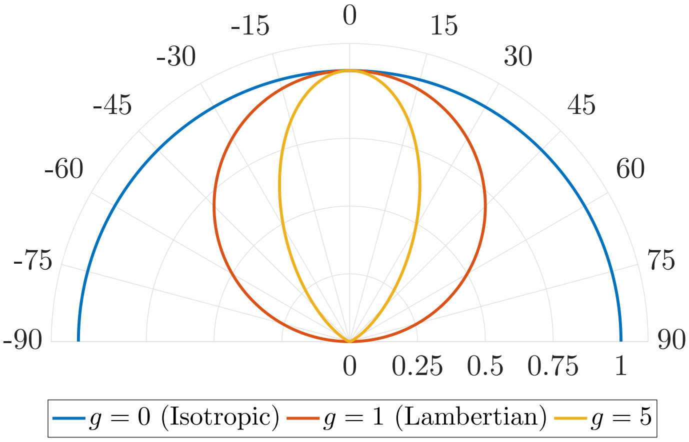

Figure 5.2: Angular radiation patterns of LED sources modeled as $I(\theta, g) = \cos^g \theta$. Isotropic ($g = 0$), Lambertian ($g = 1$).

In addition, each LED could be modeled as a quasi-monochromatic point source, and there would be no spatial coherence between any two LEDs, which means an incoherent point array source.

As a reciprocal detector point of view in the scanning DPC system, similar to the g factor in an LED source, an equivalent g factor that explains angular detection sensitivity could be introduced.

5.2 Nonparaxial DPC image formation with a planar detector

DPC imaging equation

For a scanning position (x_s, y_s) of a thin sample at focus $(z = 0)$ of which transmittance is denoted as $t(x, y)$, the electric field right after the sample is $h(x, y)t(x_s - x, y_s - y)$. Then the nonparaxial diffraction formula, Eq. (5.5), provides the field in the flat detector as

$$E(x_d, y_d) = -\frac{ik}{2\pi} \frac{d e^{ikR_d}}{R_d^2} \oiint_{\Sigma_S} h(x, y)t(x_s - x, y_s - y)\, e^{-\frac{ik}{R_d}(x_d x + y_d y)}\, dxdy \tag{5.8}$$

Taking the LED's angular emission model, Eq. (5.7), into account, detector sensitivity may be expressed as

$$D(x_d, y_d) = \left| \left(\frac{d}{R_d} \right)^{\frac{g}{2}} P_d(x_d, y_d) \right|^2, \tag{5.9}$$

where $P_d(x_d, y_d)$ denotes a detector pupil function (or geometry). In DPC imaging, $|P_d(x_d, y_d)|^2$ is practically a uniform, circular function weighted by a sign function, such as $sgn(x)$ or

$sgn(y)$, for differential detection. Its diameter is often set by a desired partial coherence factor (σ) typically to one or above. For an LED array, a two-dimensional Dirac comb function, $\sum_j \delta_{2D}(\vec{x}_d - \vec{x}_j)$ with each LED located at $\vec{x}_j$, could be multiplied to consider a discrete detection nature of the array.

If the detector is perfectly incoherent (practically true for the LED array), the total detected intensity for a sample location (x_s, y_s) is calculated as

$$I(x_s, y_s) = \oiint \left| E(x_d, y_d) \right|^2 D(x_d, y_d)\, dx_d dy_d. \tag{5.10}$$

In order to derive a transmission cross-coefficient (TCC) described in spatial frequency domain, one may introduce the Fourier representation of the sample and the PSF respectively as

$$t(\vec{x}) = \iint T(\vec{f})\, e^{i2\pi \vec{f}\cdot\vec{x}}\, d^2\vec{f}, \;\; h(\vec{x}) = \frac{1}{i\lambda f_o^2} \iint P_{\mathit{eff}}(\vec{\xi})\, e^{-i\frac{2\pi}{\lambda f_o}\vec{\xi}\cdot\vec{x}}\, d^2\vec{\xi}, \tag{5.11}$$

where $\vec{x} = (x, y)$, $\vec{f} = (f_x, f_y)$, and $\vec{\xi} = (\xi, \eta)$ for compactness. Substituting these two equations to Eq. (5.10) with further mathematical manipulation leads to a DPC intensity equation expressed as

$$I(\vec{x_s}) = \iiiint C(\vec{f_1}; \vec{f_2})\, T(\vec{f_1}) T^*(\vec{f_2})\, e^{i2\pi(\vec{f_1}-\vec{f_2})\cdot\vec{x}_s}\, d^2\vec{f_1}\, d^2\vec{f_2}, \tag{5.12}$$

where $C(\vec{f_1}; \vec{f_2})$ is the four-dimensional TCC (or transfer function) derived as

$$C(\vec{f_1}; \vec{f_2}) = \oiint \frac{d^2}{R_d^4} \Big(\frac{d}{R_d}\Big)^g \Big| P_d(\vec{x}_d) \Big|^2 P_{\mathit{eff}} \Big(-\frac{f_o}{R_d}\vec{x}_d - \lambda f_o \vec{f_1}\Big)\, P^*{}_{\mathit{eff}} \Big(-\frac{f_o}{R_d}\vec{x}_d - \lambda f_o \vec{f_2}\Big)\, d^2\vec{x}_d, \tag{5.13}$$

where $R_d = \sqrt{d^2 + |\vec{x}_d|^2}$ and the effective pupil function of the objective lens is given by Eq. (5.3). In wide-field DPC imaging, the scanning position $\vec{x}_s$ is simply replaced by the object coordinate $\vec{x}$.

Thus, the DPC intensity is determined by a 4D bilinear partially coherent process. Compared to the paraxial TCC governed only by pupils of the objective and the detector, the nonparaxial TCC includes three additional factors. These are $\big(1 - |\vec{x}_d / R_d + \lambda \vec{f}|^2\big)^{-1/4}$, which is the apodization factor in high NA aplanatic objective, d^2/R_d^4, which comes from nonparaxial wave propagation from the sample to the detector, where the inverse square law of intensity and the inclination factor in light diffraction are no longer negligible, and $(d/R_d)^g$, which is due to the angular dependence of detector responses as modeled.

Normalizing the pupils and spatial frequencies in the TCC

It is often convenient to have TCC defined in a normalized pupil as $\vec{\xi'} = \vec{\xi}/a$ (where a is a pupil radius) and a normalized spatial frequency as $\vec{m} = \vec{f}/\big(\frac{NA}{\lambda}\big)$. To do so, one may relate the detector coordinate to the objective pupil coordinate by

$$\frac{\vec{x}_d}{R_d} = \frac{a}{f_o}\vec{\xi'}. \tag{5.14}$$

The Jacobian, $J(\vec{\xi'})$, associated with such a change of variables (or a coordinate transformation) is $a^2 R_d^4/(f_o^2 d^2)$, thereby

$$\delta^2 \vec{x}_d = \left(\frac{a}{f_o}\right)^2 \frac{R_d^4}{d^2} \delta^2 \vec{\xi'}. \tag{5.15}$$

Also, plugging Eq. (5.14) to $R_d = \sqrt{d^2 + |\vec{x}_d|^2}$ yields $R_d^{-1} = d^{-1}\sqrt{1-(a/f_o)^2|\vec{\xi'}|^2}$, where $a/f_o = NA$ for an aplanatic objective lens. From all of these relations, one could convert Eq. (5.13), as a 2D integral over the normalized objective pupil coordinate, to

$$\begin{aligned} C(\vec{m}_1;\vec{m}_2) = NA^2 \oiint \Big(1-NA^2|\vec{\xi'}|^2\Big)^{\frac{g}{2}} \left|P_d\big(\vec{x}_d(\vec{\xi'})\big)\right|^2 \times \\ P_{\mathit{eff}}\big(-a(\vec{\xi'}+\vec{m}_1)\big)\, P^*_{\mathit{eff}}\big(-a(\vec{\xi'}+\vec{m}_2)\big)\, d^2\vec{\xi'}, \end{aligned} \tag{5.16}$$

where $\vec{x}_d(\vec{\xi'}) = \vec{\xi'} NAd/\sqrt{1-NA^2|\vec{\xi'}|^2}$. The split detector can be assumed to be circular for a practical reason with a radius of b. The partial coherent factor, a detection NA divided by an objective NA, could then be defined as $\sigma = (b/\sqrt{d^2+b^2})/NA$. One can show that $|\vec{x}_d| = b \longmapsto |\vec{\xi'}| = \sigma$, implying that the circular detector boundary (radius b) in the $\vec{x}_d$ coordinate is mapped into a circular boundary (radius σ) in the transformed $\vec{\xi'}$ coordinate. Also, as $\left|P_d\big(\vec{x}_d\big)\right|^2$ is a sign function (two semicircles with 1 and -1), the mapped $\left|P_d\big(\vec{\xi'}\big)\right|^2$ is also the same sign function. Hence, it may be simplified as

$$\left|P_d\big(\vec{x}_d(\vec{\xi'})\big)\right|^2 \equiv \left|P_d\Big(\frac{\vec{\xi'} NAd}{\sqrt{1-NA^2|\vec{\xi'}|^2}}\Big)\right|^2 = \left|P_d\Big(\frac{b}{\sigma}\vec{\xi'}\Big)\right|^2. \tag{5.17}$$

For the rotationally symmetric objective pupil, *i.e.*, $P(\vec{\xi'}) = P(-\vec{\xi'})$, the TCC has a form of

$$C(\vec{m}_1;\vec{m}_2) = NA^2 \oiint \Big(1-NA^2|\vec{\xi'}|^2\Big)^{\frac{g}{2}} \left|P_{d,n}\Big(\frac{\vec{\xi'}}{\sigma}\Big)\right|^2 P_{\mathit{eff},n}(\vec{\xi'}+\vec{m}_1) P^*_{\mathit{eff},n}(\vec{\xi'}+\vec{m}_2)\, d^2\vec{\xi'}, \tag{5.18}$$

where the subscript of ‘$,n$’ in each pupil function means the normalized pupil to the unit circle. As discussed in Section 2.3, the TCC is geometrically an overlap of three pupils. Unlike the paraxial TCC constructed from uniform pupils, the nonparaxial TCC is from weighted pupils. The sensitivity of the detector pupil radially decreases due to $\big(1-NA^2|\vec{\xi'}|^2\big)^{g/2}$, while the objective pupil has a radially increasing weighting as $\big(1-NA^2|\vec{\xi'}|^2\big)^{-1/4}$. As expected, the derived TCC shows a dependence on NA, and converges to the paraxial TCC when NA approaches to zero (if the prefactor of NA^2 is neglected). Strictly speaking, the paraxial TCC referred here was derived from other DPC imaging schematic comprising a collector lens between the sample and the detector (or reciprocally a condenser lens between the source and the sample) [156]. This collector lens cancels out a quadratic phase term from the Fresnel diffraction integral in the sample plane, thus yielding the paraxial TCC as such. However, as the quadratic phase term can be neglected over smaller FOV near the optical aixs, the identical paraxial TCC could still be used in the current DPC schematic for comparison. If an isotropic detector ($g=0$) is used, or reciprocally an isotropic LED source in wide-field DPC imaging, no detector weighting results. The TCC represented in the normalized objective pupil coordinate from Eq. (5.14) does not explicitly show the contribution of nonparaxial wave propagation.

In DPC imaging, $C(\vec{0};\vec{0})=0$ due to its differential nature, and thus it is not clear at which spatial frequency to normalize the TCC. Alternatively, a bright-field TCC value at the zero spatial frequency, $C_{\mathrm{BF}}(\vec{0};\vec{0})$ with uniform detector sensitivity (not differential), could be used to obtain the normalized TCC as

$$C_N(\vec{m}_1;\vec{m}_2) = \frac{1}{C_{\mathrm{BF}}(\vec{0};\vec{0})} \oiint \left(1-NA^2|\vec{\xi'}|^2\right)^{\frac{g}{2}} \left|P_{d,n}\left(\frac{\vec{\xi'}}{\sigma}\right)\right|^2 P_{\textit{eff},n}(\vec{\xi'}+\vec{m}_1)\,{P^*}_{\textit{eff},n}(\vec{\xi'}+\vec{m}_2)\,d^2\vec{\xi'}, \tag{5.19}$$

where the normalization factor is analytically derived as

$$C_{\mathrm{BF}}(\vec{0};\vec{0}) = \begin{cases} 2\pi\,\dfrac{1-(1-NA^2)^{\frac{g+1}{2}}}{(g+1)}, & \sigma \geq 1 \\ 2\pi\,\dfrac{1-(1-\sigma^2NA^2)^{\frac{g+1}{2}}}{(g+1)}, & \sigma < 1 \end{cases}. \tag{5.20}$$

The same normalization factor can be found directly from Eq. (5.13), and thus Eq. (5.20) can be shared for normalizing both $C(\vec{m}_1;\vec{m}_2)$ and $C(\vec{f}_1;\vec{f}_2)$.

If the point array detector as a Dirac comb is considered, the TCC is calculated by

$$C(\vec{m}_1;\vec{m}_2) = NA^2 \sum_j \left(1-NA^2|\vec{\xi'_j}|^2\right)^{\frac{g}{2}} \left|P_{d,n}\left(\frac{\vec{\xi'_j}}{\sigma}\right)\right|^2 P_{\textit{eff},n}\big(\vec{\xi'_j}+\vec{m}_1\big)\,{P^*}_{\textit{eff},n}\big(\vec{\xi'_j}+\vec{m}_2\big), \tag{5.21}$$

where $\vec{\xi'_j} = \frac{\vec{x}_j}{(NA\sqrt{d^2+|\vec{x}_j|^2})}$ denotes the j^{th} location of the point detector.

5.3 Nonparaxial DPC image formation with a spherical detector

DPC imaging equation

For a spherical detector/source, the nonparaxial diffraction integral, Eq. (5.6), provides the electric field on the spherical detector as

$$E(r_d,\theta_d,\phi_d) = -\frac{ik}{2\pi}\frac{e^{ikr_d}}{r_d}\cos\theta_d \oiint_{\Sigma_S} h(\vec{x})\,t(\vec{x}_s-\vec{x})\,e^{-ik\hat{M}\cdot\vec{x}}\,d^2\vec{x}, \tag{5.22}$$

where $\vec{x}_s$ is a scanning position of the sample. No angular selectivity may exist for the dome geometry, and thus the detector sensitivity would be simply $D(\theta_d,\phi_d) = \left|P_d(\theta_d,\phi_d)\right|^2$, where

$P_d(\theta_d, \phi_d)$ describes a detector pupil geometry in spherical coordinate. Then assuming the perfectly incoherent detector (again practically true for the LED array), the total detected intensity is evaluated by

$$I(\vec{x}_s) = \oiint \left|E(r_d, \theta_d, \phi_d)\right|^2 D(\theta_d, \phi_d)\, r_d^2\, d\Omega_d, \tag{5.23}$$

where $d\Omega_d = \sin\theta_d d\theta_d d\phi_d$. By plugging Eq. (5.11) with $d\Omega_d = d^2\vec{x}_d/(r_d^2 \cos\theta_d)$ here, the TCC with a spherical detector can be finally derived as

$$C(\vec{f_1}; \vec{f_2}) = \frac{1}{r_d^2} \oiint \sqrt{1 - \frac{|\vec{x}_d|^2}{r_d^2}} \left|P_d(\vec{x}_d)\right|^2 P_{\mathit{eff}}\Big(-\frac{f_o}{r_d}\vec{x}_d - \lambda f_o \vec{f_1}\Big) P^*{}_{\mathit{eff}}\Big(-\frac{f_o}{r_d}\vec{x}_d - \lambda f_o \vec{f_2}\Big)\, d^2\vec{x}_d, \tag{5.24}$$

where $\vec{x}_d = (x_d, y_d)$ is the z-projected planar detector coordinate. The detector sensitivity stays unchanged upon its projection from $P_d(\theta_d, \phi_d)$ to $P_d(\vec{x}_d)$.

Normalizing the pupils and spatial frequencies in the TCC

To transform the integral domain of the TCC into the objective pupil space, one can relate

$$\frac{a\vec{\xi'}}{f_o} = \frac{\vec{x}_d}{r_d}, \tag{5.25}$$

with the constant Jacobian of $J(\vec{\xi'}) = a^2 r_d^2/f_o^2$. Normalizing the objective pupil as $\vec{\xi'} = \vec{\xi}/a$ and the spatial frequency as $\vec{m} = \vec{f}/(\frac{NA}{\lambda})$, the TCC can be expressed as

$$\begin{aligned} C(\vec{m}_1; \vec{m}_2) = NA^2 \oiint \Big(1 - NA^2|\vec{\xi'}|^2\Big)^{\frac{1}{2}} \left|P_d\big(r_d NA\, \vec{\xi'}\big)\right|^2 \times \\ P_{\mathit{eff}}\left(-a(\vec{\xi'} + \vec{m}_1)\right) P^*{}_{\mathit{eff}}\left(-a(\vec{\xi'} + \vec{m}_2)\right) d^2\vec{\xi'}, \end{aligned} \tag{5.26}$$

where $NA = a/f_o$ for the aplanatic objective lens. For a circular split detector (radius: b) with a partial coherence factor $\sigma = (b/r_d)/NA$ and for a rotationally symmetric objective pupil $P(-\vec{\xi'}) = P(\vec{\xi'})$, the TCC is finally obtained as

$$C(\vec{m}_1; \vec{m}_2) = NA^2 \oiint \Big(1 - NA^2|\vec{\xi'}|^2\Big)^{\frac{1}{2}} \left|P_{d,n}\Big(\frac{\vec{\xi'}}{\sigma}\Big)\right|^2 P_{\mathit{eff},n}(\vec{\xi'} + \vec{m}_1) P^*{}_{\mathit{eff},n}(\vec{\xi'} + \vec{m}_2)\, d^2\vec{\xi'}, \tag{5.27}$$

where the subscript '$,n$' means the normalized pupil to the unit circle. Here, the factor of $\big(1 - NA^2|\vec{\xi'}|^2\big)$ is attributed to the inclination factor associated with the sample-to-detector wave propagation. This weighting factor appears to be the only difference between the planar and spherical geometries. The derived nonparaxial TCC also converges to the paraxial TCC as NA goes to zero (if the prefactor of NA^2 is neglected).

The TCC could be normalized by the bright-field TCC value at the zero frequency, $C_{\mathrm{BF}}(\vec{0}; \vec{0})$, whose value is already found in Eq. (5.20) with $g = 1$. Also, considering the array detector (or reciprocal LED array), the TCC similar to Eq. (5.21) can be obtained with the j^{th} array location at $\vec{\xi'_j} = \frac{\vec{x}_j}{r_d NA}$.

5.4 Simplification of DPC image formation

It can be immediately found from Eq. (5.12) that 2D DPC imaging is a four-dimensional process which is too complicated to practically handle. Two common simplifications [147, 148] made to samples could reduce such a 4D process into 2D, which are briefly introduced here.

Weak object approximation

The weak object approximation assumes an object transmittance as $t(\vec{x}) = 1 + t_w(\vec{x})$ where $|t_w(\vec{x})| \ll 1$. The $t_w(\vec{x})$ can be real or imaginary or both, upon amplitude or phase or combined objects. By substituting its Fourier transform, $T(\vec{f})=\delta(\vec{f})+T_w(\vec{f})$, to Eq. (5.12), the DPC intensity is expressed as

$$\begin{aligned} I(\vec{x}) =& C(\vec{0};\vec{0}) + \iint C(\vec{f_1};\vec{0})T_w(\vec{f_1})e^{i2\pi\vec{f_1}\cdot\vec{x}}d^2\vec{f_1} + \iint C(\vec{0};\vec{f_2})T_w^*(\vec{f_2})e^{-i2\pi\vec{f_2}\cdot\vec{x}}d^2\vec{f_2} \\ &+ \iiiint C(\vec{f_1};\vec{f_2})T_w(\vec{f_1})T_w^*(\vec{f_2})e^{i2\pi(\vec{f_1}-\vec{f_2})\cdot\vec{x}}\, d^2\vec{f_1}d^2\vec{f_2}. \end{aligned} \tag{5.28}$$

Since intensity is a real quantity (or measurable), *i.e.*, $I(\vec{x}) = I^*(\vec{x})$, one can find from Eq. (5.12) that $C(\vec{f_1};\vec{f_2}) = C^*(\vec{f_2};\vec{f_1})$. Also assured from the weak object: $|T_w| \gg |T_w\, T_w^*|$ (negligible cross-product term), the above equation could be approximated as

$$I(\vec{x}) \approx C(\vec{0};\vec{0}) + 2\,\mathrm{Re}\Big\{ \iint C(\vec{f};\vec{0})\, T_w(\vec{f})\, e^{i2\pi\vec{f}\cdot\vec{x}}d^2\vec{f}\Big\}. \tag{5.29}$$

In DPC imaging, $C(\vec{0};\vec{0}) = 0$ due to the differential nature. Now 2D image formation is reduced to a two-dimensional *linear* process, where image intensity is directly linked to an inverse Fourier transform of the product of the weak object frequency spectrum and the 2D weak object transfer function (WOTF): $C(\vec{f};\vec{0})$.

Typically the DPC intensity is defined in a normalized format (divided by its bright field intensity) as

$$I_{\mathrm{DPC}}(\vec{x}) = \frac{I_T(\vec{x})-I_B(\vec{x})}{I_T(\vec{x})+I_B(\vec{x})}, \tag{5.30}$$

where the subscripts ‘T’ and ‘B’ indicate intensity detected from the top and bottom of the split detectors in Fig. 5.1. By plugging Eq. (5.29) to here, one can obtain

$$\begin{aligned} I_{\mathrm{DPC,TB}}(\vec{x}) &= \frac{2\,\mathrm{Re}\big\{ \iint C_{\mathrm{TB}}(\vec{f};\vec{0})\, T_w(\vec{f})\, e^{i2\pi\vec{f}\cdot\vec{x}}d^2\vec{f}\big\}}{C_{\mathrm{BF}}(\vec{0};\vec{0}) + 2\,\mathrm{Re}\big\{ \iint C_{\mathrm{BF}}(\vec{f};\vec{0})\, T_w(\vec{f})\, e^{i2\pi\vec{f}\cdot\vec{x}}d^2\vec{f}\big\}} \\ &\approx 2\,\mathrm{Re}\Big\{ \iint C_{\mathrm{N,TB}}(\vec{f};\vec{0})\, T_w(\vec{f})\, e^{i2\pi\vec{f}\cdot\vec{x}}d^2\vec{f}\Big\}, \end{aligned} \tag{5.31}$$

where $C_{\mathrm{N,TB}}(\vec{f};\vec{0}) = C_{\mathrm{TB}}(\vec{f};\vec{0})/C_{\mathrm{BF}}(\vec{0};\vec{0})$, as introduced in Eq. (5.19), is a normalized 2D WOTF in the ‘TB’ configuration. Once the DPC image is acquired with the known WOTF, the original object information can be inversely calculated. However, $I_{\mathrm{DPC,TB}}(\vec{x})$ alone fails to measure major horizontal frequency contents (f_x) of the object, and thus in practice $I_{\mathrm{DPC,LR}}(\vec{x})$ (or further DPC images along other azimuthal orientations) is also measured for accurate phase imaging [73]. In computational phase retrieval, these multi-orientation 2D WOTFs are incorporated in the algorithms.

The weak object approximation, $t(\vec{x}) = e^{i\phi(\vec{x})} \approx 1 + i\phi(\vec{x})$, in quantitative phase imaging may have less than 5% error if $|\phi(\vec{x})| \leq 0.355$ radian.

Slowly varying phase gradient

If an object's phase profile changes slower than imaging resolution (the PSF) (as well as pixel resolution), the object could be approximated as $t(\vec{x}) = e^{i\nabla\phi(\vec{x})\cdot\vec{x}}$. The $\nabla\phi(\vec{x})$ is a local phase gradient which corresponds to a particular spatial frequency as $T(\vec{f}) = \delta(\vec{f} - \frac{\nabla\phi(\vec{x})}{2\pi})$, thereby reducing the DPC imaging equation, Eq. (5.12), merely to

$$I(\vec{x}) = C\Big(\frac{\nabla\phi(\vec{x})}{2\pi}; \frac{\nabla\phi(\vec{x})}{2\pi}\Big), \tag{5.32}$$

where $C\big(\frac{\nabla\phi(\vec{x})}{2\pi}; \frac{\nabla\phi(\vec{x})}{2\pi}\big)$ is called a 2D phase gradient transfer function (PGTF). This approximation also reduces the 4D imaging process into 2D, but it is different from typical linear imaging. Instead, the 2D PGTF itself directly connects the DPC intensity measured with knowledge on a sample's local phase gradients.

From the typical DPC intensity definition, Eq. (5.30), it can be shown

$$I_{\mathrm{DPC,TB}}(\vec{x}) = \frac{C_{\mathrm{TB}}\big(\frac{\nabla\phi(\vec{x})}{2\pi}; \frac{\nabla\phi(\vec{x})}{2\pi}\big)}{C_{\mathrm{BF}}\big(\frac{\nabla\phi(\vec{x})}{2\pi}; \frac{\nabla\phi(\vec{x})}{2\pi}\big)}, \tag{5.33}$$

where $C_{\mathrm{BF}}(\vec{f_1}; \vec{f_2})$ is a bright-field TCC in Eq. (5.13) with uniform detector sensitivity. The normalized 2D PGTF is thus defined by $C_{\mathrm{N,TB}}(\vec{f}; \vec{f}) = C_{\mathrm{TB}}(\vec{f}; \vec{f})/C_{\mathrm{BF}}(\vec{f}; \vec{f})$.

For 1D DPC imaging, for example, where a sample contains only f_y frequency contents, the 1D PGTF, $C_{\mathrm{N,TB}}(0, \frac{\nabla\phi_y}{2\pi}; 0, \frac{\nabla\phi_y}{2\pi})$, plays as a lookup table which directly returns the local phase gradient details of the sample. From this, a (quantitative) phase profile of the sample is then numerically reconstructed directly from $\phi(y) = \int_0^y \nabla\phi(y')\cdot dy'$ or from more robust least square algorithms [157]. However, it should be noted that in 2D DPC imaging the 2D PGTF may not work as a simple lookup table anymore. This is mainly because although $I_{\mathrm{DPC,TB}}$ is primarily a measure of vertical phase gradients, it also contains subsidiary horizontal phase gradient information coupled together, which can be implied from the 2D PGTF equation. Thus the vertical phase gradients can not be accurately extracted from the 'TB' measurement alone. Together with the 'LR' measurement, a proper gradient search algorithm may be necessary to successfully decouple horizontal/vertical phase gradients from both the 2D LR and TB PGTFs. Moreover, if the total number of LEDs in the array used for DPC imaging is insufficient, the TCC shows staircase patterns [73]. This adds a uncertainty in determining the local phase gradient, which hence requires an attention in building an optical setup compatible with the PGTF approach.

5.5 Numerical study: paraxial *vs.* nonparaxial TCC

Numerical simulations were conducted to compare the nonparaxial TCC with the paraxial TCC for the wide-field DPC imaging system with a planar 'L(left)/R(right)' split source at $\lambda = 0.5\,\mu$m. The partial coherence factor was fixed to one. The results for a spherical split source would be the same with those obtained here with $g = 1$. The array nature was not accounted.

The normalized 2D WOTF, $C_{\mathrm{N,LR}}(\vec{m};\vec{0})$, was evaluated in Fig. 5.3, together with its horizontal slice ($m_y = 0$) in Fig. 5.4. The TCC is anti-symmetric about $m_x = 0$ (y-axis) due to the source's LR asymmetry. The maximum TCC occurs near $m_x = \pm 1$ where the displaced objective pupil has a maximum overlap with only one of the half source/detector. In this case, less than 50% of the shifted objective pupil area falls within the semicircle, and thus a maximum TCC value is below 0.5 (more accurately around 0.4). For an isotropic source ($g = 1$), the nonparaxial effects that arise only from the objective's apodization seem to lower the TCC's maximum. The stronger weighting near the rim of the objective pupils reduces an effective overlap for $0 < m_x < 1.2$ compared with the paraxial overlap, while helps to increase an effective overlap at $m_x > 1.2$. For a Lambertian source ($g = 1$), the angularly decreasing strength in source/detector sensitivity together with the objective's apodization yields lower TCC values over $m_x < 0.9$ than the paraxial WOTF. The maximum TCC, however, stays almost fixed at around 0.408 in any NA regime. For a source emission model with $g \geq 2$, the nonparaxial WOTF begins to deviate from the paraxial WOTF more obviously as NA increases. Also, it results in a negative WOTF value (or WOTF

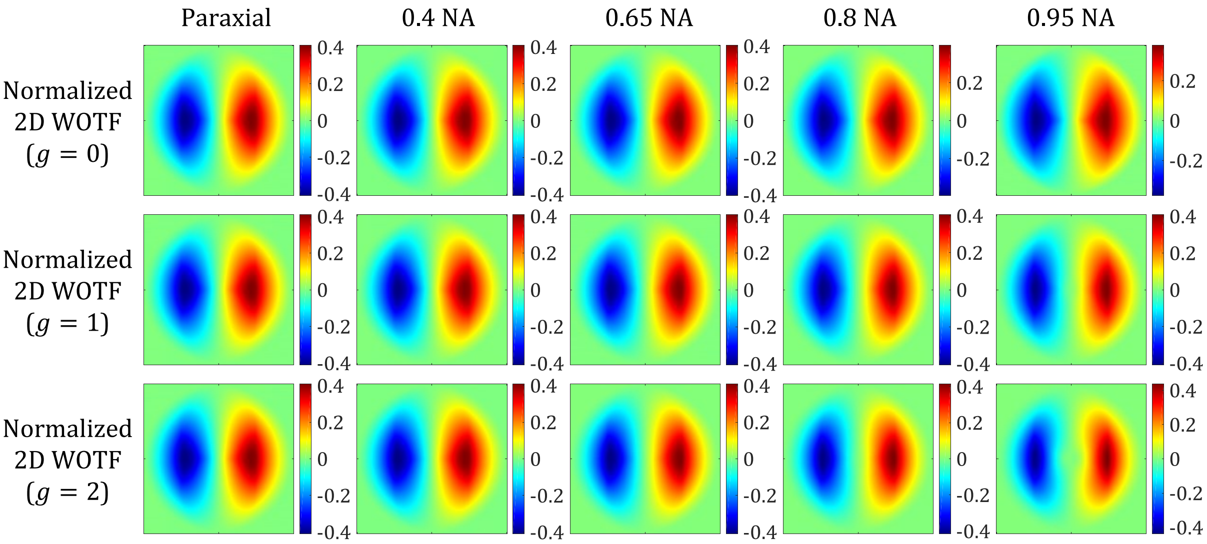

Figure 5.3: Normalized 2D nonparaxial WOTF in 'LR' DPC imaging with different g factors. The axis label omitted is the normalized spatial frequency $\vec{m}$ over [-2, 2], with $\lambda = 0.5\,\mu$m. The paraxial WOTFs are shown in the first column for comparison.

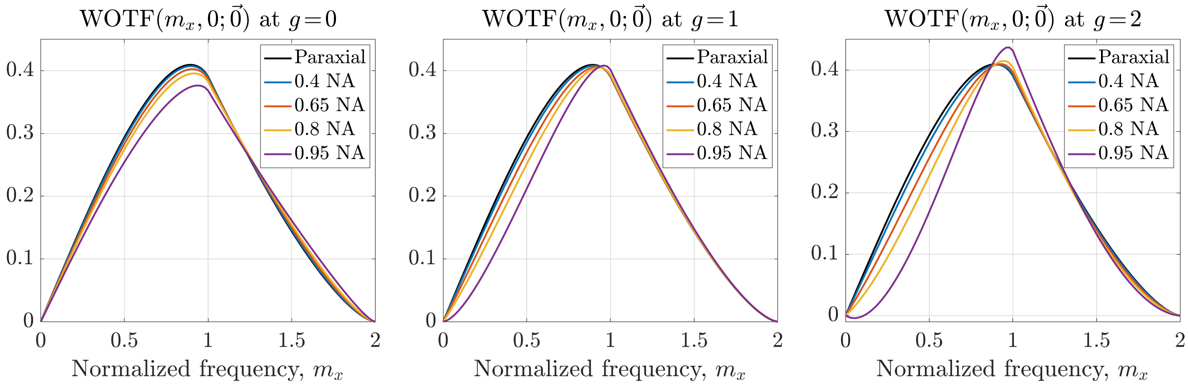

Figure 5.4: Cross-sections of the normalized 2D nonparaxial WOTF in 'LR' DPC imaging ($\lambda = 0.5\,\mu$m) with varied g factors. A negative WOTF value (*i.e.*, WOTF reversal) near $m_x = 0.05$ appears at $g=2$.

reversal) around a normalized spatial frequency of 0.05 (the physical explanation follows later.) Overall, the paraxial WOTF appears to be still a good model for NA below 0.4 in optical DPC imaging.

Next, the normalized 2D PGTF, $C_{\mathrm{N,LR}}(\vec{m}; \vec{m})$, was calculated (see Fig. 5.5). The PGTF is also anti-symmetric and saturates to either -1 or 1 when the objective pupil is completely

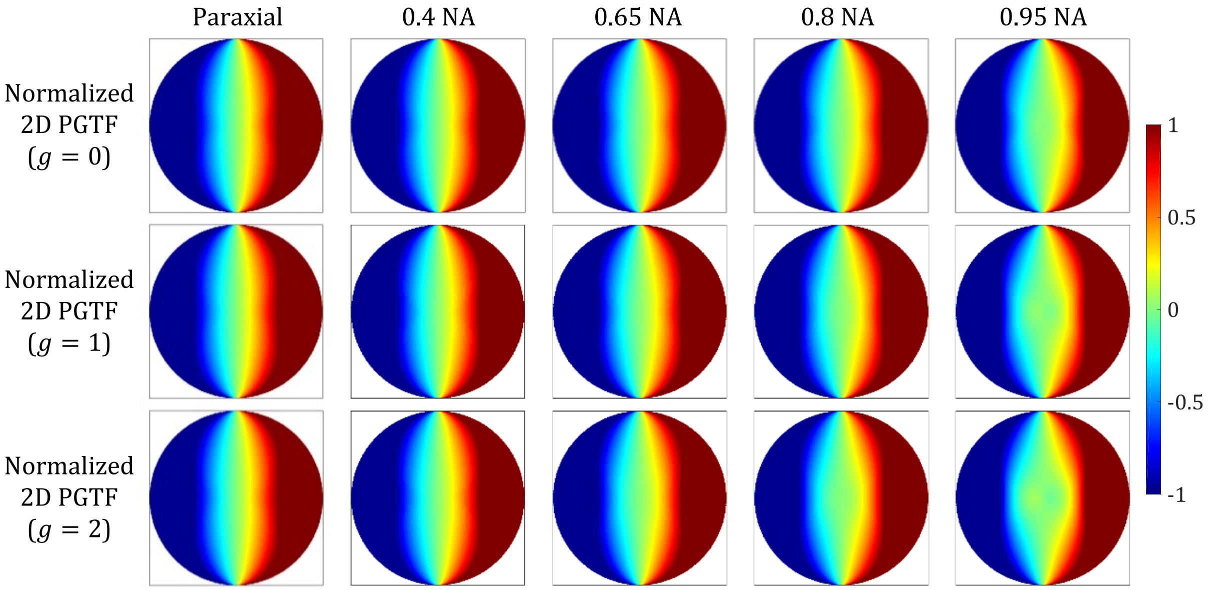

Figure 5.5: The normalized 2D nonparaxial PGTF in 'LR' DPC imaging with different g factors. The axis label omitted is the normalized spatial frequency $\vec{m}$ over [-2, 2], with $\lambda = 0.5\,\mu$m. The paraxial PGTFs are shown in the first column for comparison.

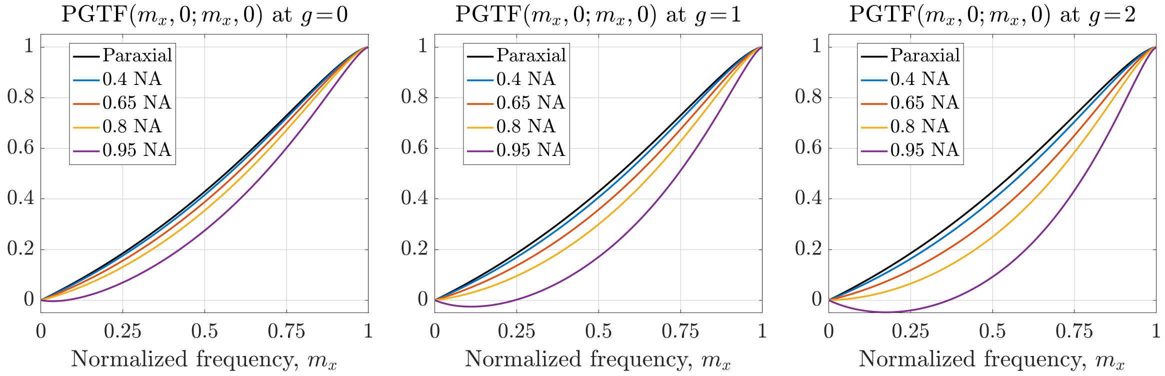

Figure 5.6: Cross-sections of the normalized 2D nonparaxial PGTF in 'LR' DPC imaging ($\lambda = 0.5\,\mu$m) with different g factors. A PGTF reversal is predicted at higher NA.

shifted towards one of the source/detector's semicircles. Thus such a clipping occurs at the normalized frequency of around one, and any phase gradient greater than that in the sample is not captured by the DPC imaging system. The normalized PGTF may only be defined within the $|\vec{m}| \leq 2$ circle, where the denominator of the PGTF (the TCC value for incoherent bright-field imaging) is non-zero. As NA increases, the PGTF deviates from the paraxial PGTF more apparently especially at higher g factors. The horizontal cross-section at $m_y = 0$ is plotted in Fig. 5.6, which shows the PGTF saturation occurring exactly at $m_x = \pm 1$. Also, a PGTF reversal is predicted in high NA DPC imaging caused primarily by the objective apodization. To see the reversal in geometrical point of view, the pupils for the PGTF(0.2,0;0,0.2) at 0.95 NA with $g=2$ were examined as shown in Fig. 5.7. The net geometrical overlap for the positive detector sensitivity area (the left semicircle) at the

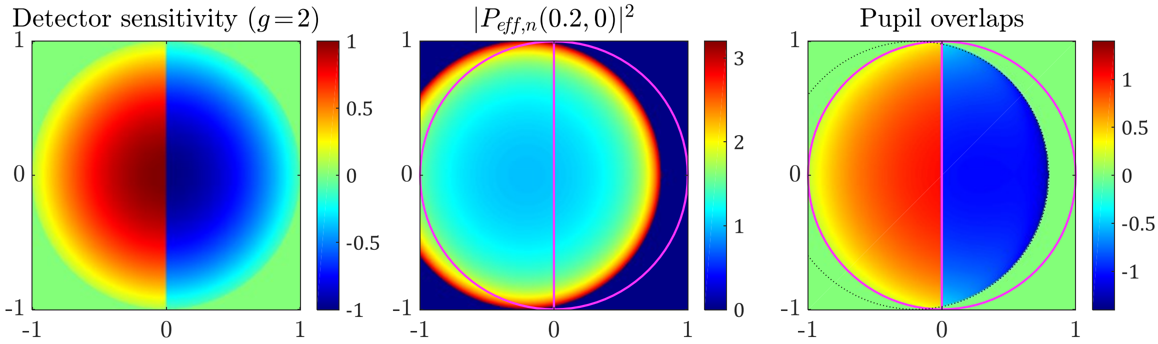

Figure 5.7: Mechanism of the PGTF reversal in nonparaxial DPC imaging. Effective pupils and their overlap in a unity coordinate ($g = 2, NA = 0.95$). The geometrical overlap is larger on the left positive semicircle, but due to the nonuniform objective pupil weighting the effective overlap on the right negative semicircle is rather larger, leading to negative differential intensity (a negative TCC value).

-0.2 shifted objective pupils is certainly larger than that for the right semicircle. Yet, the stronger rims of the two apodized objective pupils selectively influence the negative detector sensitivity area (right semicircle), yielding a negative differential intensity that is a negative TCC value. The PGTF is defined with two identically shifted objective pupils compared with only one objective pupil shifted in the WOTF, and thus undergoes a more severe reversal. The TCC reversal at higher NA may cause problems in the slowly varying phase gradient approximation. The reversal near the zero spatial frequency would make local phase gradients indeterminate (as the identical TCC intensity could result from different phase gradients). More advanced algorithm would be required to make the gradient search protocol determinate probably by incorporating the additional knowledge on phase gradients in the neighborhood of the indeterminate point.

As the g factor increases, the non-uniform detector sensitivity falls off much faster, which decreases an effective detector dimension. The effective partial coherent factor, σ, drops accordingly. It was found that the TCC at higher g factor with $\sigma = 1$ resembles the TCC at lower g factor with $\sigma < 1$ (although the results are not included here).

Besides, as shortly discussed in the previous section, strictly speaking the 2D PGTF may not play as a lookup table because the 'LR' measurement includes not only horizontal but also vertical phase gradient information. The cross-sections of the 2D PGTF in Fig. 5.5 were examined as shown in Fig. 5.8. In the paraxial PGTF (left plot), the vertical phase gradients smaller than 0.5 (in terms of a normalized frequency m_y) induce minor TCC modifications ($< 10\%$) in the measurement of horizontal phase gradients. However, in the nonparaxial PGTF (for example, at $NA = 0.8$, $g = 1$ on the right plot), the contribution of the vertical phase gradient on the measurement of the horizontal phase gradients is significant. This is especially when the y-phase gradient at the point of measurement is larger than the x-phase gradient to be measured.

5.6 Further discussion

Compared to the paraxial DPC theory, the nonparaxial theory formulated here together with the source's angular emission model certainly predicts a different TCC. It is expected that the proposed nonparaxial DPC model could be used for more accurate optical quantitative phase imaging. Yet, it should be mentioned that this scalar model is still incomplete because it does not consider the vectorial nature of light. Considering a light-sample interaction to accurately trace changes in light polarization is nontrivial. Perhaps by assuming that the dipoles consisting of the object in the first Born approximation orient in parallel to the input electric field, the vectorial pupils for each point of an incoherent source could be defined and used to construct a vectorial TCC.

In order to experimentally corroborate the nonparaxial DPC theory, a proper phase sample has to be carefully chosen or prepared. Unfortunately there are no common standard phase samples (like standard USAF resolution charts in amplitude imaging). There may be

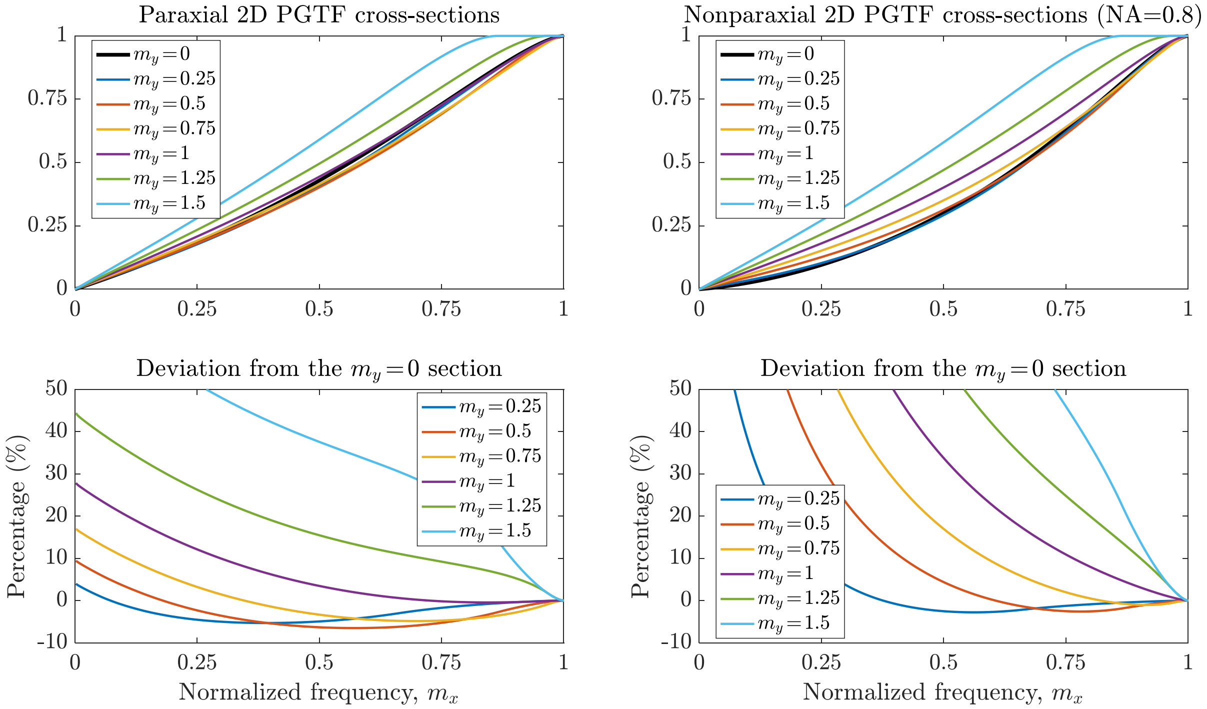

Figure 5.8: Horizontal cross-sections of the 2D 'LR' PGTF at different m_y. (left) the paraxial 2D PGTF (right) the nonparaxial PGTF at 0.8 NA ($g=1$). The 'LR' PGTF value is also influenced by an amount of m_y (vertical phase gradient).

two approaches to prove the nonparaxial TCC given that a test sample with known phase profiles can be well approximated as either a weak object or a slowly varying phase object.

In the former case, a thin micro-lens could be tried. For example, there is a commercial quartz microlens array (MLA150-7AR, Thorlabs Inc.) with a sag of 0.87 μm (over a 150 μm lens diameter) which is as thin as the typical sub-μm depth of field in high NA objective lenses. For the known phase profile of the lens, DPC intensity can be theoretically calculated using Eq. (5.31) and can be compared with experimental DPC images. With this lens, the weak object approximation would be valid within a FOV of roughly 40 μm around the lens center. The FOV could be further extended by putting an immersion oil between the top surface of the lens and a coverslip, which then requires an objective lens with a coverglass correction. Alternatively, a glass phase object with any weak phase profiles could be fabricated by focused ion beam (FIB) as done in [158]. This approach, however, may also have its own challenges because the maximum object height allowed as a weak object is only around 70 nm, which is probably too thin to fabricate a desired phase pattern. On the other hand, many biological samples are good phase objects but can be challenging here too, because even thin cells typically are not good weak objects let alone their unknown phases.

If the PGTF approach is chosen as a proof, a good phase gradient object may be even harder to obtain for high NA DPC imaging. Previous studies have used an optical fiber or a polystyrene micro-bead, immersed in liquid, as a known phase object whose phase gradient continuously changes across the diameter [153, 155]. In this case, the effective phase profile of the circular object (radius: R) may be

$$\phi(x) = \frac{2\pi}{\lambda} 2\Delta n \sqrt{R^2 - x^2}, \tag{5.34}$$

where Δn is the refractive index difference between the object and the surrounding medium. Then the normalized phase gradient across the object may be given by

$$m_x = -\frac{2\Delta n}{NA} \frac{x}{\sqrt{R^2 - x^2}}. \tag{5.35}$$

This could be a good phase gradient object that covers all spatial frequency range of interest at smaller NA, but a careful examination is needed for the validity in higher NA. First of all, the bead diameter is at least a few microns which is thicker than the sub-μm DOF of the high NA objective lens. The theoretical PGTF itself keeps unchanged throughout focus, but the effective phase profile for such thick objects may not be as simple as Eq. (5.34). This may distort the PGTF measured. Also, any significant index-mismatch of either the bead or the surrounding medium with respect to the coverslip index may induce significant optical aberrations at high NA, making an accurate PGTF measurement challenging. Even the thickness of the coverslip can be very critical. A sub-μm bead may be available instead, but it will be too small to assume as a slowly varying phase object. On the other hand, the micro-lens mentioned above is thin enough, but the phase gradient across the lens stays almost zero due to too large R. Or micro-/nano-fabrication techniques again could be considered to fabricate a sub-μm pyramid object that represents a particular constant phase gradient. For example, anisotropic web etching of crystalline silicon wafers gives micro-pyramid dips that could be used as a nano-imprinting mask. A laser-assisted multi-photon polymerization process could also provide small polymer pyramids that can be potentially used for PGTF characterization.

Most microscope samples are sitting on microscope slide glasses or immersed in liquid medium in thin petri dishes, of which effects were neglected here in the nonparaxial DPC formulation. The light refraction at the air-glass (or air-liquid) boundary before the sample may reduce illumination NA in the wide-field DPC system, perturbing the partial coherent sigma. Also, the glass (or liquid) medium may add spherical aberrations which then may modify DPC intensity. In high NA DPC imaging, this effect may also have to be considered.

Chapter 6

Conclusion

6.1 Conclusion and Outlook

To overcome the biggest challenges in optical microscopy such as super-resolution, imaging speed, penetration depth, novel high NA microscopy methods were studied.

Oblique plane microscopy (OPM), in Chapter 3, achieves high-speed deep imaging over any oblique plane of interest in a thick sample. Microscopy samples are not always prepared such that the principal plane of the sample is aligned in parallel to the microscope coverglass and/or slide glass. Also some samples such as living neuronal dendrites in brains are arranged perpendicular to sample surfaces. OPM can be a simple, cost-effective method suitable for such applications as well as diagnostic purposes such as skin cancer detections. As OPM takes an image at an inclined angle with a secondary microscope, there occurs anisotropic pupil loss that lowers optical resolution. This dissertation analytically studied such an anisotropic resolving power and its physical interpretation to improve the general understanding on wide-field OPM.

Current single molecule super-resolution microscopy (STORM), typically combined with a total internal reflection (TIR) or near-TIR illumination schematic for higher signal-to-background ratio (SBR) required in STORM, limits its imaging depth near the surface of samples. It is mainly because its shallower illumination depth and an index-mismatch present for TIR illumination. Here in Chapter 4, using oblique lightsheet illumination (alternative way to get a high SBR), super-resolution oblique plane microscopy, *oblique*STORM, was proposed for super-resolution deep imaging. The achievable imaging resolution and penetration depth were analytically investigated. It is expected that sub-50-nm resolution over a depth of around 80 μm would be feasible. The resolution could be further improved by several times if *oblique*STORM is implemented with much brighter dyes [159] or in cryogenic environment [160, 161]. As for potential applications, like STED, the other super-resolution technique applied to image actin dynamics in synapses of living brains [162], *oblique*STORM can be utilized for similar tissue level studies without sample agitation. Or it could be applied to intracellular studies, for example, single-molecule tracking of transcription factors in the nucleus of mammalian cells [163].

Label-free imaging would be an ultimate goal in (live) biological imaging, if the target specificity is solved. To attain this goal, optical differential phase contrast (DPC) microscopy can be a good potential approach. The current DPC imaging theory, more specifically the transmission cross-coefficient (TCC), explains how the phase information of samples is converted to the DPC intensity that is measured, with a good accuracy only at a lower NA regime. Thus the reconstruction of quantitative phase information of samples using the paraxial TCC is inaccurate at high NA DPC imaging. In Chapter 5, a scalar nonparaxial TCC for high NA DPC imaging was developed. It considered the nonparaxial nature of light propagation, the apodization of the aplanatic objective lens, and light source properties. The nonparaxial TCC derived was compared with the paraxial TCC, and the practical forms of the TCC simplified for two special types of objects, weak objects and slowly varying phase objects, were discussed for high NA phase imaging. It is expected that the nonparaxial TCC developed here can be a general model that covers all NA regimes for accurate phase retrieval in high resolution quantitative phase imaging of biological samples or any other phase object of interest. Moreover, the scalar nonparaxial image formation theory formulated here can be directly applied to any type of partially coherent imaging systems in general, such as conventional high NA brightfield imaging.

The theoretical studies carried out here can assist to establish the high NA microscopy methods discussed into the real world to overcome imaging challenges. On the other hand, the new sign conventions for vectorial ray tracing were proposed in this dissertation, which produce physically consistent tracing results of light polarization (which did not with the sign conventions used in previous studies). The sign convention for the coordinate in evaluating the vectorial diffraction integral could be also unified as done throughout this dissertation. Such systematic conventions can help to avoid any physically wrong interpretation during a vectorial analysis on any high-aperture optical systems.

6.2 Future work

The future work and possible research directions arising from the studies presented in this dissertation are as follows:

For *oblique*STORM, the point spread function (PSF) predicted in the oblique imaging mode may need to be experimentally proven over oblique angles. This can confirm the preliminary conclusion made on the best system layout in the oblique imaging mode based on the theoretical grounds. As the mechanical drifts matter in STORM, a good compensation strategy would need to come up with especially when STORM data is acquired over a prolonged time span. After this, real demonstration of super-resolution deep imaging of biological samples can be performed, which then complete the feasibility study of *oblique*STORM. For scientific interests or more practical purposes, further study could be conducted on the compatibility of *oblique*STORM with the existing 3D localization methods [140, 141, 164, 165] to achieve 3D *oblique*STORM.

For high NA optical DPC imaging, an experimental proof of the nonparaxial TCC model derived is essential. To do so, a proper artificial phase object would need to be fabricated as addressed in Section 5.6. An effect of microscope slide glasses or a liquid buffer in petri dishes, where samples are typically prepared, on high NA DPC intensity would need to be verified and incorporated in the theory if it turned out to be necessary. Once the nonparaxial TCC model is rigorously proven to be correct, then it could be easily extended and used for three-dimensional quantitative phase imaging valid at any NA regime. Also, in practical point of view, the development of a software algorithm that determines 2D or 3D local phase gradients from high NA experimental DPC images based on the phase gradient transfer function would be very useful. A study of the light-sample interaction to account for the vectorial nature in high-aperture DPC imaging would be a prerequisite to develop an accurate vectorial DPC imaging theory.

Bibliography

1. Wojcik, M., Hauser, M., Li, W., Moon, S. & Xu, K. Graphene-enabled electron microscopy and correlated super-resolution microscopy of wet cells. *Nature Communications* **6,** 7384 (2015).
2. Pendry, J. B. Negative Refraction Makes a Perfect Lens. *Physical Review Letters* **85,** 3966–3969 (2000).
3. Fang, N., Lee, H., Sun, C. & Zhang, X. Sub-diffraction-limited optical imaging with a silver superlens. *Science* **308,** 534–537 (2005).
4. Liu, Z., Lee, H., Xiong, Y., Sun, C. & Zhang, X. Far-field optical hyperlens magnifying sub-diffraction-limited objects. *Science* **315,** 1686 (2007).
5. Rho, J. *et al.* Spherical hyperlens for two-dimensional sub-diffractional imaging at visible frequencies. *Nature Communications* **1,** 143 (2010).
6. Lu, D. & Liu, Z. Hyperlenses and metalenses for far-field super-resolution imaging. *Nature Communications* **3** (2012).
7. Huang, F. M. & Zheludev, N. I. Super-Resolution without Evanescent Waves. *Nano Letters* **9,** 1249–1254 (2009).
8. Rogers, E. T. F. *et al.* A super-oscillatory lens optical microscope for subwavelength imaging. *Nature Materials* **11,** 432–435 (2012).
9. Gustafsson, M. G. Surpassing the lateral resolution limit by a factor of two using structured illumination microscopy. *Journal of Microscopy* **198,** 82–87 (2000).
10. Chen, B.-C. *et al.* Lattice light-sheet microscopy: imaging molecules to embryos at high spatiotemporal resolution. *Science* **346,** 1257998 (2014).
11. Gustafsson, M. G. L. Nonlinear structured-illumination microscopy: wide-field fluorescence imaging with theoretically unlimited resolution. *Proceedings of the National Academy of Sciences of the United States of America* **102,** 13081–13086 (2005).
12. Wei, F. & Liu, Z. Plasmonic Structured Illumination Microscopy. *Nano Letters* **10,** 2531–2536 (2010).
13. Wei, F. *et al.* Wide field super-resolution surface imaging through plasmonic structured illumination microscopy. *Nano Letters* **14,** 4634–4639 (2014).

14. Narimanov, E. Hyper-Structured Illumination. *ACS Photonics,* 5 (2016).

15. Hell, S. W. & Wichmann, J. Breaking the diffraction resolution limit by stimulated emission: stimulated-emission-depletion fluorescence microscopy. *Optics Letters* **19,** 780 (1994).

16. Chmyrov, A. *et al.* Nanoscopy with more than 100,000 'doughnuts'. *Nature Methods* **10,** 737–740 (2013).

17. Betzig, E. *et al.* Imaging intracellular fluorescent proteins at nanometer resolution. *Science* **313,** 1642–1645 (2006).

18. Hess, S. T., Girirajan, T. P. K. & Mason, M. D. Ultra-high resolution imaging by fluorescence photoactivation localization microscopy. *Biophysical Journal* **91,** 4258–4272 (2006).

19. Rust, M. J., Bates, M. & Zhuang, X. Sub-diffraction-limit imaging by stochastic optical reconstruction microscopy (STORM). *Nature Methods* **3,** 793–795 (2006).

20. Vaughan, J. C., Jia, S. & Zhuang, X. Ultrabright photoactivatable fluorophores created by reductive caging. *Nature Methods* **9,** 1181–1184 (2012).

21. Weisenburger, S. *et al.* Cryogenic colocalization microscopy for nanometer-distance measurements. *ChemPhysChem* **15,** 763–770 (2014).

22. Kaufmann, R. *et al.* Super-resolution microscopy using standard fluorescent proteins in intact cells under cryo-conditions. *Nano Letters* **14,** 4171–4175 (2014).

23. Science, E. Adaptive optics in microscopy. *Phil. Trans. R. Soc. A* **365,** 2829–2843 (2007).

24. Ahrens, M. B., Orger, M. B., Robson, D. N., Li, J. M. & Keller, P. J. Whole-brain functional imaging at cellular resolution using light-sheet microscopy. *Nature Methods* **10,** 413–420 (2013).

25. Wang, K. *et al.* Rapid adaptive optical recovery of optimal resolution over large volumes. *Nature Methods* **11,** 625–628 (2014).

26. Ntziachristos, V. Going deeper than microscopy: the optical imaging frontier in biology. *Nature Methods* **7,** 603–614 (2010).

27. Kobat, D., Horton, N. G. & Xu, C. In vivo two-photon microscopy to 1.6-mm depth in mouse cortex. *Journal of Biomedical Optics* **16,** 106014 (2011).

28. Horton, N. G. *et al.* In vivo three-photon microscopy of subcortical structures within an intact mouse brain. *Nature Photonics* **7,** 205–209 (2013).

29. Katz, O., Bromberg, Y., Small, E. & Silberberg, Y. Focusing and Compression of Ultrashort Pulses through Scattering Media. *Nature Photonics* **5,** 372–377 (2010).

30. Chaigne, T. *et al.* Controlling light in scattering media non-invasively using the photoacoustic transmission matrix. *Nature Photonics* **8,** 58–64 (2013).

31. Wang, Y. M., Judkewitz, B., DiMarzio, C. A. & Yang, C. Deep-tissue focal fluorescence imaging with digitally time-reversed ultrasound-encoded light. *Nature Communications* **3,** 928 (2012).
32. Judkewitz, B., Wang, Y. M., Horstmeyer, R., Mathy, A. & Yang, C. Speckle-scale focusing in the diffusive regime with time reversal of variance-encoded light (TROVE). *Nature Photonics* **7,** 300–305 (2013).
33. Nixon, M. *et al.* Real-time wavefront shaping through scattering media by all-optical feedback. *Nature Photonics* **7,** 919–924 (2013).
34. Ma, C., Xu, X., Liu, Y. & Wang, L. V. Time-reversed adapted-perturbation (TRAP) optical focusing onto dynamic objects inside scattering media. *Nature Photonics* **8,** 931–936 (2014).
35. Lai, P., Wang, L., Tay, J. W. & Wang, L. V. Photoacoustically guided wavefront shaping for enhanced optical focusing in scattering media. *Nature Photonics* **9,** 126–132 (2015).
36. Katz, O., Heidmann, P., Fink, M. & Gigan, S. Non-invasive single-shot imaging through scattering layers and around corners via speckle correlations. *Nature Photonics* **8,** 784–790 (2014).
37. Bertolotti, J. *et al.* Non-invasive imaging through opaque scattering layers. *Nature* **491,** 232–234 (2012).
38. Hu, S., Maslov, K. & Wang, L. V. Second-generation optical-resolution photoacoustic microscopy with improved sensitivity and speed. *Optics Letters* **36,** 1134 (2011).
39. Razansky, D. *et al.* Multispectral opto-acoustic tomography of deep-seated fluorescent proteins in vivo. *Nature Photonics* **3,** 412–417 (2009).
40. Wang, L. V. & Hu, S. Photoacoustic Tomography: In Vivo Imaging from Organelles to Organs. *Science* **335,** 1458–1462 (2012).
41. Zhang, H. F., Maslov, K., Stoica, G. & Wang, L. V. Functional photoacoustic microscopy for high-resolution and noninvasive in vivo imaging. *Nature Biotechnology* **24,** 848–851 (2006).
42. Beard, P. *et al.* Biomedical photoacoustic imaging. *Interface Focus* **1,** 602–631 (2011).
43. Troy, T., Jekic-McMullen, D., Sambucetti, L. & Rice, B. Quantitative comparison of the sensitivity of detection of fluorescent and bioluminescent reporters in animal models. *Molecular Imaging* **3,** 9–23 (2004).
44. Deliolanis, N. C. *et al.* Performance of the red-shifted fluorescent proteins in deep-tissue molecular imaging applications. *Journal of Biomedical Optics* **13,** 044008 (2008).
45. Wei Zhang, Z. Maturation of Layer V Pyramidal Neurons in the Rat Prefrontal Cortex: Intrinsic Properties and Synaptic Function. *Journal of Neurophysiology* **91,** 1171–1182 (2004).

46. Buzsáki, G., Logothetis, N. & Singer, W. Scaling brain size, keeping timing: Evolutionary preservation of brain rhythms. *Neuron* **80,** 751–764 (2013).
47. Wloga, D. & Frankel, J. From Molecules to Morphology: Cellular Organization of Tetrahymena thermophila. *Methods in Cell Biology* **109,** 83–140 (2012).
48. Bouchard, M. B. *et al.* Swept confocally-aligned planar excitation (SCAPE) microscopy for high-speed volumetric imaging of behaving organisms. *Nature Photonics* **9,** 113–119 (2015).
49. Fahrbach, F. O., Voigt, F. F., Schmid, B., Helmchen, F. & Huisken, J. Rapid 3D light-sheet microscopy with a tunable lens. *Optics Express* **21,** 21010 (2013).
50. Smith, D. R., Winters, D. G. & Bartels, R. A. Submillisecond second harmonic holographic imaging of biological specimens in three dimensions. *Proc. Natl. Acad. Sci. USA* **110,** 18391–18396 (2013).
51. Levo, M., Ng, R., Adams, A., Footer, M. & Horowitz, M. Light Field Microscopy. *ACM Transactions on Graphics* **25** (2006).
52. Prevedel, R. *et al.* Simultaneous whole-animal 3D imaging of neuronal activity using light-field microscopy. *Nature Methods* **11,** 727–730 (2014).
53. Wakin, M. B. *et al. An architecture for compressive imaging.* in *Proceedings of International Conference on Image Processing, ICIP* (IEEE, 2006), 1273–1276.
54. Candès, E. J., Romberg, J. K. & Tao, T. Stable signal recovery from incomplete and inaccurate measurements. *Communications on Pure and Applied Mathematics* **59,** 1207–1223 (2006).
55. Donoho, D. Compressed sensing. *IEEE Transactions on Information Theory* **52,** 1289–1306 (2006).
56. Guo, Q. *et al.* Fast time-lens-based line-scan single-pixel camera with multi-wavelength source. *Biomedical Optics Express* **6,** 3610–3617 (2015).
57. Bosworth, B. T. *et al.* High-speed flow microscopy using compressed sensing with ultrafast laser pulses. *Optics Express* **23,** 10521 (2015).
58. Diebold, E. D., Buckley, B. W., Gossett, D. R. & Jalali, B. Digitally-synthesized beat frequency multiplexing for sub-millisecond fluorescence microscopy. *Nature Photonics* **7,** 806–810 (2013).
59. Stelzer, E. H. K. Light-sheet fluorescence microscopy for quantitative biology. *Nature Methods* **12,** 23–26 (2014).
60. Magidson, V. & Khodjakov, A. Circumventing photodamage in live-cell microscopy. *Methods in Cell Biology* **114,** 545–560 (2013).
61. Brida, G., Genovese, M. & Ruo Berchera, I. Experimental realization of sub-shot-noise quantum imaging. *Nature Photonics* **4,** 227–230 (2010).

62. Taylor, M. A. *et al.* Biological measurement beyond the quantum limit. *Nature Photonics* **7,** 229–233 (2013).
63. Zernike, F. How I discovered phase contrast. *Science* **121,** 345–349 (1955).
64. McCormick, B. H. Brain tissue scanner enables brain microstructure surveys. *Neurocomputing* **44-46,** 1113–1118 (2002).
65. Kim, M. K. Principles and techniques of digital holographic microscopy. *Journal of Photonics for Energy* **1,** 018005 (2010).
66. Murphy, D. B. & Davidson, M. W. *Differential Interference Contrast Microscopy and Modulation Contrast Microscopy.* 2nd ed., 173–198 (John Wiley & Sons, Inc., Hoboken, NJ, USA, 2012).
67. Huang, D. *et al.* Optical coherence tomography. *Science* **254,** 1178–1181 (1991).
68. Mertz, J. Nonlinear microscopy: New techniques and applications. *Current Opinion in Neurobiology* **14,** 610–616 (2004).
69. Min, W., Freudiger, C. W., Lu, S. & Xie, X. S. Coherent nonlinear optical imaging: beyond fluorescence microscopy. *Annual review of physical chemistry* **62,** 507–530 (2011).
70. Tong, L. & Cheng, J.-X. Label-free imaging through nonlinear optical signals. *Materials Today* **14,** 264–273 (2011).
71. Ye, T., Fu, D. & Warren, W. S. Nonlinear absorption microscopy. *Photochemistry and photobiology* **85,** 631–645 (2009).
72. Ou, X., Horstmeyer, R., Yang, C. & Zheng, G. Quantitative phase imaging via Fourier ptychographic microscopy. *Optics Letters* **38,** 4845–4848 (2013).
73. Tian, L. & Waller, L. Quantitative differential phase contrast imaging in an LED array microscope. *Optics Express* **23,** 11394–11403 (2015).
74. Gobel, W. & Helmchen, F. New angles on neuronal dendrites in vivo. *Journal of Neurophysiology* **98,** 3770–3779 (2007).
75. Dunsby, C. Optically sectioned imaging by oblique plane microscopy. *Optics Express* **16,** 20306–20316 (2008).
76. Anselmi, F., Ventalon, C., Begue, A., Ogden, D. & Emiliani, V. Three-dimensional imaging and photostimulation by remote-focusing and holographic light patterning. *Proc. Natl. Acad. Sci. USA* **108,** 19504–19509 (2011).
77. Smith, C. W., Botcherby, E. J. & Wilson, T. Resolution of oblique-plane images in sectioning microscopy. *Optics Express* **19,** 2662–2669 (2011).
78. Smith, C. W., Botcherby, E. J., Booth, M. J., Juskaitis, R. & Wilson, T. Agitation-free multiphoton microscopy of oblique planes. *Optics Letters* **36,** 663–665 (2011).
79. Goodman, J. W. *Introduction to Fourier Optics.* 3rd ed. (W. H. Freeman, 2004).

80. Mansuripur, M. Distribution of light at and near the focus of high-numerical-aperture objectives. *J. Opt. Soc. Am. A* **3,** 2086 (1986).
81. Sheppard, C. J. R. & Matthews, H. J. Imaging in high-aperture optical systems. *J. Opt. Soc. Am. A* **4,** 1354–1360 (1987).
82. Foreman, M. R. & Török, P. Computational methods in vectorial imaging. *Journal of Modern Optics* **58,** 339–364 (2011).
83. Munro, P. R. T. & Török, P. Vectorial, high-numerical-aperture study of phase-contrast microscopes. *J. Opt. Soc. Am. A* **21,** 1714–1723 (2004).
84. Munro, P. R. T. & Török, P. Calculation of the image of an arbitrary vectorial electromagnetic field. *Optics express* **15,** 9293–9307 (2007).
85. Török, P., Munro, P. R. T. & Kriezis, E. E. High numerical aperture vectorial imaging in coherent optical microscopes. *Optics express* **16,** 507–523 (2008).
86. Jackson, J. D. *Classical electrodynamics.* 3rd ed. (Wiley, New York, 1999).
87. Stratton, J. A. & Chu, L. J. Diffraction Theory of Electromagnetic Waves. *Physical Review* **56,** 99–107 (1939).
88. Stratton, J. A. *Electromagnetic theory.* (McGraw-Hill, 1941).
89. Sheppard, C., Choudhury, A. & Gannaway, J. Electromagnetic field near the focus of wide-angular lens and mirror system. *IEE journal on microwaves* **1,** 129–132 (1977).
90. Gu, M. *Advanced optical imaging theory.* (Springer, New York, 2000).
91. Wolf, E. & Li, Y. Conditions for the Validity of the Debye Integral-Representation of Focused Fields. *Optics Communications* **39,** 205–210 (1981).
92. Li, Y. J. Focal shifts in diffracted converging electromagnetic waves. I. Kirchhoff theory. *J. Opt. Soc. Am. A* **22,** 68–76 (2005).
93. Li, Y. J. Focal shifts in diffracted converging electromagnetic waves. II. Rayleigh theory. *J. Opt. Soc. Am. A* **22,** 77–83 (2005).
94. Shibuya, M. *et al.* Incoming inclination factor for scalar imaging theory. *Optical Engineering* **49,** 023202 (2010).
95. Goodman, J. W. *Statistical optics.* (Wiley, 2000).
96. Frieden, B. R. Optical Transfer of the Three-Dimensional Object. *J. Opt. Soc. Am.* **57,** 56 (1967).
97. Zernike, F. The concept of degree of coherence and its application to optical problems. *Physica* **5,** 785–795 (1938).
98. McCutchen, C. W. Generalized Source and the van Cittert-Zernike Theorem: A Study of the Spatial Coherence Required for Interferometry. *J. Opt. Soc. Am.* **56,** 727 (1966).
99. Hopkins, H. H. On the Diffraction Theory of Optical Images. *Proc. R. Soc. Lond. A* **217,** 408–432 (1953).

100. Born, M. & Wolf, E. *Principles of Optics.* 7th ed. (Cambridge University Press, 1999).
101. Thompson, B. J. Image Formation with Partially Coherent Light. *Progress in Optics* **7,** 169–230 (1969).
102. Stephanakis, A. C. & Rubin, D. I. *Advances In 1:1 Optical Lithography* in *International Society for Optics and Photonics* (1987), 74–85.
103. Sheppard, C. J. R., Kawata, Y., Kawata, S. & Gu, M. Three-dimensional transfer functions for high-aperture systems. *J. Opt. Soc. Am. A* **11,** 593 (1994).
104. Novotny, L. & Hecht, B. *Principles of Nano-Optics.* 2nd ed. (Cambridge, 2012).
105. Stamnes, J. J. *Waves in focal regions: propagation, diffraction, and focusing of light, sound, and water waves.* (Adam Hilger, Bristol, UK, 1986).
106. McCutchen, C. W. Generalized Aperture and the Three-Dimensional Diffraction Image. *J. Opt. Soc. Am.* **54,** 240 (1964).
107. Richards, B. & Wolf, E. Electromagnetic Diffraction in Optical Systems. II. Structure of the Image Field in an Aplanatic System. *Proc. R. Soc. Lond. A* **253,** 358–379 (1959).
108. Sheppard, C. J. R., Choudhury, A. & Gannaway, J. Electromagnetic field near focus of wide-angular lens and mirror systems. *Iee Journal on Microwaves Optics and Acoustics* **1,** 129–132 (1977).
109. Nijboer, B. The diffraction theory of optical aberrations. *Physica* **13,** 605–620 (1947).
110. Visser, T. D. & Wiersma, S. H. Spherical aberration and the electromagnetic field in high-aperture systems. *J. Opt. Soc. Am. A* **8,** 1404–1410 (1991).
111. Kant, R. An analytical solution of vector diffraction for focusing optical systems. *Journal of Modern Optics* **40,** 337–347 (1993).
112. Kant, R. An analytical solution of vector diffraction for focusing optical systems with Seidel aberrations. *Journal of Modern Optics* **40,** 2293–2310 (1993).
113. Török, P., Varga, P., Laczik, Z. & Booker, G. R. Electromagnetic diffraction of light focused through a planar interface between materials of mismatched refractive indices: an integral representation. *J. Opt. Soc. Am. A* **12,** 325 (1995).
114. Yun, G., Crabtree, K. & Chipman, R. A. Three-dimensional polarization ray-tracing calculus I: definition and diattenuation. *Applied optics* **50,** 2855–2865 (2011).
115. Yun, G., McClain, S. C. & Chipman, R. A. Three-dimensional polarization ray-tracing calculus II: retardance. *Applied optics* **50,** 2866–2874 (2011).
116. Sheppard, C. J. R. & Larkin, K. G. Vectorial pupil functions and vectorial transfer functions. *Optik* **107,** 79–87 (1997).
117. Arnison, M. R. & Sheppard, C. J. R. A 3D vectorial optical transfer function suitable for arbitrary pupil functions. *Optics Communications* **211,** 53–63 (2002).

118. Török, P., Higdon, P. D. & Wilson, T. Theory for confocal and conventional microscopes imaging small dielectric scatterers. *Journal of Modern Optics* **45,** 1681–1698 (1998).

119. Török, P., Higdon, P. & Wilson, T. On the general properties of polarised light conventional and confocal microscopes. *Optics Communications* **148,** 300–315 (1998).

120. Hecht, E. *Optics.* 5th ed. (Pearson, 2016).

121. Peatross, J. & Ware, M. *Physics of Light and Optics.* 2015 editi (available at optics.byu.edu).

122. Gerrard, A. & Burch, J. M. *Introduction to Matrix Methods in Optics.* (Dover Publications, 1975).

123. Kumar, S. *et al.* High-speed 2D and 3D fluorescence microscopy of cardiac myocytes. *Optics Express* **19,** 13839 (2011).

124. Cutrale, F. & Gratton, E. Inclined selective plane illumination microscopy adaptor for conventional microscopes. *Microscopy research and technique* **75,** 1461–1466 (2012).

125. Botcherby, E. J., Juskaitis, R., Booth, M. J. & Wilson, T. Aberration-free optical refocusing in high numerical aperture microscopy. *Optics Letters* **32,** 2007–2009 (2007).

126. Botcherby, E. J., Juskaitis, R., Booth, M. J. & Wilson, T. An optical technique for remote focusing in microscopy. *Optics Communications* **281,** 880–887 (2008).

127. Kim, J., Li, T., Wang, Y. & Zhang, X. Vectorial point spread function and optical transfer function in oblique plane imaging. *Optics Express* **22,** 11140–11151 (2014).

128. Huisken, J., Swoger, J., Del Bene, F., Wittbrodt, J. & Stelzer, E. H. K. Optical sectioning deep inside live embryos by selective plane illumination microscopy. *Science* **305,** 1007–1009 (2004).

129. Li, T. *et al.* Axial Plane Optical Microscopy. *Scientific Reports* **4,** 1–6 (2014).

130. Chaudhuri, O., Parekh, S. H., Lam, W. A. & Fletcher, D. A. Combined atomic force microscopy and side-view optical imaging for mechanical studies of cells. *Nature Methods* **6,** 383–387 (2009).

131. Andermann, M. L. *et al.* Chronic cellular imaging of entire cortical columns in awake mice using microprisms. *Neuron* **80,** 900–913 (2013).

132. Flors, C. & Earnshaw, W. C. Super-resolution fluorescence microscopy as a tool to study the nanoscale organization of chromosomes. *Curr. Opin. Chem. Biol.* **15,** 838–844 (2011).

133. Flors, C. DNA and chromatin imaging with super-resolution fluorescence microscopy based on single-molecule localization. *Biopolymers* **95,** 290–297 (2011).

134. Xu, K., Babcock, H. P. & Zhuang, X. Dual-objective STORM reveals three-dimensional filament organization in the actin cytoskeleton. *Nature methods* **9,** 185–188 (2012).

135. Izeddin, I. *et al.* PSF shaping using adaptive optics for three-dimensional single-molecule super-resolution imaging and tracking. *Optics Express* **20,** 4957 (2012).

136. Van de Linde, S. *et al.* Direct stochastic optical reconstruction microscopy with standard fluorescent probes. *Nature Protocols* **6,** 991–1009 (2011).

137. Brockett, R. W. *Robotic manipulators and the product of exponentials formula.* 120–129 (1984).

138. Polyanskiy, M. N. *"Refractive index database," http://refractiveindex.info (accessed Dec. 5, 2015).*

139. Thompson, R. E., Larson, D. R. & Webb, W. W. Precise nanometer localization analysis for individual fluorescent probes. *Biophysical journal* **82,** 2775–2783 (2002).

140. Deschout, H. *et al.* Precisely and accurately localizing single emitters in fluorescence microscopy. *Nature Methods* **11,** 253–266 (2014).

141. Huang, B., Wang, W., Bates, M. & Zhuang, X. Three-dimensional super-resolution imaging by stochastic optical reconstruction microscopy. *Science* **319,** 810–813 (2008).

142. Dempsey, G. T., Vaughan, J. C., Chen, K. H., Bates, M. & Zhuang, X. Evaluation of fluorophores for optimal performance in localization-based super-resolution imaging. *Nature Methods* **8,** 1027–1036 (2011).

143. Dempsey, G. T., Vaughan, J. C., Chen, K. H., Bates, M. & Zhuang, X. Evaluation of fluorophores for optimal performance in localization-based super-resolution imaging. *Nature Methods* **8,** 1027–1036 (2011).

144. Olivier, N., Keller, D., Gönczy, P. & Manley, S. Resolution doubling in 3D-STORM imaging through improved buffers. *PloS one* **8,** e69004 (2013).

145. Olivier, N., Keller, D., Rajan, V. S., Gönczy, P. & Manley, S. Simple buffers for 3D STORM microscopy. *Biomedical Optics Express* **4,** 885–899 (2013).

146. Dekkers, N. H. & Lang, H. Differential Phase Contrast in a STEM. *Optik* **41,** 452–456 (1974).

147. Hamilton, D. K. & Sheppard, C. J. R. Differential phase contrast in scanning optical microscopy. *Journal of Microscopy* **133,** 27–39 (1984).

148. Hamilton, D. K., Sheppard, C. J. R. & Wilson, T. Improved imaging of phase gradients in scanning optical microscopy. *Journal of Microscopy* **135,** 275–286 (1984).

149. Schmahl, G. & Rudolph, D. in *X-ray Microscopy* 231–238 (Springer Berlin Heidelberg, 1987).

150. Shibata, N. *et al.* Differential phase-contrast microscopy at atomic resolution. *Nature Physics* **8,** 611–615 (2012).

151. Kachar, B. Asymmetric illumination contrast: a method of image formation for video light microscopy. *Science* **227,** 766–768 (1985).

152. Noda, T., Kawata, S. & Minami, S. Three-dimensional phase-contrast imaging by a computed-tomography microscope. *Applied Optics* **31,** 670 (1992).

153. Mehta, S. B. & Sheppard, C. J. R. Quantitative phase-gradient imaging at high resolution with asymmetric illumination-based differential phase contrast. *Optics Letters* **34,** 1924 (2009).

154. Tian, L., Wang, J. & Waller, L. 3D differential phase-contrast microscopy with computational illumination using an LED array. *Optics Letters* **39,** 1326–1329 (2014).

155. Lee, D., Ryu, S., Kim, U., Jung, D. & Joo, C. Color-coded LED microscopy for multi-contrast and quantitative phase-gradient imaging. *Biomedical Optics Express* **6,** 4912 (2015).

156. Sheppard, C. & Choudhury, A. Image Formation in the Scanning Microscope. *Optica Acta: International Journal of Optics* **24,** 1051–1073 (1977).

157. Harker, M. & O'leary, P. *Least squares surface reconstruction from gradients: Direct algebraic methods with spectral, Tikhonov, and constrained regularization* in *Proceedings of the IEEE Computer Society Conference on Computer Vision and Pattern Recognition* (IEEE, 2011), 2529–2536.

158. Ni, X. *et al.* An ultrathin invisibility skin cloak for visible light. *Science* **349,** 1310–1314 (2015).

159. Vaughan, J. C., Jia, S. & Zhuang, X. Ultrabright photoactivatable fluorophores created by reductive caging. *Nature methods* **9,** 1181–1184 (2012).

160. Weisenburger, S. *et al.* Cryogenic Colocalization Microscopy for Nanometer-Distance Measurements. *ChemPhysChem* **15,** 763–770 (2014).

161. Kaufmann, R. *et al.* Super-Resolution Microscopy Using Standard Fluorescent Proteins in Intact Cells under Cryo-Conditions. *Nano Letters* **14,** 4171–4175 (2014).

162. Urban, N. T., Willig, K. I., Hell, S. W. & Nägerl, U. V. STED nanoscopy of actin dynamics in synapses deep inside living brain slices. *Biophysical Journal* **101,** 1277–1284 (2011).

163. Izeddin, I. *et al.* Single-molecule tracking in live cells reveals distinct target-search strategies of transcription factors in the nucleus. *eLife* **3** (2014).

164. Badieirostami, M., Lew, M. D., Thompson, M. A. & Moerner, W. E. Three-dimensional localization precision of the double-helix point spread function versus astigmatism and biplane. *Applied physics letters* **97,** 161103 (2010).

165. Jia, S., Vaughan, J. C. & Zhuang, X. Isotropic 3D Super-resolution Imaging with a Self-bending Point Spread Function. *Nature photonics* **8,** 302–306 (2014).